Symmetry and Topological Phases in Condensed Matter and Beyond

Simon Kin-Wei Lieu

Thesis submitted for the degree of

Doctor of Philosophy of Imperial College London

Condensed Matter Theory Group

Department of Physics

Blackett Laboratory

Imperial College London

June 20, 2019

Declaration of Originality

I declare that the work presented in this thesis is my own work unless otherwise referenced.

Copyright Declaration

Abstract

Topological phase transitions represent a new paradigm beyond conventional Landau-Ginzburg symmetry breaking. Even in the absence of symmetry breaking, the symmetries of a Hamiltonian play an important role in stabilizing topological signatures. In this thesis, we will study the interplay between symmetry and topology in many-body systems, with three distinct physical setups in mind.

First, we investigate a two-dimensional system of ultracold bosons which is condensed in the p-band of a triangular lattice. Certain smooth interaction profiles result in non-Abelian symmetry generators of the order parameter manifold, leading to anomalous physical consequences. These include a lack of Berezinskii-Kosterlitz-Thouless transition due to unstable vortex configurations, additional Goldstone modes, and a marginally divergent normal fluid density which implies lack of superfluidity in the thermodynamic limit. Our results suggest possible connections to solid state experiments on ^{4}He films.

We then show that disorder which keeps a Hamiltonian in the same Altland-Zirnbauer symmetry class is capable of inducing a topological transition. This is achieved by considering the normalizability of Majorana edge modes in a topological superconductor, and corroborated with entanglement metrics. While degeneracies of the many-body spectrum are robust with respect to weak perturbations, strong disorder can both promote and destroy a topological index.

Lastly, we study topological edge modes and degeneracies in atomic, molecular, and optical systems which evolve non-unitarily in time or space due to non-equilibrium effects, including: condensate instabilities after a quench, decoherence channels from an external environment, and dissipation into a medium. Mathematically, the non-unitary evolution is generated by effective Hamiltonians which break Hermiticity. These systems can possess uniquely non-Hermitian symmetries which are absent from equilibrium counterparts. We present a symmetry-based classification, and investigate several systems which can be solved exactly.

Publications

This thesis contains work drawn from the following publications:

- **Simon Lieu**. "Non-Hermitian Majorana modes protect degenerate steady states," arXiv:1904.07481 (2019).

- **Simon Lieu**, Andrew F. Ho, Derek K. K. Lee, and Piers Coleman. "Intertwined superfludity and density wave order in a p-orbital Bose condensate," *Phys. Rev. B*, 99 014504 (2019).

- **Simon Lieu**, Derek K. K. Lee, and Johannes Knolle. "Disorder protected and induced local zero-modes in longer-range Kitaev chains," *Phys. Rev. B*, 98 134507 (2018).

- **Simon Lieu**. "Topological symmetry classes for non-Hermitian models and connections to the bosonic Bogoliubov-de Gennes equation," *Phys. Rev. B*, 98 115135, (2018).

- **Simon Lieu**. "Topological phases in the non-Hermitian Su-Schrieffer-Heeger model," *Phys. Rev. B*, 97 045106, (2018).

Acknowledgments

First and foremost, I thank my advisor, Derek, for his academic insight, guidance, patience, and humor. It has been a pleasure to work with him and I am am grateful for the countless hours spent teaching me how to do research. Doing physics everyday is a demanding task; I thank him for making the last few years exciting and enjoyable from beginning to end.

I would like to thank a number of academic collaborators and mentors who have also greatly influenced my research style and ideas over the last few years. Most notably: Johannes Knolle, Ryan Barnett, Andrew Ho, and Piers Coleman. Variety is the spice of life, and I am very thankful to have learned a broad range of condensed matter theory from these experts.

I would also like to thank a number of external academics who supported my early career in research by inviting me to give talks and visit their institutions. Specifically: Emil Bergholtz, Shu Chen, Jasper van Wezel, Hossein Sadeghpour, and Liang Fu. I have greatly benefited from these discussions and it was inspiring to meet other physicists who are passionate about similar ideas. I thank Nigel Cooper for hosting me in Cambridge during the last part of my PhD, where the final portion of this thesis was completed.

There is more to life than physics, and I am grateful for the friendships (old and new) which have made the last few years so memorable. From the office: Simon (2), Freddie, Joachim, Illya, Ollie, Marise, Seyed, Nuttawut, Alex, Lara, Stefano, Iacopo, Gleb, Tom, Joe, Fan, Emanuele; thanks to Imperial Medics Rowing for the fun times both on and off the water; thanks to my flatmates Boshko and Elisa for keeping me grounded in reality; for providing reasons to escape London (spontaneous or not), I thank: Karla, Beñat, Caleb, Nate, Suyoung, Andy, Johnny, Josie-Dee, Todd.

I would especially like to thank Tracey Olsen for making it possible for me to live near Gloucester Road for the majority of my doctoral studies. No doubt the creative interior design, paint fumes, and supernatural discussions are to blame for my outlandish theories.

Finally, I would like to thank my parents for their love, endless support, and encouragement throughout this and every season of my life. This thesis is dedicated to them.

Contents

List of Figures

List of Tables

Chapter 1

History, models, and methods

1.1 Historical background

At the heart of condensed matter theory lies the study of phase transitions. In simplest terms, a phase transition occurs when a large number of particles exhibit qualitatively different *collective* behavior as a function of a single parameter of the system. The most common example is the liquid-to-solid transition: As one varies the temperature of water from above to below 0 °C, the behavior of the molecules changes dramatically. Above the transition temperature, the liquid phase is characterized by randomly distributed and uncorrelated particle positions and velocities, resulting in a fluid which conforms to the shape of its container. Below the transition, particles orient themselves in a rigid lattice structure known as the solid phase. By choosing a particular lattice configuration, the solid spontaneously chooses preferred positions for its molecules, formally called spontaneous breaking of translational invariance. (See Fig. 1.1.)

Remarkably, this paradigm of "spontaneous symmetry breaking" is incredibly general, and can be used to explain both classical and quantum phase transitions [1]. Solids break translational order, superfluids break global gauge symmetry, ferromagnets break rotational invariance. Generically, the broken-symmetry side of a phase boundary distinguishes itself from the unbroken phase by the presence of a non-zero

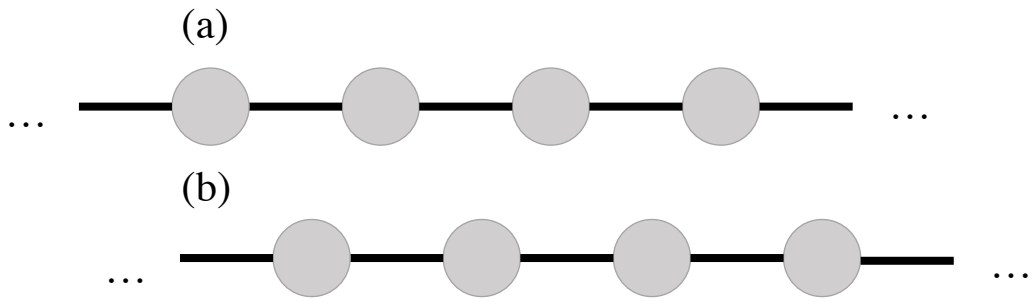

Figure 1.1 A solid spontaneously breaks translational symmetry. Particles pick preferred positions in real space to form a lattice (a). If we melt the solid, then freeze it again, different preferred positions will be selected at random (b).

"order parameter," an object which quantifies the degree of symmetry breaking in a phase. An effective field theory in terms of the order parameter and its variations in real space goes under the name Landau-Ginzburg statistical field theory [2], and can be used to make robust predictions. These ideas led to the development of Wilson's renormalization group approach [3], a method which explains universal behavior across systems with vastly different microscopic degrees of freedom.

Until the latter part of the last century, it was unclear whether a phase transition which defies the Landau-Ginzburg framework exists in nature. The first counterexample was uncovered in two-dimensional (2D) liquid Helium films. Experimentally, these materials exhibit a superfluid-to-normal fluid transition as a function of temperature [4]. This behavior was highly unexpected since Mermin and Wagner [5] (and Hohenberg [6]) rigorously demonstrated that spontaneous symmetry breaking of a continuous degree of freedom (such as the superfluid's global phase) cannot occur at any finite temperature in 2D due to large fluctuations which destroy the order. In a seminal work by Kosterlitz and Thouless [7] (and Berezinskii [8]), the authors demonstrated that by thinking of the problem in terms of topological defects known as vortices, the experimentally observed behavior could be explained. The BKT theory is widely hailed as the first example of a topological phase transition, since it was the first time that ideas of adiabaticity and topological equivalence were

used to explain a physical transition.

Soon thereafter, topological ideas were used to explain phase transitions in a completely different context. In 1980, von Klitzing experimentally found that a 2D electron gas has quantized transverse conduction plateaus as a function of applied magnetic field, known as the quantum Hall effect [9]. This behavior was elegantly explained by Thouless, Kohmoto, Nightingale, and den Nijs [10], who found that plateaus come in integer multiples of the so-called Chern number, which is a quantity calculated from the many-body ground state and can only be altered by closing the gap around the Fermi energy. These ideas paved the way towards our modern-day understanding of "topological insulators," although it took a few more revolutionary ideas along the way.

In 1988, Haldane constructed a tight-binding model on a graphene lattice which revealed remarkably similar physics to the quantum Hall effect without the need to apply an external magnetic field [11]. Specifically, the system was found to possess a non-trivial Chern number resulting in a quantized conductance due to the presence of gapless modes which propogate unidirectionally on the edge of the lattice. This model demonstrated that a tight-binding Hamiltonian can possess a non-trivial topological invariant. In 2004, Kane and Mele extended these ideas by demonstrating that the quantum Hall effect has a spinful cousin known as the quantum spin Hall effect, which again can be formulated on the lattice [12]. Bernevig, Hughes, and Zhang predicted this spin Hall effect to occur in physical materials (HgTe wells) [13] and the subsequent experimental observation was found within the year by the group of Molenkamp [14].

The 2016 Nobel Prize in Physics was awarded to Thouless, Kosterlitz, and Haldane, for their seminal contributions outlined above. Within the last 15 years, the study of topological phase transitions has been a central theme in the condensed matter research community. It is remarkable that such subtle properties were only recently uncovered in simple tight-binding models which, in principle, rely on only non-interacting quantum mechanics. Topological materials in 1, 2, and 3 dimen-

transition type	important theorem	consequences
symmetry-breaking	Goldstone	gapless modes
topological	bulk-boundary	gapless edge modes

Table 1.1: Goldstone's theorem guarantees gapless excitations for systems with a broken continuous symmetry (e.g. phonons in a solid due to broken translational invariance). Analogously, the bulk-boundary correspondence guarantees gapless *edge* excitations for non-trivial topological indices (e.g. edge modes in quantum Hall).

sions have been found experimentally [15, 16], and a symmetry-based classification was uncovered by Ryu *et al.* [17]. In addition to tight-binding models, the formalism applies equally well to quadratic *superconductors* in the Bogoliubov-de Gennes approximation.

On a theoretical level, physicists are fascinated by the notions of spontaneous symmetry breaking and topological invariants because there exist very general theorems which accompany these paradigms, summarized in Table 1.1. For models with global, continuous symmetry breaking, Goldstone's theorem ensures that for every symmetry generator broken, a gapless mode must be present [18]. Often times an effective theory concerning the gapless modes is enough to explain qualitative behavior at low temperatures for a variety of systems which break the same continuous symmetry. In analogy, the bulk-boundary correspondence states that non-trivial topological integers associated with a ground state correspond to the presence of edge modes which lie within the energy gap around the Fermi level. Physically, these modes can conduct even though the bulk is insulating. Thus an effective low-energy description often only involves edge modes.

Beyond fundamental science, topological ideas are currently being exploited to benefit quantum technology. A non-zero topological integer associated with an electronic ground state leads to: (1) eigenstates localized at the boundary of the sample with an energy which lies within the gap around the Fermi level (called gapless

edge modes), (2) quantization of observables (e.g. the Hall resistivity). The first feature is useful for "topological quantum computation": A qubit is represented as one of two degenerate (equal energy) ground states related via a gapless edge mode [19, 20]. The topological degeneracy prevents qubit dephasing which can arise from time-dependent variations in the energy splitting. The second feature is useful for quantum metrology: The Hall resistivity is directly proportional to the topological integer with a prefactor which is exactly h/e^2, experimentally accurate up to one part in 10^9 [21].

1.2 Motivation

While the major developments are outlined above, several mysteries remain in the details. Each chapter of this thesis concerns a different aspect of the general phenomenon of topological phase transitions. The central theme is to start with a paradigmatic topological model and perturb it in a novel way such that we may begin to observe qualitatively distinct behavior from what is perceived as standard.

As mentioned in the previous section, there are at least two very different types of transitions which classify as "topological" in the sense that they defy the Landau-Ginzburg paradigm of symmetry breaking:

1. Thermal phases induced by the proliferation of topological defects in the order parameter (e.g. BKT)

2. Ground state phases of electrons characterized by a global topological index calculated from the Bloch Hamiltonian (e.g. the Haldane model)

This thesis will be concerned with both. Of course, there are other definitions of topological phases of matter, most notably based on the presence or absence of long-range entanglement sometimes called intrinsic topological order (e.g. the fractional quantum Hall effect) [22]; we will not comment on transitions of this type. For the rest of this chapter, we will provide a brief discussion of these two topological transition types via explicit examples.

1.3 The two-dimensional Bose superfluid

In this section, we summarize the basic theory describing the 2D interacting Bose gas. Chapter 2 will build on this material, in light of unexpected results concerning the superfluid response of ^{4}He films adsorbed on graphite.

1.3.1 The Berezinskii-Kosterlitz-Thouless transition

Before the seminal work of BKT [7, 8], there was strong experimental evidence that 2D films of ^{4}He exhibit a phase transition from a normal fluid phase to a superfluid phase as a function of temperature [4]. This was highly unexpected, since Mermin and Wagner proved a no-go theorem which seemed to imply that the canonical description in terms of a spatially-varying order parameter would break down in two dimensions and lower [5]. Nevertheless, BKT borrowed this formalism and used it in an unconventional way to demonstrate that even in the absence of a symmetry-broken phase, qualitative features of the macroscopic system could change dramatically due to the proliferation of topological defects in the order parameter at high temperature. Here, we sketch the main results.

The order parameter of a superfluid is its macroscopic wavefunction

$$\psi(\mathbf{r}) = \left\langle \Psi \left| \hat{\psi}(\mathbf{r}) \right| \Psi \right\rangle = \sqrt{n(\mathbf{r})} e^{i\theta(\mathbf{r})} \tag{1.1}$$

where $|\Psi\rangle$ is the macroscopic coherent state, $\hat{\psi}(\mathbf{r})$ is the real-space particle annihilation operator, and $\psi(\mathbf{r})$ is the spatially-varying order parameter. We now make the further simplification that near a transition, the phase of the order parameter will vary much faster than the density modulation such that

$$\psi(\mathbf{r}) \approx \sqrt{\bar{n}} e^{i\theta(\mathbf{r})}. \tag{1.2}$$

We turn to a Landau-Ginzburg statistical field theory approach [23]. The partition function of the system is described via

$$Z = \int D\psi(\mathbf{r}) \exp[-\beta H(\psi(\mathbf{r}))], \tag{1.3}$$

where β is an effective inverse-temperature; we integrate over all possible field configurations and assign a probability to each one according to the Hamiltonian H. The probability of a given field configuration $\psi(\mathbf{r})$ is

$$P(\psi) = \frac{\exp[-\beta H(\psi(\mathbf{r}))]}{Z}. \tag{1.4}$$

If we suppress density modulations, the lowest-order symmetry-respecting Hamiltonian around the ordered state must be

$$-\beta H = -K\bar{n} \int d^d\mathbf{r} (\nabla\theta(\mathbf{r}))^2, \tag{1.5}$$

where we have expanded in lowest orders of the fluctuations in the phase, and temperature dependence is hidden in the factor $K(T)$. At this point, it is typical to expand the real-space phase fluctuations in terms of their Fourier components, in order to diagonalize the argument in the integrand above: $\theta(\mathbf{r}) = \sum_{\mathbf{q}} \exp(i\mathbf{q}\cdot\mathbf{r})\theta_{\mathbf{q}}$. Doing so leads to the canonical result

$$\lim_{r\to\infty} \langle \psi^*(\mathbf{r})\psi(\mathbf{0})\rangle = \begin{cases} c_0(T) & \text{for } d > 2 \\ 0 & \text{for } d \leq 2 \end{cases} \tag{1.6}$$

where c_0 is some temperature-dependent constant. The saturation of the infinite-range correlator is the mathematical definition of spontaneous symmetry breaking, sometimes called off-diagonal long-range order [24]. This specific calculation is a symptom of a more general result called the Mermin-Wagner theorem: Fluctuations around an ordered state destroy symmetry breaking of a continuous order parameter for dimensions $d \leq 2$ at finite temperature when interactions are short-ranged. In 2D, strict symmetry breaking is absent at any finite temperature in the thermodynamic limit.

It look the courage of BKT to probe this result further for $d = 2$. Although in the thermodynamic limit the long-range correlator must indeed go to zero, it will do so algebraically rather than exponentially in $d = 2$ at low temperature. This is sometimes called quasi-long-range order. A phase transition can occur, described by a transition from exponential to algebraic decay of the long-range correlator. In

order to explain this physically, we must consider topological defects in real space called vortices.

Rather than expand the partition function in terms of long wavelength fluctuations of the phase via Fourier transformation, we instead consider real-space phase configurations which form a vortex around some preferred position is taken to be $\mathbf{r} = 0$. (At the vortex core, the density of the wavefunction must be zero; otherwise the phase of the wavefunction is ill-defined. Away from this core, we assume the density is constant.)

Mathematically, the order parameter of the global phase of the wavefunction lives on a U(1) symmetry manifold. The order parameter at a given point $\mathbf{r}$ is a vector on the unit circle: $\mathbf{v}(\mathbf{r}) = [\cos\theta(\mathbf{r}), \sin\theta(\mathbf{r})]^T$; to get to another point on the manifold, we can apply a rotation matrix $R(\phi)$ to rotate $\mathbf{v}(\mathbf{r})$ by an amount ϕ. The two-dimensional rotation matrices $R(\phi)$ form a linear representation of the U(1) symmetry group (a compact, Abelian group parameterized by a single generator).

Along a loop in real space, each point will get mapped to a point on the U(1) order parameter manifold (unit circle). Any loop which encloses the vortex will necessarily trace out a full circle in order parameter space; conversely, if the loop does not enclose the vortex, then the loop will not trace a circle on the manifold of θ. This is depicted in the blue and red circles in Fig. 1.2, respectively. The statement that loops around vortices have a well defined winding number mathematically translates to: $\pi_1(\mathrm{U}(1)) = \mathbb{Z}$. The first homotopy group maps loops in real space to loops on a manifold and asks which ones can be smoothly deformed into each other.

Naively, we would expect that the formation of a single vortex must never arise, since the energetic cost of its creation must be quite large due to gradients of the overall phase. However, a single vortex configuration carries a significant entropic weight. Here, we provide a simple calculation analogous to the first KT paper [25] which explains why vortex configurations can arise at high temperatures.

Let us regularize the Hamiltonian by placing spins on a square lattice, and consider the contribution to the partition function from a configuration with a single vortex

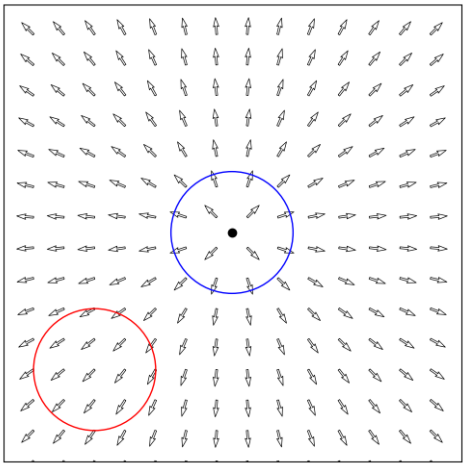

Figure 1.2 Vortex configuration of the order parameter $\theta(\mathbf{r})$. Real-space loops which enclose the vortex core at the origin (blue circle) *must* have a winding number of one on the U(1) order parameter manifold. Loops which do not enclose the origin (red) will have zero winding number.

at the origin

$$-\beta H(\psi_{1v}) = -\beta E_t - K\bar{n}\int_t^L d^2\mathbf{r}(\nabla\theta(\mathbf{r}))^2 \tag{1.7}$$

$$= -\beta E_t - K\bar{n}\int_t^L 2\pi r dr \left(\frac{1}{r}\right)^2 \tag{1.8}$$

$$= -\beta E_t - 2\pi K \ln\left(\frac{L}{t}\right), \tag{1.9}$$

where we have defined an arbitrary cutoff t which separates a region near the vortex core where the discreteness of the lattice matters $r < t$ which contributes some finite energy E_t, and a region where we are safe to make a continuum approximation $r > t$. In the region $r > t$, the phase is approximated as smoothly varying with a gradient which scales as r^{-1}. Indeed we see that the energetic cost of a vortex scales with system size and is infinite in the thermodynamic limit.

Let us now sum over all such vortex configurations, localized in different positions on the lattice

$$Z_{1v} \approx \left(\frac{L}{t}\right)^2 \exp\left[-2\pi K \ln\left(\frac{L}{t}\right)\right] \propto \left(\frac{L}{t}\right)^{2-2\pi K}. \tag{1.10}$$

The prefactor is a configurational entropy resulting from where we can place a single vortex configuration. Taking this into account, we see that a phase transition must

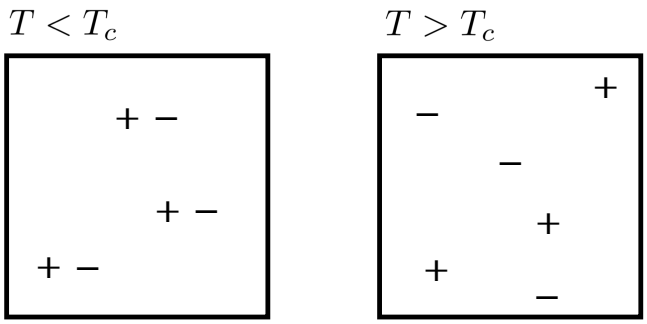

Figure 1.3 Phase configurations which contribute significantly to the partition function above and below T_c. The $\pm$ signs indicate vortices with ± 1 winding number. At low temperatures, vortices with opposite winding number pair up to form a dipole. At high temperatures, free vortices roam around the system. The binding/unbinding transition of vortex pairs is called the BKT transition, and is responsible for superfluidity in 2D ^{4}He films.

occur at $K_c = 1/\pi$ where a vortex configuration starts to contribute significantly to the partition function at $K < K_c$, i.e. high temperature. While the energy of a vortex is indeed large, so is the entropic contribution arising from its location. We thus find that the favorability of single vortex configurations will depend on the temperature of the system.

A more elaborate approach involves treating "positive" and "negative" vortices (i.e. ones with opposite winding number) as fundamental quantities and considering their interactions [7]. In 2D, the system resembles a charged Couloumb gas with interactions which scale logarithmically with distance. One can show that the phase transition between algebraic and exponential decay of the correlators occurs exactly at $K_c = 1/\pi$, in remarkable agreement with our heuristic analysis. Physically, the vortices form positive/negative bound pairs in the low temperature phase, whilst vortices unbind at high temperature, as depicted in Fig. 1.3.

The key insight of BKT was to expand the partition function in terms of topological defects (vortices) rather than microscopic degrees of freedom (local phase fluctuations). Thus they considered vortices as the "fundamental particles" of the

model. This could be achieved because vortices are topologically stable on the U(1) manifold, meaning that the winding number around a single vortex core is guaranteed not to change arbitrarily far away from its center. This is no longer true if the order parameter manifold has a more complicated structure, e.g. S^2. For the manifold S^2 (i.e. the surface of a sphere in 3D), the first homotopy group is trivial $\pi_1(S^2) = 0$, which implies that all loops can be contracted to a point. This is one mechanism for a superfluid to elude the famous BKT transition, which we will explore in Ch. 2.

1.3.2 Bogoliubov theory

The Landau-Ginzburg approach discussed in the previous section is only valid near the phase transition temperature T_c. At low temperatures near $T = 0$, it is useful to start thinking about the microscopic Hamiltonian governing the bosons. In this subsection, we discuss the Bogoliubov approximation to diagonalizing this microscopic Hamiltonian [26, 27], then discuss its predictions for the temperature scaling of observables.

Consider the 2D interacting Bose Hamiltonian

$$\mathcal{H} = \sum_{\mathbf{k}} \epsilon_{\mathbf{k}} b^\dagger_{\mathbf{k}} b_{\mathbf{k}} + \frac{1}{2L^2} \sum_{\mathbf{k},\mathbf{k}',\mathbf{q}} V_{\mathbf{q}} b^\dagger_{\mathbf{k}-\mathbf{q}} b^\dagger_{\mathbf{k}'+\mathbf{q}} b_{\mathbf{k}'} b_{\mathbf{k}}, \tag{1.11}$$

where $\epsilon_{\mathbf{k}} = \epsilon k^2$ is the quadratic kinetic energy, $V_{\mathbf{q}}$ is the Fourier transform of the interaction potential, L is the system size, and b are the bosonic operators in Fourier space. For neutral bosons like ^{4}He or ultracold atoms, it is often reasonable to approximate the interaction profile as a constant in Fourier space: $V_{\mathbf{q}} = V_0$, which represents a contact interaction in real space: $V(\mathbf{r}) \propto \delta(\mathbf{r})$. This involves s-wave scattering by $V(\mathbf{r})$, valid when the wavelengths involved are long compared to the range of $V(\mathbf{r})$.

The interaction term in (1.11) makes the Hamiltonian complicated to diagonalize exactly without resorting to numerical methods. We proceed by making the Bogoliubov approximation. Near $T = 0$ we expect a large occupation of the condensed

state at $k = 0$ due to a large number of bosons in the condensate. As such, we can approximate the operator $b_{k=0} \approx \sqrt{N_0}$, where N_0 represents the macroscopic number of bosons in the condensate. Making this approximation and keeping the terms of largest order in N_0, the Hamiltonian reads

$$\mathcal{H} = E_{mf} + \sum_{\mathbf{k}} \epsilon_{\mathbf{k}} b^\dagger_{\mathbf{k}} b_{\mathbf{k}} + \frac{nV_0}{2} \sum_{\mathbf{k}\neq 0} \left(2b^\dagger_{\mathbf{k}} b_{\mathbf{k}} + b^\dagger_{\mathbf{k}} b^\dagger_{-\mathbf{k}} + b_{\mathbf{k}} b_{-\mathbf{k}} \right) + O(\sqrt{N_0}/L^2), \quad (1.12)$$

where E_{mf} is a constant "mean-field" energy and $n \equiv N_0/L^2$ is the particle density. The second and third terms on the right-hand-side (RHS) of (1.12) compose the Bogoliubov Hamiltonian. This can be written succinctly in matrix form via

$$\mathcal{H}^{\text{Bog}} + \epsilon_{zp} = \frac{1}{2} \sum_{\mathbf{k}} \begin{pmatrix} b^\dagger_{\mathbf{k}} & b_{-\mathbf{k}} \end{pmatrix} \begin{pmatrix} \epsilon_{\mathbf{k}} + nV_0 & nV_0 \\ nV_0 & \epsilon_{-\mathbf{k}} + nV_0 \end{pmatrix} \begin{pmatrix} b_{\mathbf{k}} \\ b^\dagger_{-\mathbf{k}} \end{pmatrix} \quad (1.13)$$

$$\equiv \frac{1}{2} \sum_{\mathbf{k}} B^\dagger_{\mathbf{k}} H_{\mathbf{k}} B_{\mathbf{k}}, \quad (1.14)$$

where $\epsilon_{zp} = 1/2 \sum_{\mathbf{k}} (\epsilon_{\mathbf{k}} + nV_0)$ is a constant zero-point energy associated with the spectrum.

To diagonalize this quadratic Hamiltonian, we perform a Bogoliubov transformation into bosonic quasiparticles

$$B_{\mathbf{k}} = T_{\mathbf{k}} \tilde{B}_{\mathbf{k}}, \qquad B^\dagger_{\mathbf{k}} = \tilde{B}^\dagger_{\mathbf{k}} T^\dagger_{\mathbf{k}}, \quad (1.15)$$

where $B_{\mathbf{k}} = (b_{\mathbf{k}}, b^\dagger_{-\mathbf{k}})^T$ and $\tilde{B}_{\mathbf{k}} = (\beta_{\mathbf{k}}, \beta^\dagger_{-\mathbf{k}})^T$. If we impose that the quasiparticles obey bosonic commutation relations, then this implies a constraint on the transformation

$$T_{\mathbf{k}} \sigma_z T^\dagger_{\mathbf{k}} = \sigma_z, \quad (1.16)$$

where σ_i represents Pauli matrices. Additionally, the "particle-hole" symmetry: $H_{\mathbf{k}} = \sigma_x H^*_{-\mathbf{k}} \sigma_x$ imposes a structure

$$T_{\mathbf{k}} = \begin{pmatrix} u_{\mathbf{k}} & v_{\mathbf{k}} \\ v^*_{-\mathbf{k}} & u^*_{-\mathbf{k}} \end{pmatrix}. \quad (1.17)$$

We write the diagonalized Hamiltonian as

$$\mathcal{H}^{\text{Bog}} = \frac{1}{2} \sum_{\mathbf{k}} \tilde{B}^\dagger_{\mathbf{k}} \sigma_z \Lambda_{\mathbf{k}} \tilde{B}_{\mathbf{k}}, \qquad T^\dagger_{\mathbf{k}} H_{\mathbf{k}} T_{\mathbf{k}} = \sigma_z \Lambda_{\mathbf{k}}, \quad (1.18)$$

where $\Lambda_{\mathbf{k}}$ is a diagonal matrix. Equation (1.16) implies $T_{\mathbf{k}}^{-1} = \sigma_z T_{\mathbf{k}}^{\dagger} \sigma_z$, which leads to

$$\sigma_z H_{\mathbf{k}} t_{\mathbf{k},\mu} = \lambda_{\mathbf{k},\mu} t_{\mathbf{k},\mu}, \tag{1.19}$$

where $t_{\mathbf{k},\mu}$ is a column of $T_{\mathbf{k}}$ and $\lambda_{\mathbf{k},\mu}$ is a diagonal entry of Λ. The spectrum is found by solving for the eigenvalues of $\sigma_z H_{\mathbf{k}}$, and the transformation matrix columns $t_{\mathbf{k},\mu}$ correspond to the right eigenvectors. Once this transformation is achieved, the Hamiltonian takes the diagonal form

$$\mathcal{H}^{\text{Bog.}} = \sum_{\mathbf{k}} \left(E_{\mathbf{k}} \beta_{\mathbf{k}}^{\dagger} \beta_{\mathbf{k}} + \frac{1}{2} \right). \tag{1.20}$$

where the second term on the right represents the zero-point energy associated with the spectrum.

For the specific Hamiltonian (1.13), we find

$$E_{\mathbf{k}} = \sqrt{\epsilon_{\mathbf{k}} \left(\epsilon_{\mathbf{k}} + 2nV_0 \right)}, \qquad u_{\mathbf{k}}, v_{\mathbf{k}} = \pm \left(\frac{\epsilon_{\mathbf{k}} + V_0 n}{2E_{\mathbf{k}}} \pm \frac{1}{2} \right)^{1/2}. \tag{1.21}$$

This is a gapless mode (linear in k at long wavelengths) which is a consequence of Goldstone's theorem due to a spontaneously broken U(1) phase of the macroscopic wavefunction.

Within the Bogoliubov approximation, the interacting Bose Hamiltonian (1.11) is "exactly solvable," meaning that we can calculate any expectation value we wish by writing bosonic particles b in terms of bosonic quasiparticles β. The Hamiltonian is diagonal in β, and the interacting ground state is annihilated by all quasiparticles: $\beta_{\mathbf{k}} |\text{gnd}\rangle = 0$. We discuss two thermodynamic results which will be useful in the next chapter.

The density of bosons out of the condensate is given by

$$N_{nc} = \sum_{\mathbf{k} \neq 0} \left\langle b_{\mathbf{k}}^{\dagger} b_{\mathbf{k}} \right\rangle, \tag{1.22}$$

which we may rewrite in terms of Bogoliubov quasiparticles as

$$N_{nc} = \sum_{\mathbf{k} \neq 0} u_{\mathbf{k}}^* u_{\mathbf{k}} \left\langle \beta_{\mathbf{k}}^{\dagger} \beta_{\mathbf{k}} \right\rangle + v_{\mathbf{k}}^* v_{\mathbf{k}} \left\langle \beta_{\mathbf{k}} \beta_{\mathbf{k}}^{\dagger} \right\rangle \tag{1.23}$$

$$= \sum_{\mathbf{k} \neq 0} v_{\mathbf{k}}^* v_{\mathbf{k}} + \left(u_{\mathbf{k}}^* u_{\mathbf{k}} + v_{\mathbf{k}}^* v_{\mathbf{k}} \right) n_{\mathbf{k}} \tag{1.24}$$

where $n_{\mathbf{k}} = 1/(e^{\beta E_{\mathbf{k}}} - 1)$ is the Bose-Einstein distribution for the quasiparticle at wavevector $\mathbf{k}$, and $\beta = T^{-1}$. (We set Boltzmann's constant to unity.) At long wavelengths such that $E_{\mathbf{k}} \ll T$, the thermal factor may be approximated as $n_{\mathbf{k}\mu} \approx T/E_{\mathbf{k}}$. The first term only contributes at zero temperature

$$N_{nc}(T) - N_{nc}(T=0) = T \sum_{\mathbf{k}\neq 0} \left(\frac{|u_{\mathbf{k}}|^2 + |v_{\mathbf{k}}|^2}{E_{\mathbf{k}}} \right) \propto T \int_{L^{-1}}^{A(T)} \left(\frac{1}{k^2} \right) d^d\mathbf{k} \tag{1.25}$$

where $A(T)$ is a wavevector which scales linearly with temperature. We find that the number of uncondensed bosons is logarithmically divergent with system size L when $d = 2$. This is again a consequence of the Mermin-Wagner theory, which forbids a true condensate to form at any non-zero temperature in the thermodynamic limit.

We now proceed to quote the result for the normal fluid density ρ_n. In linear-response theory

$$\rho_n = \frac{2}{L^d Z} \lim_{\mathbf{q}\to 0} \sum_{mm'} \frac{e^{-\beta \mathcal{E}_m} |\langle m'| J_{\perp \mathbf{q}} |m\rangle|^2}{\mathcal{E}_{m'} - \mathcal{E}_m}\,, \tag{1.26}$$

where m labels many-body eigenstates with energies $\mathcal{E}_m$ of the interacting system described by a gas of Bogoliubov excitations with partition function Z [28]. We need the Fourier transform of the current operator $\mathbf{J}_{\mathbf{q}}$, in particular its component, $J_{\perp\mathbf{q}}$, transverse to the wavevector $\mathbf{q}$

$$J_{\perp\mathbf{q}} = \mathbf{J}_{\mathbf{q}} \cdot (\hat{\mathbf{z}} \times \hat{\mathbf{q}})\,, \qquad \mathbf{J}_{\mathbf{q}} = \sum_{\mathbf{p}} (\mathbf{p} - \tfrac{1}{2}\mathbf{q})\, b^\dagger_{\mathbf{p}-\mathbf{q}} b_{\mathbf{p}}\,. \tag{1.27}$$

A calculation similar to the previous paragraph leads to

$$\rho_n(T=0) = 0, \qquad \rho_n(T) \propto T \int_{L^{-1}}^{A(T)} d^d\mathbf{k} \propto T^{d+1}. \tag{1.28}$$

The zero-temperature result is a consequence of Galilean invariance via the famous Landau argument for superfluidity. The 2D system is predicted to be a perfect superfluid at $T = 0$, with a normal fluid density which scales as T^3. Thus even though there is no condensation in $d = 2$, the normal fluid density is finite at any temperature T. Superfluidity can exist in the absence of symmetry breaking, in agreement with the BKT analysis.

1.4 Symmetry-protected topological phases

Beyond Ch. 2, the rest of this thesis deals with a subject called "symmetry-protected topological phases," which describes ground state phases of electrons in equilibrium. In this section, we review some of the basic ideas concerning the geometrical phase. We then apply these ideas to the Su-Schrieffer-Heeger model [29] and the Haldane model [11], followed by a general discussion between the interplay of symmetry with topology.

1.4.1 The Berry phase

The concept of a geometric phase is of central importance in the theory of topological insulators. Consider a Hamiltonian matrix parameterized by some value $\mathbf{x}$. For every $\mathbf{x}$, we write the associated eigenvectors and eigenvalues as

$$H(\mathbf{x})\psi(\mathbf{x}) = E(\mathbf{x})\psi(\mathbf{x}). \tag{1.29}$$

Consider what happens when we prepare a particle in an eigenstate of $H(\mathbf{x})$ at a time t_i, then vary the parameter $\mathbf{x}(t)$ slowly in time. We consider a closed loop in parameter space such that at the final time $t = t_f$ the parameter $\mathbf{x}$ returns to the original value: $\mathbf{x}(t_i) = \mathbf{x}(t_f)$. If the spectrum of the Hamiltonian $H(\mathbf{x})$ is non-degenerate throughout this process, what is the phase accumulated by the wavefunction $\psi(\mathbf{x})$? The initial and final wavefunctions are related by the phase

$$\psi(\mathbf{x}(t_f)) = e^{i(\theta_{\text{dyn.}}+\theta_{\text{geo.}})}\psi(\mathbf{x}(t_i)), \tag{1.30}$$

where $\theta_{\text{dyn.}} = -\int_{t_i}^{t_f} E_0(\mathbf{x}(t))dt$ is the dynamical phase accumulated due to energetic contributions (we set $\hbar = 1$), and

$$\theta_{\text{geo.}} = i\int \psi^\dagger(\mathbf{x})\nabla_{\mathbf{x}}\psi(\mathbf{x})\cdot d\mathbf{x}, \tag{1.31}$$

is the geometrical (Berry) phase associated with the path taken in parameter space $\mathbf{x}$ [30]. The quantity $\mathbf{A}(\mathbf{x}) = \psi^\dagger(\mathbf{x})\nabla_{\mathbf{x}}\psi(\mathbf{x})$ is called the Berry connection.

While this analysis is true for any closed loop in parameter space, Zak was the first to notice its relevance to band theory [31]. In the theory of non-interacting

electrons in a periodic potential, eigenstates are labeled by a Bloch wavevector in the first Brillouin zone $\mathbf{k}$ such that k_i is only meaningful between $[0, 2\pi)$, e.g. for a square lattice. In one-dimension, this quantity is simply a scalar k. Zak noticed that bands can have non-zero geometrical phases associated with an adiabatic path in parameter space which sends $k_0 \to k_0 + 2\pi$ as a function of time. For 1D Brillouin zones, this geometric phase is called the Zak phase.

1.4.2 The first Chern number

The Berry phase is a geometric quantity associated with a loop in parameter space, which is a suitable object to associate with a band in 1D. In 2D, the Brillouin zone is a torus, mapped out by the quasimomenta $k_x, k_y \in [0, 2\pi)$. Is there a geometrical object which we can associate with this closed, orientable surface?

The Chern number of a given (non-degenerate) band is defined as

$$\nu = -\frac{1}{2\pi} \int_{BZ} dk_x dk_y \left(\nabla \times \mathbf{A}(\mathbf{k})\right)_z . \tag{1.32}$$

The integrand in the equation above is known as the Berry curvature. (Unlike the Berry connection, the Berry curvature is gauge invariant.) The Berry curvature at a given point $\mathbf{k}'$ is the Berry phase of an infinitesimal loop around this point in parameter space. The sum of these Berry phases around a closed surface must be an integer times 2π. This is because every side of a loop is an internal edge which contributes an opposite amount in the adjacent loop, hence the exponent of the summed Berry phases must be one. Thus a crucial difference between the Berry phase and the Chern number is that the latter is guaranteed to be quantized in integer units on a closed, orientable surface. The Chern number is the topological invariant associated with the ground state of the quantum Hall Hamiltonian and the Haldane model [10].

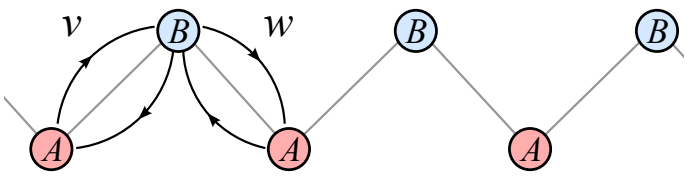

Figure 1.4 Schematic diagram of the SSH chain. Electrons hop to nearest-neighbors on a bipartite lattice with intracell hopping v and intercell hopping w. This is an example of a 1D topological insulator, capable of hosting gapless edge modes at the boundary.

1.4.3 The Su-Schrieffer-Heeger model

While topological insulators were first predicted to occur in 2D materials, it is conceptually simpler to think about 1D models which exhibit analogous behavior. We begin by studying the simplest example of a 1D topological insulator, called the Su-Schrieffer-Heeger (SSH) model which historically served as a minimal description of polyacetylene [29]. In the next subsection, we discuss the 2D Haldane model [11].

Consider a 1D system of non-interacting, spinless fermions on a bipartite lattice, described by the Hamiltonian

$$\mathcal{H} = v \sum_{i=1}^{N} \left(c_{A,i}^{\dagger} c_{B,i} + h.c. \right) + w \sum_{i=1}^{N-1} \left(c_{B,i}^{\dagger} c_{A,i+1} + h.c. \right), \tag{1.33}$$

where $c_{A/B,i}$ annihilates a fermion on lattice site i in sublattice A/B, v represents hopping within the unit cell, and w represents hopping between unit cells, $v, w \in \mathbb{R}$. (See Fig. 1.4.)

If we impose periodic boundary conditions on this model, then we can rewrite (1.33) in terms of Bloch wavefunctions: $c_{A/B,k} = 1/\sqrt{N} \sum_{m=1}^{N} e^{imk} c_{A/B,j}$. (We set lattice spacing to unity.) The Hamiltonian takes the simple form:

$$\mathcal{H} = \begin{pmatrix} c_{A,k}^{\dagger} & c_{B,k}^{\dagger} \end{pmatrix} \begin{pmatrix} 0 & \alpha_k \\ \alpha_k^{*} & 0 \end{pmatrix} \begin{pmatrix} c_{A,k} \\ c_{B,k} \end{pmatrix}, \qquad \alpha_k = v + we^{-ik}. \tag{1.34}$$

We can rewrite this more compactly as: $\mathcal{H} = \mathbf{c}_k^{\dagger} H(k) \mathbf{c}_k$, where $H(k)$ is called the first-quantized Bloch Hamiltonian. The spectrum is found by diagonalizing

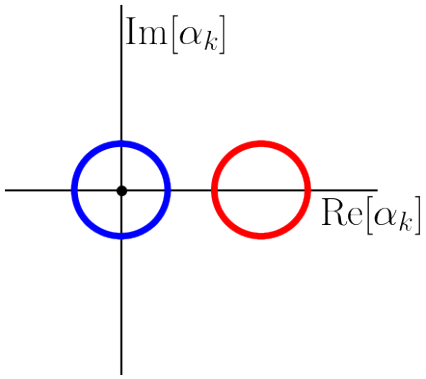

Figure 1.5 The trajectory of α_k for $k \in [0, 2\pi)$ in the complex plane for $v < w$ (blue) and $v > w$ (red). The winding number around the origin can only change if the loop passes through the origin ($v = w$), indicating a band crossing.

$H(k)$ which results in the dispersion: $E(k) = \pm|\alpha_k|$. We notice that the Bloch Hamiltonian (and consequently the spectrum) is completely specified by this one parameter, α_k. Moreover, this parameter has a unique winding number: If we plot the loop traced out by Re$[\alpha_k]$ against Im$[\alpha_k]$ in the 2D plane as we vary $k \in [0, 2\pi)$ then the number of times that α_k winds around the origin is a topological invariant in the sense that any smooth deformation in the parameters v, w which preserve a band gap will ensure that this integer will not change. This is plotted in Fig. 1.5. We notice that for $v < w$ the winding number is one, while it is zero in the opposite limit. A topological phase transition occurs at $v = w$ when this integer changes discontinuously.

We can associate a non-zero winding number with a non-zero, quantized Zak phase of the lowest energy band (which is completely filled in the ground state). The eigenvectors of $H(k)$ are:

$$\psi_k^{\pm} = \frac{1}{\sqrt{2}} \begin{pmatrix} 1 \\ \pm e^{i\phi_k} \end{pmatrix}, \qquad e^{-i\phi_k} = \frac{\alpha_k}{|\alpha_k|} \tag{1.35}$$

Using this expression, the Zak phase of the lower band is

$$\theta_{\text{geo.}} = -\frac{1}{2} \int_0^{2\pi} \frac{d\phi_k}{dk} dk = -\frac{1}{2} \left(\phi_k |_{k=0}^{k=2\pi} \right). \tag{1.36}$$

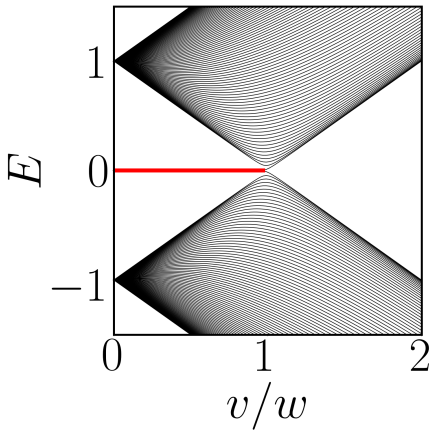

Figure 1.6 Spectrum of the SSH Hamiltonian (1.33) with open boundary conditions as a function of v/w. Edge modes (red) have exactly zero energy, and only appear when $v/w < 1$.

Since the eigenvectors ψ_k must be single-valued across the Brillouin zone, ϕ_k can only vary by integer multiples of 2π across the Brillouin zone. This implies that the geometric phase is strictly quantized in units of π, $\theta_{\text{geo.}} = n\pi$. Moreover, the coefficient n is exactly the winding number of the Bloch Hamiltonian discussed in the previous paragraph.

As mentioned in the introduction, a general principle of topological insulators is the bulk-boundary correspondence, which roughly states that non-trivial topological integers calculated from the Bloch Hamiltonian will correspond to gapless boundary modes in the finite system (i.e. without periodic boundary conditions). This is indeed the case for the SSH model. If we impose *open* boundary conditions, then the spectrum of (1.33) is given in Fig. 1.6. For a chain which starts with a v link in a parameter regime $v < w$, there exists an eigenstate localized at the edge which has exactly zero energy. The mode at the boundary can only be adiabatically removed once a bulk mode becomes degenerate with it, which only occurs when the Bloch spectrum hits zero (and hence at a band closing point).

As presented in this subsection, the topological features appear rather contrived and highly dependent on the specific form of the SSH Hamiltonian. What terms can we add to the Hamiltonian which would keep the winding number well defined?

What terms preserve the quantization of the Zak phase? Why do eigenstates at the edge have to possess zero energy? It turns out that the SSH Hamiltonian has a "chiral" symmetry which can elegantly explain all of these features. In subsection 1.4.6, we will aim to describe topological phases through the lens of Altland-Zirnbauer symmetries [32].

1.4.4 The Haldane model

In the previous subsection, we discussed the SSH model which is the simplest Hamiltonian which obeys the paradigm of "topological band theory," summarized below

1. The negative energy Bloch band (which is completely filled in the ground state) had a non-zero topological integer i.e. the Zak phase.

2. The quantized invariant could not change smoothly, but only by discrete steps at a band crossing (degeneracy).

3. In a finite geometry, the bulk invariant predicted the presence of eigenstates localized at the boundary of the system with an energy within the insulating gap.

Topological materials which obey this general framework can be found in arbitrary dimensions. We now discuss the simplest example in 2D, called the Haldane model.

To described the Haldane model [11], we begin by considering electrons hopping on a 2D honeycomb lattice like the one depicted in Fig. 1.7. There are two degrees of freedom within the unit cell (labeled A and B), hence the eigenstates form two Bloch bands. (Any minimal description of a topological material must have two bands in order to form an energy gap.) The Hamiltonian is

$$\mathcal{H} = \sum_j \mu_j c_j^\dagger c_j - \sum_{\langle i,j\rangle} \left(t_1 c_i^\dagger c_j + h.c. \right) - \sum_{\langle\langle i,j\rangle\rangle} \left(t_2 e^{i\phi} c_i^\dagger c_j + h.c. \right) \tag{1.37}$$

where $\mu_j = +\mu$ on A sublattice sites, $\mu_j = -\mu$ on B, and $\mu, t_1, t_2, \phi \in \mathbb{R}$. t_1 represent hopping between nearest neighbors and t_2 between next-nearest neighbors. The

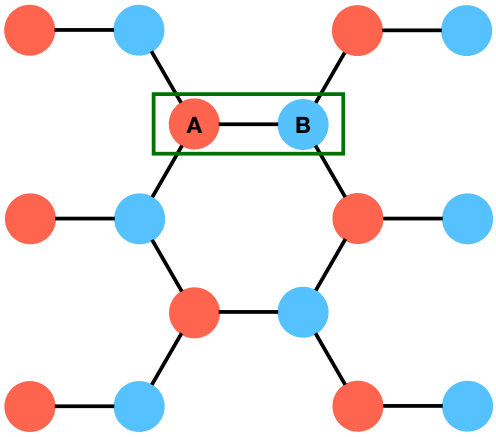

Figure 1.7 A honeycomb lattice, with sublattice sites A (red) and B (blue) in each unit cell (green). In the Haldane model, electrons can hop between nearest neighbors and next-nearest neighbors, and experience a staggered sublattice potential.

presence of a non-zero ϕ term breaks time-reversal symmetry and cannot be gauged away.

We impose periodic boundary conditions and calculate the bulk spectrum with Bloch's theorem. The Brillouin zone forms a torus, labeled by momenta k_x and k_y. Thus we can calculate the Chern number associated with the lowest energy band, with a phase diagram given in Fig. 1.8. The Chern number can be non-zero and will only change when bulk bands become degenerate, in direct analogy with the Zak phase of the SSH model.

What is the consequence of a non-trivial Chern number? Again, a non-trivial band topology leads to the presence of eigenstates localized at the edge of the sample. This is depicted in Fig. 1.9 for topological and trivial parameter regimes in a semi-infinite, cylindrical geometry.

1.4.5 Symmetry and Topology: The Tenfold way

Long before the rise of topological ideas in condensed matter, physicists utilized symmetries to constrain the spectral properties in disordered many-body systems via random matrix theory. Dyson started this program by introducing a three-fold

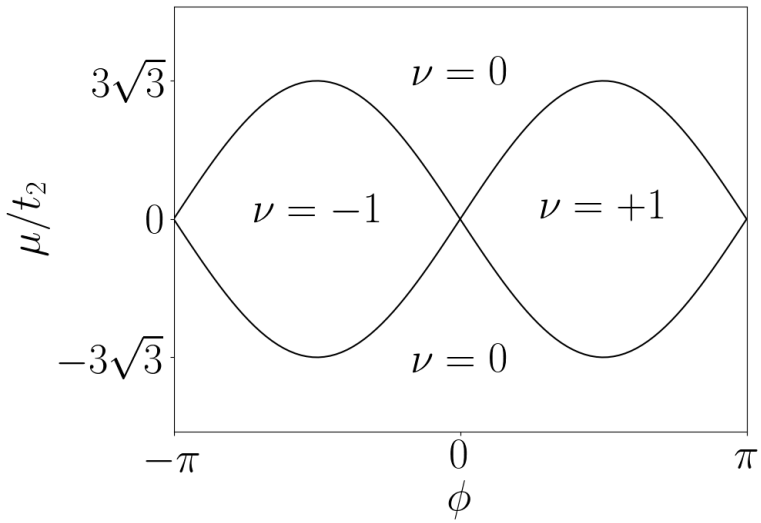

Figure 1.8 Phase diagram of the Haldane model with $|t_2/t_1| < 1/3$. The Chern number ν can be non-zero, and changes abruptly whenever the bandgap closes at $\mu/t_2 = 3\sqrt{3}|\sin\phi|$. A non-trivial Chern number indicates the presence of gapless edge modes.

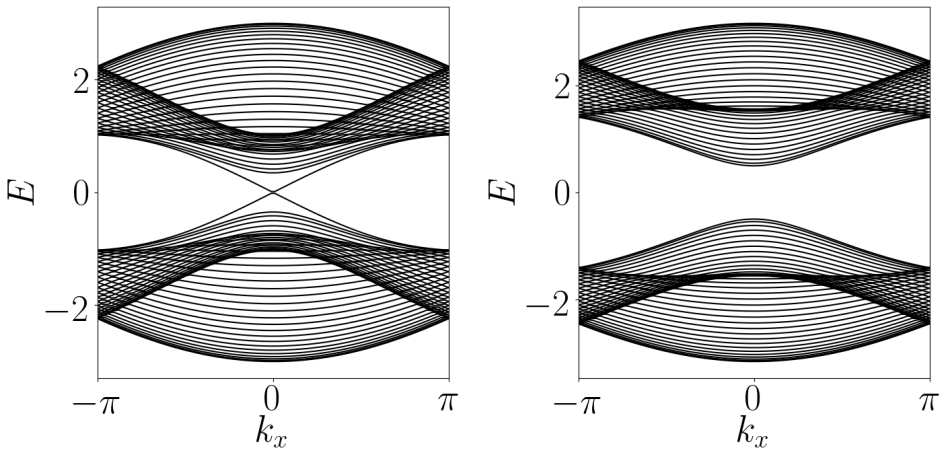

Figure 1.9 Spectrum of the Haldane model in an "armchair" cylindrical geometry with periodic boundary conditions in x and finite slab in y. Parameter values: $\mu/t_1 = 0.2, t_2/t_1 = 0.1, \phi = \pi/2$ (left); $\mu/t_1 = 1, t_2/t_1 = 0.1, \phi = \pi/2$ (right). Edge modes live in the band gap in the topological phase (left). In the trivial phase (right), the system is a normal insulator.

way based on the presence of time-reversal symmetry (TRS) [33]

$$H = U_T H^* U_T^\dagger, \qquad U_T U_T^* = \pm\mathbb{I}. \tag{1.38}$$

A system can either break TRS (e.g. by applying a magnetic field), have $U_T U_T^* = +\mathbb{I}$ "bosonic" TRS, or have $U_T U_T^* = -\mathbb{I}$ "fermionic" TRS. Imposing such constraints on the random matrix Hamiltonian results in non-trivial predictions concerning the energy level statistics, in good agreement with experimental measurements on atomic nuclei.

Many years later, Altland and Zirnbauer observed that fermionic superconductors in the Bogoliubov-de Gennes approximation fall outside of Dyson's three universality classes [32]. This is due to the inherent particle-hole symmetry which imposes an additional constraint on the random matrix problem

$$H = -U_C H^* U_C^\dagger, \qquad U_C U_C^* = \pm\mathbb{I}. \tag{1.39}$$

This resulted in four new classes with a built-in particle-hole symmetry and time-reversal: $U_T^2 = \pm\mathbb{I}, U_C^2 = \pm\mathbb{I}$, and two new classes with just particle-hole symmetry: $U_C^2 = \pm\mathbb{I}$, expanding the number of universality classes to nine.

The final class needed to complete the Tenfold way requires the definition of chiral symmetry

$$H = -U_S H U_S^\dagger, \qquad U_S^2 = \mathbb{I}. \tag{1.40}$$

This symmetry can exist alone in the absence of time-reversal and particle-hole symmetry.

Separate from these developments, early investigations of topological insulators were heavily influenced by symmetry considerations. Haldane postulated that broken time-reversal symmetry (not a net magnetic field) was fundamental in preserving the topological features of the quantum Hall state, leading to the next-nearest neighbor terms in his canonical tight-binding model. Restoring time-reversal led to the $\mathbb{Z}_2$ quantum spin Hall state. As the field of topological free fermions grew in the early 2000s, it became apparent that non-unitary symmetries (i.e. ones that do not

simply block diagonalize the Hamiltonian) were extremely important in protecting the topological characteristics of bulk invariants and edge modes.

The bridge which connects the ten Altland-Zirnbauer (AZ) symmetry classes to their respective topological classification is called the Tenfold way, a triumph of mathematical physics initiated by Kitaev [34] and completed by Ryu *et al.* [17]. The chart summarizing these results is given in Table 1.2. Deriving this chart from first principles is mathematically challenging, but understanding its consequences is simple: For a given symmetry class (labeled by the letters), in a given dimension, the chart tells us how many topologically distinct ground states exist in the class: one, two, or countably infinite, indicated by 0 , $\mathbb{Z}_2$, and $\mathbb{Z}$ respectively. All topological band insulators/superconductors (which are not protected by spatial symmetries) are included in this chart. For reference, we note the Haldane model is class A in $d = 2$, characterized by an integer invariant $\mathbb{Z}$, corresponding to the Chern number of the filled bands. While this chart is elegantly derived using the machinery of K-theory and Clifford algebras, these methods do not provide us with much physical intuition. In the next couple of subsections, we study the interplay of symmetry and topology through the lens of bulk invariants and gapless boundary modes.

1.4.6 Symmetry constraints on bulk invariants

Bulk invariants are integers which are associated with the Bloch Hamiltonian of a model. In this subsection, we provide two examples where imposing symmetries on a Hamiltonian will influence the values that these integers can assume.

Let us revisit a 1D, two-band Bloch Hamiltonian (e.g. SSH) parameterized by a single momentum label k

$$H(k) = \begin{pmatrix} A_k & B_k \\ B_k^* & -A_k \end{pmatrix}, \tag{1.41}$$

where we impose Hermiticity but otherwise keep the model general, $A \in \mathbb{R}, B \in \mathbb{C}$. (We exclude a term proportional to the identity.) We now impose a chiral symmetry

class	TRS	PHS	chiral	$d=1$	$d=2$	$d=3$
A	0	0	0	0	$\mathbb{Z}$	0
AI	+1	0	0	0	0	0
AII	−1	0	0	0	$\mathbb{Z}_2$	$\mathbb{Z}_2$
AIII	0	0	1	$\mathbb{Z}$	0	$\mathbb{Z}$
BDI	+1	+1	1	$\mathbb{Z}$	0	0
CII	+1	−1	1	$\mathbb{Z}$	0	$\mathbb{Z}_2$
D	0	+1	0	$\mathbb{Z}_2$	$\mathbb{Z}$	0
C	0	−1	0	0	$\mathbb{Z}$	0
DIII	−1	+1	1	$\mathbb{Z}_2$	$\mathbb{Z}_2$	$\mathbb{Z}$
CI	+1	−1	1	0	0	$\mathbb{Z}$

Table 1.2: The Tenfold way table which relates non-unitary symmetry classes (on the left) to the presence or absence of topologically distinct ground states in a given dimension d. For example, the Haldane state (characterized by an integer-valued $\mathbb{Z}$ Chern index) is class A in 2D.

on the Hamiltonian: $H_k = -\sigma_z H_k \sigma_z$. This constrains the matrix to obey the form

$$H(k) = \begin{pmatrix} 0 & B_k \\ B_k^* & 0 \end{pmatrix}. \tag{1.42}$$

The Hamiltonian is parameterized by a single complex variable and has eigenvalues $\pm|B_k|$. It is now possible to define a topological invariant: The winding number of B_k will trace out a loop in the complex plane as we vary $k \in [0, 2\pi)$. The number of times that this loop winds around the origin ($B_k = 0$) is a topological invariant since it cannot change without closing a gap in the Bloch spectrum. (See Fig. 1.5.)

We find that imposing chiral symmetry in 1D results in a well defined winding number, in agreement with the $\mathbb{Z}$ classification from the Tenfold way. In the absence of chiral symmetry, the winding number is no longer well defined. The Hamiltonian can have a term $A_k\sigma_z$ with real coefficient A_k, such that it is parameterized by three real numbers: $\mathrm{Re}[B_k], \mathrm{Im}[B_k], A_k$. The third dimension allows the loop to be lifted out of the plane, such that all loops can be deformed into each other without every closing a band gap, i.e. by avoiding the origin. Without chiral symmetry (class A), all 1D models are topologically equivalent.

Imposing a symmetry can also be used to reduce the number of topologically distinct ground states. A 2D system in the presence of fermionic spin-1/2 time-reversal symmetry (e.g. quantum spin Hall) will ensure that the sum of the Chern numbers of negative-energy bands must be zero: $\nu_\uparrow + \nu_\downarrow = 0$. A 2D TRS system can still exhibit topological protection (via the "spin-Chern number," $\nu_\uparrow - \nu_\downarrow \neq 0$), but it is characterized by a $\mathbb{Z}_2$ invariant.

1.4.7 Symmetry constraints on boundary modes

In the last subsection, we found that the AZ symmetries play an important role in constraining the values of bulk topological invariants, i.e. integer-valued quantities calculated from the Bloch Hamiltonian which can only change when the band gap closes. Below, we will show that these symmetries also have a direct consequence

on the stability of gapless boundary modes in a finite geometry (i.e. where crystal momentum is no longer a good quantum number).

Again, let us consider a 1D system and impose a chiral symmetry: $H = -\tau_z H \tau_z$, where this time we consider a $2N \times 2N$ Hamiltonian matrix representing a real-space finite chain of length N, and $\tau_z = \mathbb{I}_N \otimes \sigma_z$. We now imagine that the spectrum is gapped around $E = 0$, apart from a single mode localized on the left side of the chain with energy $E = 0$. Additionally, we suppose that this mode must satisfy $\psi^+_{\text{edge}} = +\tau_z \psi^+_{\text{edge}}$, which ensures that its energy must be exactly zero due to the chiral symmetry. How can this edge mode be removed from zero energy? In order to do so, it must couple with another degenerate eigenvector such that the chiral operator acting on one state will give an orthogonal state: $\tau_z \psi_1 = \psi_2, E_1 = -E_2 \neq 0$. This can only be achieved if either: (1) there exists another mode at the same edge will opposite chirality $\psi^-_{\text{edge}} = -\tau_z \psi^-_{\text{edge}}$ such that $\psi^\pm_{\text{edge}}$ can form a linear combination with nonzero energy, or (2) the bulk gap closes at zero energy, and the localization length of the edge mode diverges to adiabatically become a bulk mode. We find that the quantity $N^+ - N^-$ is a topological invariant: As long as the bulk gap remains open, the difference in the number of edge modes on one side of the chain with $+1$ chiral eigenvalue vs. edge modes with -1 chiral eigenvalue must remain constant [35].

Now let us turn to a 2D time-reversal symmetric system, such as the quantum spin Hall insulator. We impose a time-reversal symmetry for the Bloch Hamiltonian in a cylindrical geometry, where we keep the system finite in y but consider periodic boundary conditions in x. Time reversal symmetry is represented as: $H(k_x) = U_T H^*(-k_x) U_T^\dagger$ with $U_T U_T^* = -\mathbb{I}$ due to the spin-1/2 nature of the fermions. The $U_T U_T^* = -\mathbb{I}$ flavor of time-reversal symmetry guarantees a Kramers degeneracy, which states that all eigenvalues must be at least two-fold degenerate. This has very interesting implications for edge modes at high-symmetry points in the Brillouin zone, with an energy in the bandgap: For every eigenstate $\psi_{\text{edge},\uparrow}(k_x = 0)$ with energy $E(k_x = 0)$, there must be another *orthogonal* eigenstate $\psi_{\text{edge},\downarrow}(k_x = 0)$ at

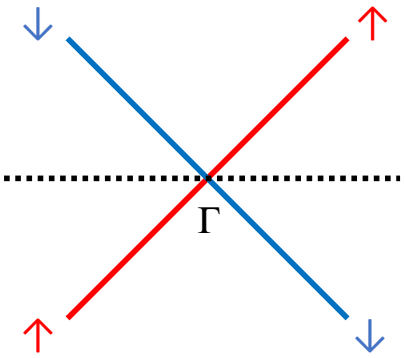

Figure 1.10 Schematic diagram of spin-up (red) and spin-down (blue) edge-mode dispersion near the high-symmetry point (Γ) of the Brillouin zone for a system with semi-periodic boundary conditions. The band crossing is protected at Γ due to Kramers theorem.

the same edge with the same energy. Moreover, due to the TRS symmetry which relates dispersion at $+k$ to $-k$, these two edge modes must have opposite group velocity: $\partial E_{\uparrow}(k_x)/\partial k_x|_{k_x=0} = -E_{\downarrow}(k_x)/\partial k_x|_{k_x=0}$. This is depicted in Fig. 1.10. The TRS is directly responsible for the quantum spin Hall effect: Spin-up edge modes conduct in the opposite direction from spin-down edge modes on the same edge [12].

1.5 Structure of the thesis

Having introduced the canonical models and central concepts, we are in a position to outline the novel results contained in this thesis. The structure is as follows:

- In Chapter 2, we study a two-dimensional Bose gas which eludes the BKT transition due to the absence of topologically stable vortices. The order parameter manifold is generated by operators which obey an SU(3) algebra, which results in anomalous Goldstone modes and qualitatively unique thermodynamic response. While our study was motivated by solid-state experiments, we discuss possible implementations using dipolar-interacting cold atoms.

- In Chapter 3, we study the effects of strong disorder on the paradigmatic Kitaev chain: The simplest example of a topological superconductor which

hosts Majorana mode excitations. Is topological band theory well defined once translational invariance is lost? We show that disorder which keeps the Hamiltonian in the same AZ symmetry class can both promote and reduce topological indices in a model with $\mathbb{Z}$ classification.

- From Chapter 4 onwards, the thesis will focus on borrowing topological ideas to constrain the behavior of non-equilibrium systems. Chapter 4 introduces the concept of "non-Hermitian symmetry protected topological phases" by highlighting the Bernard-LeClair (BL) classes which generalize the canonical Altland-Zirnbauer classes in the absence of Hermiticity. We discuss physical setups where the BL symmetries arise naturally.

- In Chapter 5, we make the analysis of the previous chapter more concrete by studying three different non-Hermitian Su-Schrieffer-Heeger models: the chirally-symmetric, PT-symmetric, and bosonic-SSH models.

- In Chapter 6, we present unpublished work concerning a robust degeneracy of steady states in a dissipative two-level system using the framework of non-Hermitian topology. The Ising model in the presence of a complex transverse field is studied from the perspective of Majorana modes in a Kitaev chain. We derive a phase diagram which defines a parameter region with guaranteed two-fold degeneracy in the dynamical (complex) spectrum.

- We conclude the thesis by summarizing the main achievements and commenting on future directions in Chapter 7.

Chapter 2

Intertwined superfluidity and density wave order

Recent experiments on ^{4}He films adsorbed on graphite suggest a temperature-dependent superfluid response which defies conventional BKT behavior [36]. Motivated by these results, we study a two-dimensional (2D) superfluid which violates the assumptions necessary for a BKT transition due to an enlarged symmetry manifold which does *not* support vortex excitations.

Specifically, we consider a continuum model of the weakly interacting Bose gas in the presence of an external potential with minima on a triangular lattice potential. The non-interacting spectrum admits a global energy minimum at the Γ point in the Brillouin zone; however, the first excited band has minima at the M points (at the edge of the Brillouin zone). We consider a metastable BEC which condenses at the M points and find that in the presence of certain finite-range interactions, the space of degenerate coherent states is isomorphic to S^5. The symmetry generators of the degenerate manifold are non-Abelian, which has several physical consequences. Firstly, vortex configurations of the overall phase can be smoothly undone. This implies that the usual mechanism to achieve superfluidity in a 2D Bose gas (i.e. vortex-antivortex pairing) is expected to fail. Secondly, the enlarged number of symmetry generators results in an unconventional number and type of

Goldstone modes. We show that these anomalous gapless modes affect the thermodynamic response of the temperature-dependent superfluid density (calculated within the Bogoliubov approximation), suggesting that superfluidity is a finite-size effect in a 2D non-Abelian condensate. Corrections beyond mean-field theory reduce the S^5 degeneracy to a smaller manifold due to zero-point fluctuations. This "order-by-disorder" splitting is found to be weak compared to other energy scales in the model. While our setup does not serve as a realistic model to describe ^{4}He on graphite, our analysis suggests that a macroscopic wavefunction with intertwined superfluidity and density wave order shares qualitative features observed in experiment.

2.1 Experimental motivations

The predictions of BKT theory were experimentally verified to great accuracy using torsional oscillator experiments on 2D ^{4}He films [4]. Helium atoms are placed inside a chamber which proceeds to rotate. Experimentalists measure the moment of inertia of the chamber as a function of the temperature of the helium. The normal fluid contributes to the moment of inertia, while the superfluid does not. This procedure leads to an accurate measurement of the superfluid density as a function of temperature.

Recent experiments at Royal Holloway, University of London have revisited these canonical experiments, with a slight twist. Helium atoms were placed on a graphite substrate, and various density regimes were probed. At certain density regimes corresponding to bilayer formation, Nyeki *et al.* found striking results which suggest an unconventional superfluid response which violated predictions from BKT theory [36]. This phase is characterized by: (1) a superfluid density which increases smoothly from zero at the critical temperature, rather than exhibiting a "universal jump" which is characteristic of a BKT transition, and (2) the superfluid fraction at low temperature T scales linearly with T, rather than the conventional T^3 depen-

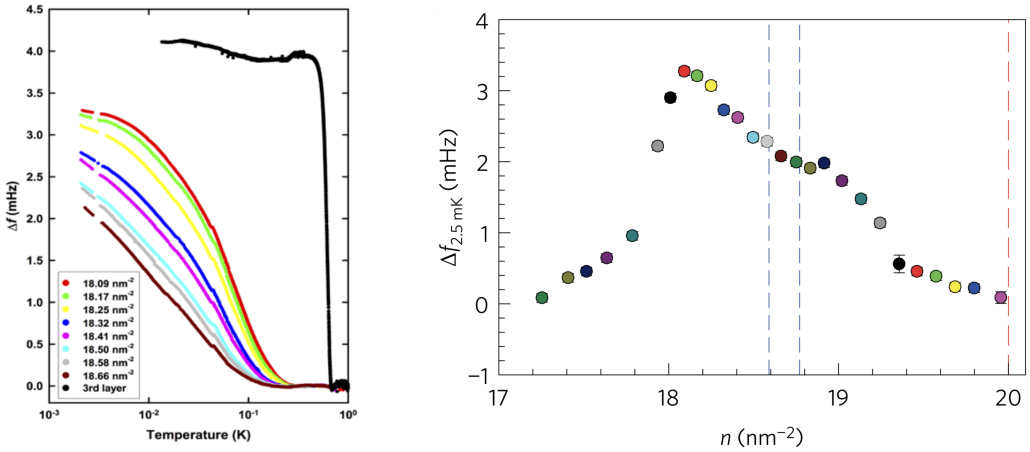

Figure 2.1 *Left*: The frequency shift of a torsional oscillator (directly proportional to the superfluid density) vs. the temperature for a variety of ^{4}He densities on a graphite substrate. The trilayer densities exhibit conventional BKT response (black), while bilayer densities exhibit anomalous behavior: (1) a smooth onset of the superfluidity, (2) a linear temperature dependence near $T = 0$. *Right*: Isotherm ($T = 2.5$ mK) of frequency shift for a range of helium densities. The unconventional behavior occurs at bilayer densities, with the dashed red line indicting promotion to trilayer coverage. Dashed blue lines indicate a bilayer density regime where an incommensurate solid phase is expected to occur. (Figures taken from Ref. [36].)

dence. Figure 2.1 (left) depicts experimental data. For bilayer densities (non-black colors), the superfluid density smoothly increases from zero, whilst trilayer densities (black) exhibit conventional BKT response. This unconventional behavior occurs for a wide range of bilyaer densities (Fig. 2.1, right) some of which are predicted to form an incommensurate solid phase according to quantum Monte Carlo [37]. What could explain the anomalous behavior?

Since this exotic physics occurs at a density regime close to completion of the second layer, Nyeki *et al.* theoretically speculated that a "non-Abelian supersolid" might be to blame. As a minimal example, consider what happens if the macroscopic coherent state of a superfluid has more structure than just an overall phase

$$|\Psi(\mathbf{r})\rangle \propto \exp\left[\sqrt{N}e^{i\theta(\mathbf{r})}\left(e^{i\phi(\mathbf{r})}\cos\chi(\mathbf{r})B_1^\dagger + e^{-i\phi(\mathbf{r})}\sin\chi(\mathbf{r})B_2^\dagger\right)\right]|\text{vac}\rangle\,, \tag{2.1}$$

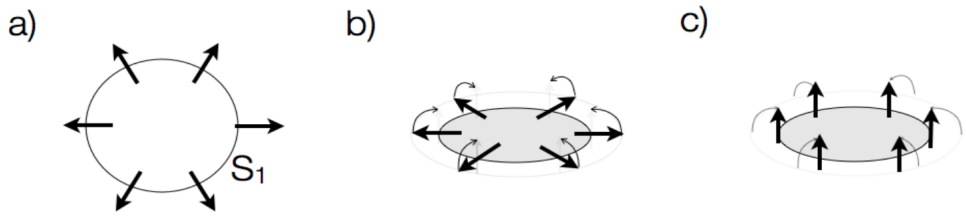

Figure 2.2 (a) A vortex configuration on the U(1) manifold is topologically stable, i.e. it has a well-defined winding number. (b,c) Vortices can smoothly unbind on a S^n manifold when $n > 1$. (Figure taken from Ref. [36].)

where $B^\dagger_{1,2}$ excite single-particle states which have a different density profile. The order parameter for such a macroscopic wavefunction no longer lives on the U(1) manifold, but is instead defined by three angular variables: θ, ϕ, χ which define the surface of a sphere in 4D. This is the S^3 manifold. The symmetry generators of S^3 do not commute, and obey an SU(2) algebra. The enlarged manifold would ensure that vortices are not topologically-stable excitations: $\pi_1(S^3) = 0$. (In other words, a loop in real-space which has a non-zero winding number of the overall phase can smoothly be deformed to a loop with zero winding number, see Fig. 2.2.) This would violate a fundamental assumption of the BKT theory, leading to the absence of a "universal jump" in the superfluid density at the transition. Additionally, the manifold breaks a larger number of symmetry generators, which would result in a larger number of gapless Goldstone modes. These additional modes could deplete the superfluid at a faster rate near $T = 0$.

In this chapter, we will study the novel physics associated with a macroscopic wavefunction of the form (2.1). It is difficult for such a wavefunction to be the ground state of a Hamiltonian with just kinetic energy and interaction terms. Thus we will not comment on features of a non-Abelian supersolid. Rather, we will consider imposing an external potential such that the single-particle states form a band structure. Condensation into the second-lowest band (in the presence of smooth interactions) can lead to a macroscopic wavefunction of the form (2.1). We proceed to describe this setup in detail, and study its novel features.

2.2 The model

Consider the 2D interacting Bose Hamiltonian in the presence of a triangular potential of the form

$$\mathcal{H} = \sum_{\mathbf{k}} (\epsilon_{\mathbf{k}} - \mu)\, b^\dagger_{\mathbf{k}} b_{\mathbf{k}} + \frac{U}{2} \sum_{\mathbf{k},i} \left(b^\dagger_{\mathbf{k}+\mathbf{Q}_i} b_{\mathbf{k}} + h.c. \right) + \frac{1}{2L^2} \sum_{\mathbf{k},\mathbf{k}',\mathbf{q}} V_{\mathbf{q}} b^\dagger_{\mathbf{k}-\mathbf{q}} b^\dagger_{\mathbf{k}'+\mathbf{q}} b_{\mathbf{k}'} b_{\mathbf{k}}, \quad (2.2)$$

where $\epsilon_{\mathbf{k}}$ is the quadratic kinetic energy dispersion, μ is the chemical potential, U is the strength of the external potential, $\mathbf{Q}_i$ are six vectors defined by $\mathbf{Q}_i = Q\left[\cos\left(\frac{\pi i}{3}\right), \sin\left(\frac{\pi i}{3}\right)\right]$, $i \in 0:5$, $V_{\mathbf{q}}$ is the Fourier transform of the interaction potential, L is the system size, and b are the bosonic operators in Fourier space. When $U < 0$ the external potential in real-space exhibits minima on a triangular lattice, and maxima on a hexagonal lattice as depicted in of Fig. 2.3.

We begin by exactly diagonalizing the single-particle Hamiltonian ($V_{\mathbf{q}} = 0$), resulting in a band structure given in the right of Fig. 2.3. Although the global minimum is indeed at the Γ point, the first excited band has a minimum at the M point. If we consider a tight-binding approach on a discrete triangular lattice, then the lowest band represents the non-degenerate s-band while the first two excited bands are formed out of linear combinations of the p_x, p_y orbitals. Indeed previous work studied the metastability of a p-band orbital on a triangular lattice with on-site interactions [38, 39]. We aim to emphasize the novel properties which may arise due to certain finite-range interactions which preserve the single-particle eigenstate degeneracy at the mean-field level. We call this first excited band the p-band.

There is a three-fold degeneracy in the single-particle ground states of the p-band which comes from the three inequivalent M points of the Brillouin zone of a triangular lattice. (See Fig. 2.4.) The creation operator which excites a single-particle eigenstate with a minimum energy at the M point may be written in terms of plane wave state according to: $B^\dagger_{M_1} = \kappa \left(b^\dagger_{\mathbf{Q}_0/2} - b^\dagger_{-\mathbf{Q}_0/2} \right) + \ldots$ where the dots indicate higher-order Fourier modes which get mapped back onto M_1. The κ parameters are complex numbers which represent the relative population and phase between different Fourier components which are determined by diagonalizing the single-particle Hamiltonian.

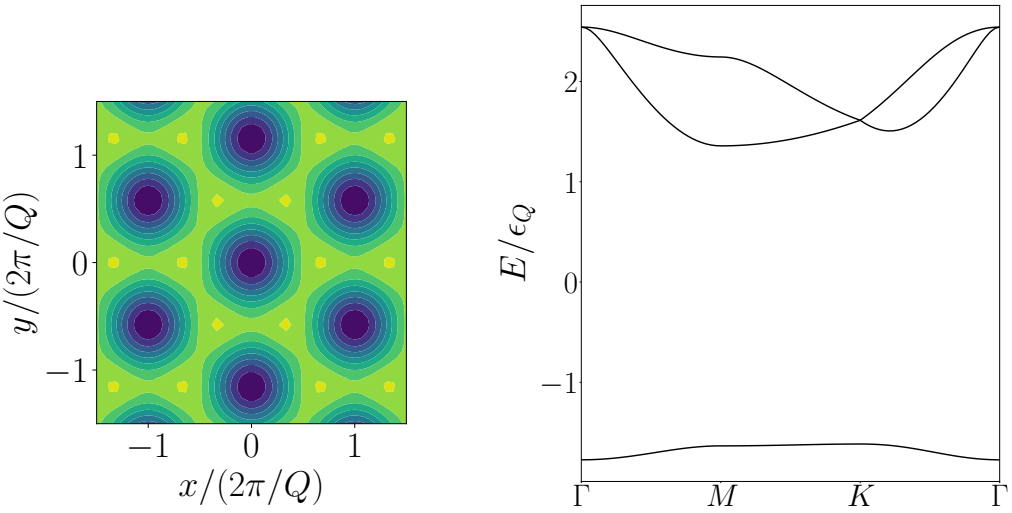

Figure 2.3 *Left*: Contour plot of external potential in real-space with minima (blue) on triangular lattice, maxima (yellow) on hexagonal lattice. *Right*: Single-particle eigenvalues in the Brillouin zone, for parameter value $U = -2\epsilon_Q$.

(κ are also chosen to properly normalize the wavefunction.) However there are two more states which are precisely degenerate: $B^\dagger_{M_2} = \kappa\left(b^\dagger_{\mathbf{Q}_1/2} - b^\dagger_{-\mathbf{Q}_1/2}\right) + \ldots$, $B^\dagger_{M_3} = \kappa\left(b^\dagger_{\mathbf{Q}_2/2} - b^\dagger_{-\mathbf{Q}_2/2}\right) + \ldots$. The M point minimum is therefore triply degenerate at the single-particle level. From now on we write $B_{M_i} = B_i$.

Upon condensing at the M-point, the black spots in Fig. 2.4 depict the possible wavevectors $\mathbf{G}_i$ where bosons may condense in Fourier space, where we truncate to the n Fourier components closest to zero momentum to numerically perform calculations. Each of these n sites will be assigned a complex scalar α_i which represents the condensate amplitude at the wavevector $\mathbf{G}_i$. The relative strength between different α_i parameters is set by finding the single-particle eigenstates. The "natural" Brillouin zone set by the external potential partitions momentum space into Brillouin zones which are separated by an integer multiple of $\mathbf{Q}_i$. Upon condensing at M, the periodicity of the system changes such that the new Brillouin zones are now separated by an integer multiple of $\mathbf{Q}_i/2$, as depicted in Fig. 2.5. (The fundamental Brillouin zone changes after condensation.)

If we now consider the addition of isotropic interactions to the model, we find that as long as the condition $V(k \geq Q/2) = 0$ is satisfied, then the interaction term does

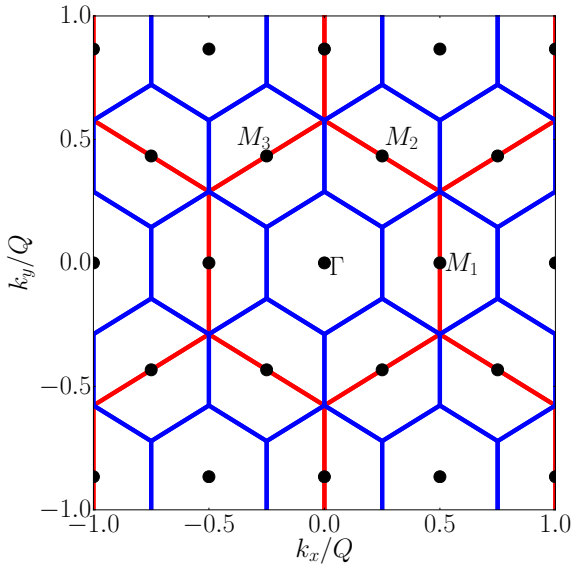

Figure 2.4 The Brillouin zone set by the applied external potential $\mathbf{Q}_i$ depicted in red. The first excited band minimum occurs at the three inequivalent M points. Upon condensation at the M points, the fundamental periodicity of the system doubles in real-space, and hence the Brillouin zone halves in momentum space, as depicted by the blue Brillouin zone above. If $V(k \geq Q/2) = 0$ then the interaction does not directly couple the condensation momenta corresponding to distinct M points. Notation: Each of the n black dots represents a Fourier component where bosons can condense, and has an associated wavevector $\mathbf{G}_i$ and complex number α_i which represents the relative population and phase at the associated Fourier component.

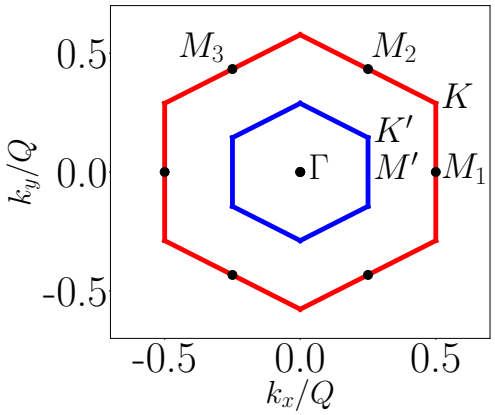

Figure 2.5 The first Brillouin zone before (red) and after (blue) condensation.

Figure 2.6 If $V(k \geq Q/2) = 0$ is satisfied, then direct interaction processes (left) between the different condensation momenta at M_i and M_j are forbidden. "Superexchange" processes (right) can still couple the inequivalent M points via intermediate states.

not couple the condensation spots between inequivalent M points and consequently the three-fold degeneracy is preserved at the mean-field level. (See Fig. 2.6 left.) Mathematically, this implies that the coherent state

$$|\Psi\rangle = e^{-N/2} \exp\left[\sqrt{N}\left(c_1 B_1^\dagger + c_2 B_2^\dagger + c_3 B_3^\dagger\right)\right] |\text{vac}\rangle\,, \tag{2.3}$$

is a mean-field (local) minimum of the energy: $E_{\text{mf}} = \langle\Psi|H|\Psi\rangle$, for any state: $|c_1|^2 + |c_2|^2 + |c_3|^2 = 1$ as long as $V(k \geq Q/2) = 0$ is satisfied. Note that this condition ensures that the average number of particles will be N, which is set by the chemical potential. Our setup therefore requires two non-standard ingredients: (1) condensation into the second-lowest band (the p-band), and (2) an interaction profile which obeys $V(k \geq Q/2) = 0$. In Fig. 2.7, we present plots of the single-particle density for three distinct states in the ground state manifold of the p-band.

If the interaction condition is not satisfied (e.g. for a real-space contact interaction, $V(k) = V_0$) then the interaction term necessarily couples spots between the inequivalent M points, and consequently the relative phases and population distributions become locked to minimize E_{mf}. In general, if $V(k \geq Q/2) > 0$, then the phases orient themselves in such a way as to minimize the squared density of the macroscopic wavefunction. As studied in previous work [38], this constrains the ground state to be of the form: $|\Psi\rangle \propto \exp\left[\sqrt{N}e^{i\theta}\left(B_1^\dagger + iB_2^\dagger\right)\right]|\text{vac}\rangle$, implying that the only continuous symmetry remaining is the overall U(1) global gauge symmetry [38]. We wish to avoid this scenario in order to probe the novel physics associated with a "non-Abelian condensate."

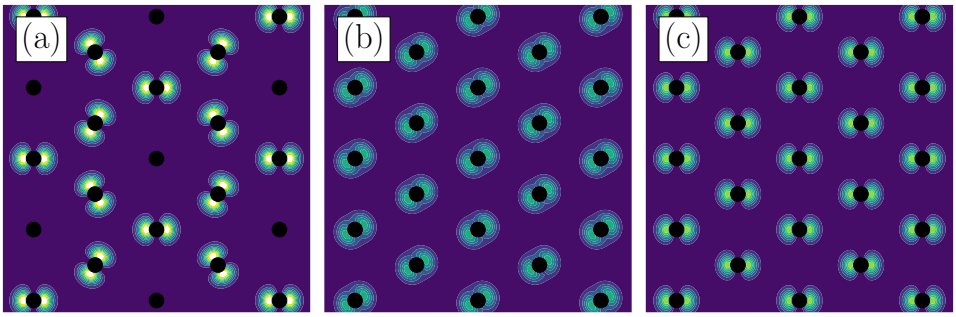

Figure 2.7 Contour plot for the density for three distinct single-particle states which minimize the energy of the p-band: (a) $c_1 = c_2 = c_3$, (b) $c_1 = ic_2, c_3 = 0$, (b) $c_1 = 1, c_2 = c_3 = 0$. The black dots indicate minima of the triangular lattice potential. State (b) has the flattest density profile, thus minimizing the energy of a contact interaction in real-space.

2.3 SU(3) symmetry and the S^5 manifold

In the previous section we found that as long as the condition $V(k \geq Q/2) = 0$ is met, the macroscopic wavefunction associated with the interacting condensate in the p-band is of the form

$$|\Psi\rangle \propto \exp\left[\sqrt{N}\left(c_1 B_1^\dagger + c_2 B_2^\dagger + c_3 B_3^\dagger\right)\right]|\text{vac}\rangle\,, \tag{2.4}$$

where $|c_1|^2 + |c_2|^2 + |c_3|^2 = 1$ and $B_{1,2,3}^\dagger$ represent the three inequivalent ground states at the M points. The order-parameter of a given state in the manifold is

$$\left\langle \Psi \left| \hat{\psi}(\mathbf{r}) \right| \Psi \right\rangle = \sqrt{\bar{n}} \begin{pmatrix} c_1(\mathbf{r}) & c_2(\mathbf{r}) & c_3(\mathbf{r}) \end{pmatrix} \begin{pmatrix} \phi_1(\mathbf{r}) \\ \phi_2(\mathbf{r}) \\ \phi_3(\mathbf{r}) \end{pmatrix} \equiv \sqrt{\bar{n}}\mathbf{c}^T \cdot \mathbf{\Phi} \tag{2.5}$$

where $\bar{n} = N/L^2$ and $\phi_i(\mathbf{r}) = \langle \mathbf{r}|B_i^\dagger|\text{vac}\rangle$ are single-particle wavefunctions. Thus the order-parameter space may be represented as a 3-dimensional complex vector $\mathbf{c}$ with unit norm. The space of degenerate coherent states is isomorphic to the manifold of S^5, i.e. the hypersphere in six dimensions, since the only requirement to remain degenerate is $\sum_{i=1}^{3} (\text{Re}[c_i]^2 + \text{Im}[c_i]^2) = 1$. Formally this is because the Hamiltonian has an emergent SU(3) symmetry which results in a degenerate S^5 manifold, explained below.

2.3.1 Relationship between SU(3) and S^5

Consider the problem of a system consisting of three types of bosons each of which cost an equivalent amount of energy

$$\mathcal{H}_{\mathrm{SU(3)}} = E\left(B_1^\dagger B_1 + B_2^\dagger B_2 + B_3^\dagger B_3\right). \tag{2.6}$$

The symmetry generators of the Hamiltonian are the so-called Schwinger-Bose representation of SU(3): $Q^i = \frac{1}{2}\sum_{jk} B_j^\dagger \Delta^i_{jk} B_k$, where the Δ are Gell-Mann matrices

$$\Delta^1 = \begin{pmatrix} 0 & 1 & 0 \\ 1 & 0 & 0 \\ 0 & 0 & 0 \end{pmatrix}, \quad \Delta^2 = \begin{pmatrix} 0 & -i & 0 \\ i & 0 & 0 \\ 0 & 0 & 0 \end{pmatrix}, \quad \Delta^3 = \begin{pmatrix} 1 & 0 & 0 \\ 0 & -1 & 0 \\ 0 & 0 & 0 \end{pmatrix},$$

$$\Delta^4 = \begin{pmatrix} 0 & 0 & 1 \\ 0 & 0 & 0 \\ 1 & 0 & 0 \end{pmatrix}, \quad \Delta^5 = \begin{pmatrix} 0 & 0 & -i \\ 0 & 0 & 0 \\ i & 0 & 0 \end{pmatrix}, \quad \Delta^6 = \begin{pmatrix} 0 & 0 & 0 \\ 0 & 0 & 1 \\ 0 & 1 & 0 \end{pmatrix},$$

$$\Delta^7 = \begin{pmatrix} 0 & 0 & 0 \\ 0 & 0 & -i \\ 0 & i & 0 \end{pmatrix}, \quad \Delta^8 = \frac{1}{\sqrt{3}} \begin{pmatrix} 1 & 0 & 0 \\ 0 & 1 & 0 \\ 0 & 0 & -2 \end{pmatrix}.$$

The Q^i operators form an SU(3) algebra, and each of them satisfies $[\mathcal{H}_{\mathrm{SU(3)}}, Q^i] = 0$. The manifold of degenerate single-particle ground states is

$$|\mathrm{gnd}\rangle = \left(c_1 B_1^\dagger + c_2 B_2^\dagger + c_3 B_3^\dagger\right)|\mathrm{vac}\rangle, \qquad |c_1|^2 + |c_2|^2 + |c_3|^2 = 1. \tag{2.7}$$

In this simple example, an SU(3) symmetry of the Hamiltonian is responsible for an S^5 manifold of degenerate ground states.

In direct analogy with the single-particle problem, we only need five symmetry generators to parameterize the full S^5 manifold of our interacting macroscopic state. Any state $|\Psi\rangle$ in the degenerate manifold may be achieved by the following unitary transformation on the "highest-weight state":

$$|\Psi\rangle \propto \exp\left[i\sum_{j=4}^{8}\theta_j Q^j\right]\exp\left[\sqrt{N}B_3^\dagger\right]|\mathrm{vac}\rangle. \tag{2.8}$$

Namely the first three generators $Q^{1:3}$ which form an SU(2) subgroup are redundant and hence are not needed in parameterizing the manifold. This is consistent with the isomorphism $S^5 \sim \mathrm{SU}(3)/\mathrm{SU}(2)$, and has implications on the number/type of Goldstone modes in the system: Although SU(3) has 8 symmetry generators, the ground state only spontaneously breaks 5 of them.

The SU(3) symmetry of the interacting Hamiltonian is emergent (or accidental): $[\mathcal{H}, Q^i] \neq 0$, but $\langle\Psi|[\mathcal{H}, Q^i]|\Psi\rangle = 0$. This implies that the S^5 degenerate manifold will be destroyed from corrections beyond mean-field theory. In Sec. 2.7 we will show that this splitting is small for the parameter regime considered.

2.3.2 Goldstone modes for nonrelativistic Hamiltonians: The Watanabe-Brauner counting rule

Goldstone's theorem [18] states that for every symmetry generator which is spontaneously broken, the spectrum is guaranteed a linear (in momentum), gapless excitation mode: $E(k) \propto k$. A crystalline solid is the simplest example: The continuous translational symmetry is broken, which corresponds to a linear, gapless phonon mode in each dimension. While Goldstone's theorem is exact for relativistic Hamiltonians, it requires some modification for effective low-energy Hamiltonians which break Lorentz invariance and possess non-commuting symmetry generators. Surprisingly, this generalization was only uncovered within the last decade.

Watanabe and Brauner spectulated a generalization to Goldstone's theorem [40, 41], which was later rigorously proved by Watanabe and Murayama [42, 43] and generalized to emergent symmetries [44, 45]. The algorithm to predict Goldstone modes for non-Abelian symmetry generators in the absence of Lorentz invariance is as follows: Suppose we have n broken symmetry generators $P_1, \ldots, P_n$. Define a matrix: $\Gamma_{ij} = \langle \mathrm{gnd}\,|[P_i, P_j]|\,\mathrm{gnd}\rangle$, where $|\mathrm{gnd}\rangle$ is the symmetry-broken ground state. The number of modes with even dispersion in momentum k is given by $n_{\mathrm{even}} = \frac{1}{2}\mathrm{rank}(\Gamma)$ and the number of odd modes is $n_{\mathrm{odd}} = n - 2n_{\mathrm{even}}$. Applying this rule to any state in the S^5 manifold, we anticipate two even and one odd mode,

which we shall confirm numerically and analytically in the subsequent sections. Note that quadratic Goldstone modes are only predicted to arise in the presence of non-commuting generators.

We sketch an intuitive understanding of this result, which is explained more carefully in Appendix A. Gapless modes in the momentum k are adiabatically related to zero-energy eigenstates of the Hamiltonian at $H(k = 0)$. These zero-energy eigenstates are found by applying symmetry generators to the spontaneously-broken order parameter: $\mathbf{e}_i = \Delta^i \mathbf{c}$, where $\mathbf{c}$ is the order-parameter vector of the condensed state. Abelian symmetry generators will correspond to orthogonal zero-modes which generate independent gapless excitations. However, two non-Abelian symmetry generators can generate orthogonal zero-modes which correspond to the *same* gapless excitation. The canonical example is the Heisenberg ferromagnet: The ground state breaks an S^2 symmetry, but only has a single, quadratic gapless excitation in k. The two broken symmetry generators conspire to generate the same gapless excitation.

2.3.3 Implications for a BKT transition

Apart from anomalous Goldstone modes, a non-Abelian symmetry manifold is also interesting in the context of superfluid BECs in two dimensions [46]. To understand this, let us first review the conventional theory, which was briefly discussed in the previous chapter.

Conventional superfluids with condensation into one single-particle state have a complex scalar as an order parameter. The global gauge symmetry of this order parameter means that the coherent states span a U(1) manifold (see Sec. 1.3.1). In two dimensions, the Mermin-Wagner-Hohenberg theorem [5, 6] forbids spontaneous breaking of the U(1) symmetry, i.e. no condensate with infinitely long ranged phase coherence, at any non-zero temperatures for a system in the thermodynamic limit. However, the loss of condensation does not necessarily lead to the loss of superfluidity. The destruction of superfluidity in the U(1) superfluid requires freely propagating vortices inducing phase slips across the system. BKT [7, 8] showed

that vortices are bound in vortex-antivortex pairs below a non-zero critical temperature T_{BKT}. The motion of these pairs do not cause phase slips. Thus, the system remains in a superfluid phase up to T_{BKT}. Above this critical temperature, the vortices and antivortex unbind and the system loses its superfluid response due to freely propagating vortices.

The BKT theory relies on the topological protection of the vortices in the form of quantized circulation. Since the BKT superfluid is the only known superfluid without condensation at non-zero temperatures, this leads us to ask whether our non-Abelian condensate possesses topologically protected defects which can protect it from phase slip events. The first homotopy group for our S^5 manifold is trivial: $\pi_1(S^5) = 0$, meaning that any closed loop in the manifold of S^5 may be continuously shrunk to a point. This means that phase vortices are not topologically stable. Explicitly, we can destroy the phase of the amplitude at M_i by a trajectory on the S^5 manifold that takes the coherent state through a region where $c_i = 0$. In addition, $\pi_2(S^5)$ is also trivial and so there are no topologically stable defects for our coherent states in two dimensions.

In the absence of topological defects, we expect that our system is not protected from thermally induced phase slips and so is *not* a superfluid in the thermodynamic limit. Thus, the 2D S^5-degenerate condensate we study here is a rare example of an interacting Bose system without superfluidity in the thermodynamic limit at any non-zero temperature. In this sense, a condensate with non-Abelian symmetry generators may be viewed as a "failed superfluid" in two dimensions, the failure being the lack of topological protection when the order parameter exists on an S^5 manifold.

We should stress that the loss of condensate in two dimensions only applies to the thermodynamic limit. Bose condensation is possible in a finite system whose size is smaller than the correlation length of the order parameter. We will see explicitly how a system loses condensation and superfluidity as we increase the system size or raise the temperature in Sec. 2.6. In order to perform that stability analysis, we

need to understand the low-energy excitations of the system at zero temperature. This is studied in the next section.

2.3.4 Summary

The manifold of degenerate coherent states in the p-band is isomorphic to S^5 in the presence of interactions which obey $V(k > Q/2) = 0$. From this simple observation, we have already deduced two robust statements: (1) we expect two quadratic gapless modes and one linear gapless mode due to the Watanabe-Brauner generalization of Goldstone's theorem, and (2) we do not expect a BKT transition due to the topological instability of vortices in the overall phase of the wavefunction. In the following section, we will use Bogoliubov theory to confirm these predictions.

2.4 Bogoliubov transformation and symmetries

2.4.1 Bogoliubov Hamiltonian

Once the system spontaneously chooses a ground state, we may find the excitation spectrum for a given state by diagonalizing the Bogoliubov Hamiltonian. To construct the Bogoliubov Hamiltonian, we make the replacement $b_{\mathbf{G}_i} \to \alpha_i + \delta b_{\mathbf{G}_i}$ in the microscopic Hamiltonian and only keep terms which are quadratic in α; this makes the Hamiltonian quadratic in the bosonic operators and hence solvable. (See Sec. 1.3.2.) We will divide reciprocal space into n Brillouin zones centered at each of the possible n condensation sites located at reciprocal lattice sites labeled $\mathbf{G}_i$ and focus on momenta near these spots: $b_{\mathbf{G}_i+\mathbf{k}} \equiv b_{i,\mathbf{k}}$ where $\mathbf{k}$ is only defined within the first Brillouin zone (blue hexagon in Fig. 2.5). In the next section we write the explicit form of this Hamiltonian for the p-band condensate.

2.4.2 Bogoliubov transformation

The Bogoliubov Hamiltonian described in the previous subsection is of the form

$$\mathcal{H}^{\text{Bog}} = \frac{1}{2}\sum_{\mathbf{k}} B_{\mathbf{k}}^{\dagger} H_{\mathbf{k}} B_{\mathbf{k}}, \qquad B_{\mathbf{k}} = \left(b_{1,\mathbf{k}}, \ldots, b_{n,\mathbf{k}}, b_{1,-\mathbf{k}}^{\dagger}, \ldots, b_{n,-\mathbf{k}}^{\dagger}\right)^{T}, \tag{2.9}$$

where $H_{\mathbf{k}}$ is a $2n \times 2n$ matrix and n is the number of condensation spots considered. This is just a n-mode generalization of the Hamiltonian considered in Sec. 1.3.2. We define a Bogoliubov transformation

$$B_{\mathbf{k}} = T_{\mathbf{k}} \tilde{B}_{\mathbf{k}}, \qquad B_{\mathbf{k}}^{\dagger} = \tilde{B}_{\mathbf{k}}^{\dagger} T_{\mathbf{k}}^{\dagger}. \tag{2.10}$$

to bosonic quasiparticles β. The diagonalized Hamiltonian reads

$$\mathcal{H}^{\text{Bog}} = \frac{1}{2}\sum_{\mathbf{k}} \tilde{B}_{\mathbf{k}}^{\dagger} \Sigma_z \Lambda_{\mathbf{k}} \tilde{B}_{\mathbf{k}}, \qquad T_{\mathbf{k}}^{\dagger} H_{\mathbf{k}} T_{\mathbf{k}} = \Sigma_z \Lambda_{\mathbf{k}}, \tag{2.11}$$

where $\Sigma_z = \sigma_z \otimes \mathbb{I}_n$ and $\Lambda_{\mathbf{k}}$ is a diagonal matrix with entries $\lambda_{\mathbf{k},\mu}$ found via

$$\Sigma_z H_{\mathbf{k}} t_{\mathbf{k},\mu} = \lambda_{\mathbf{k},\mu} t_{\mathbf{k},\mu}, \tag{2.12}$$

where $t_{\mathbf{k},\mu}$ is a column of $T_{\mathbf{k}}$. The spectral eigenvalues are found by solving for the eigenvalues of $\Sigma_z H_{\mathbf{k}}$, and the transformation matrix columns $t_{\mathbf{k},\mu}$ correspond to the right-eigenvectors. Once this transformation is achieved then the Hamiltonian takes the simple form

$$\mathcal{H}^{\text{Bog}} = \sum_{\mathbf{k}} \sum_{\mu=1}^{n} E_{\mathbf{k}\mu} \left(\beta_{\mathbf{k}\mu}^{\dagger} \beta_{\mathbf{k}\mu} + \frac{1}{2}\right). \tag{2.13}$$

where the factor of $1/2$ represents the zero-point energy associated with the spectrum.

2.4.3 Particle-hole and inversion symmetry

By construction, a bosonic Bogoliubov Hamiltonian has particle-hole symmetry

$$\Sigma_x H_{\mathbf{k}} \Sigma_x = H_{-\mathbf{k}}^{*}, \tag{2.14}$$

where $\Sigma_x = \sigma_x \otimes \mathbb{I}_n$, which implies that the transformation is of the form

$$T_{\mathbf{k}} = \begin{pmatrix} U_{\mathbf{k}} & V_{\mathbf{k}} \\ V_{-\mathbf{k}}^{*} & U_{-\mathbf{k}}^{*} \end{pmatrix}. \tag{2.15}$$

symmetry	Bog. spectrum
particle-hole	$\{\lambda(\mathbf{k})\} = -\{\lambda(-\mathbf{k})\}$
inversion	$\{\lambda(\mathbf{k})\} = \{\lambda(-\mathbf{k})\}$
PH + IS	$\{\lambda(\mathbf{k})\} = -\{\lambda(\mathbf{k})\}$

Table 2.1: Symmetry implications on the Bogoliubov spectrum. PH is particle-hole symmetry; IS is inversion.

Thus if $t_{\mathbf{k},\mu}$ is an eigenvector of $\Sigma_z H_{\mathbf{k}}$ with eigenvalue $\lambda_{\mathbf{k},\mu}$, then $\Sigma_x t^*_{-\mathbf{k},\mu}$ is also an eigenvalue of $\Sigma_z H_{\mathbf{k}}$ with eigenvalue $-\lambda_{\mathbf{k},\mu}$.

The Bogoliubov Hamiltonian in the S^5 manifold also has inversion symmetry (IS), defined by

$$PH_{\mathbf{k}}P = H_{-\mathbf{k}}, \tag{2.16}$$

where $P = \mathbb{I}_2 \otimes \tau$ and τ is a matrix which takes $b_{\mathbf{G}_i,\mathbf{k}} \to b_{-\mathbf{G}_i,-\mathbf{k}}$. This is a unitary symmetry which relates eigenvalues at $+\mathbf{k}$ and $-\mathbf{k}$. We summarize the results of this section in Table 2.1, where the notation $\{\lambda(\mathbf{k})\}$ represents the set of eigenvalues at a given $\mathbf{k}$.

2.5 Numerical spectrum

The Bogoliubov Hamiltonian corresponding to (2.2) takes the explicit form

$$\mathcal{H}^{\text{Bog}} = \frac{1}{2}\sum_{\mathbf{k}} B^\dagger_{\mathbf{k}} H_{\mathbf{k}} B_{\mathbf{k}}, \qquad H_{\mathbf{k}} = \begin{pmatrix} N_{\mathbf{k}} & A_{\mathbf{k}} \\ A^*_{-\mathbf{k}} & N^*_{-\mathbf{k}} \end{pmatrix}, \tag{2.17}$$

where

$$\begin{aligned} A_{\mathbf{k}} &= V(\mathbf{k})\alpha^T\alpha + \left[\sum_i V\left(\frac{\mathbf{Q}_i}{2} + \mathbf{k}\right) S_i^{\text{anom}}\right], \\ N_{\mathbf{k}} &= V(\mathbf{k})\alpha^T\alpha^* + \left(\frac{U}{2}\right) W + \epsilon(\mathbf{k}) + (V_0 n - \mu)\,\mathbb{I} + \left[\sum_i V\left(\frac{\mathbf{Q}_i}{2} + \mathbf{k}\right) S_i^{\text{norm}}\right], \end{aligned}$$

and α is a $1 \times n$ matrix representing the condensation at each of the n sites, W is a sparse matrix with unit entries which label sites which are connected by an external

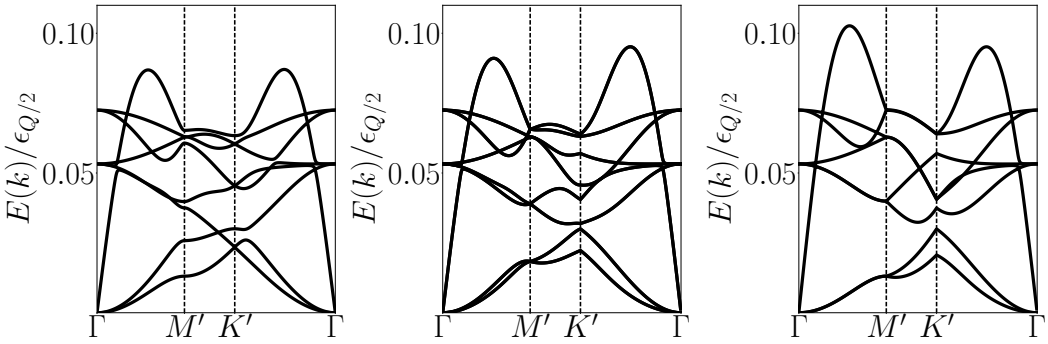

Figure 2.8 Three gapless modes and five gapped modes for: $c_1 = c_2 = c_3$ (left); $c_1 = ic_2, c_3 = 0$ (middle); $c_1 = 1, c_2 = c_3 = 0$ (right). Parameter values: $V(k) = \exp(-k^2/\sigma^2), \sigma = 0.3Q/2$, $U = -6\epsilon_{Q/2}$.

potential wavevector $\mathbf{Q}_i$, $\epsilon(\mathbf{k})$ is a diagonal matrix which accounts for the kinetic energy expanded around the M points, and the term proportional to the identity is due to the self-interaction as well as the chemical potential. The terms in square brackets are only non-zero if the condition $V(k \geq Q/4) \neq 0$ is satisfied, namely there is scattering from one Brillouin zone to the adjacent ones. The S matrices defined above are

$$(S_i^{\text{anom}})_{mn} = \alpha_{\mathbf{G}_m - \mathbf{Q}_i/2}\alpha_{\mathbf{G}_n + \mathbf{Q}_i/2}, \qquad (S_i^{\text{norm}})_{mn} = \alpha^*_{\mathbf{G}_m - \mathbf{Q}_i/2}\alpha_{\mathbf{G}_n - \mathbf{Q}_i/2}, \tag{2.18}$$

where $\mathbf{G}_i$ represents the position in the Brillouin zone of the ith condensation site, and $\alpha_{\mathbf{X}}$ is the condensate amplitude at the momentum $\mathbf{X}$.

In Fig. 2.8 we plot the 8 Bogoliubov modes closest to zero energy for three distinct condensed states. These 8 modes are interacting-versions of the two non-interacting p-bands. (See Fig. 2.5, the Brillouin zone after condensation (blue) is one quarter the size of the Brillouin zone of the non-interacting problem (red).) In agreement with the generalization of Goldstone's theorem, we find that each state admits two quadratic gapless modes, and a single linear mode. These quadratic modes are absent from a conventional superfluid, and will result in unconventional thermodynamic response which we will describe in the following sections. Also, note that the Bogoliubov spectrum depends on which state in the S^5 manifold the system chooses to condense into. Thus the excitation spectrum carries information about the con-

densed state. This can be viewed as a symptom of the emergent SU(3) symmetry: Each spectrum possesses an associated zero-point energy which will serve to split the S^5-degenerate manifold due to contributions beyond mean-field theory. As we will see in Sec. 2.7, this splitting is relatively weak.

In Appendix A, we use singular perturbation theory to calculate analytical expressions for the gapless Bogoliubov modes for different condensed states in the S^5 manifold. Indeed, we find two modes quadratic in k and a single linear mode which is in agreement with our numerical analysis. For condensation into a single mode $c_1 = 1$ (e.g. Fig. 2.8, right), the excitations with quadratic dispersion are of the form: $\beta^\dagger_{\text{quad},\mathbf{k}} = c(\theta)B^\dagger_{M_2,\mathbf{k}} + d(\theta)B^\dagger_{M_3,\mathbf{k}} + O(k)$ where c, d are coefficients that depend on the direction chosen in the Brillouin zone θ, $O(k)$ represents creation operators which are at least linearly dependent on k, and $B_{M_2,\mathbf{k}} = \kappa\left(b_{\mathbf{Q}_1/2+\mathbf{k}} - b_{-\mathbf{Q}_1/2+\mathbf{k}}\right) + \ldots$ represents the single-particle eigenstates displaced by an amount $\mathbf{k}$ in Fourier space. Thus at small $\mathbf{k}$ we find that the quadratic modes represent populating the single-particle modes corresponding to $B^\dagger_{2,3}$. Hence these quadratic gapless excitations may be viewed as "phasons" similar to those in Ref. [47], i.e. density fluctuations which correspond to the density profile of other states in the S^5 manifold.

We note that there are 4 branches of the Bogoliubov spectrum with negative energy eigenvalues, corresponding to the s-band single-particle states which turn into 4 distinct bands in the smaller Brillouin zone. These negative energy branches are indicative that the system has condensed in a metastable state of the first excited band.

2.6 Thermodynamic response

In the previous section, we calculated the Bogoliubov spectrum around a coherent state in the S^5 degenerate manifold. In this section, we use these results to calculate the thermodynamic response of the superfluid at finite temperature. Specifically, we will calculate the temperature dependence of the condensate depletion and the

normal fluid density. Here we report numerical results which can be confirmed via analytics using a long-wavelength effective field theory [46].

2.6.1 Condensate depletion

The density of bosons out of the condensate is given by

$$N_{nc} = \sum_{i,\mathbf{k}\neq 0} \left\langle b^\dagger_{i,\mathbf{k}} b_{i,\mathbf{k}} \right\rangle, \tag{2.19}$$

which we may rewrite in terms of Bogoliubov quasiparticles as

$$\begin{aligned} N_{nc} &= \sum_{i\mu,\mathbf{k}\neq 0} U^*_{\mathbf{k},i\mu} U_{\mathbf{k},i\mu} \left\langle \beta^\dagger_{\mu,\mathbf{k}} \beta_{\mu,\mathbf{k}} \right\rangle + V^*_{\mathbf{k},i\mu} V_{\mathbf{k},i\mu} \left\langle \beta_{\mu,\mathbf{k}} \beta^\dagger_{\mu,\mathbf{k}} \right\rangle & (2.20)\\ &= \sum_{i\mu,\mathbf{k}\neq 0} V^*_{\mathbf{k},i\mu} V_{\mathbf{k},i\mu} + \left(U^*_{\mathbf{k},i\mu} U_{\mathbf{k},i\mu} + V^*_{\mathbf{k},i\mu} V_{\mathbf{k},i\mu} \right) n_{\mathbf{k}\mu} & (2.21)\\ &\equiv \sum_{\mathbf{k}\neq 0} F_{\mathbf{k}} + \sum_{\mathbf{k}\neq 0} G_{\mathbf{k},\mu} n_{\mathbf{k}\mu}, & (2.22) \end{aligned}$$

where $n_{\mathbf{k},\mu} = 1/(e^{\beta E_{\mathbf{q},\mu}} - 1)$ is the Bose factor for the quasiparticle μ at wavevector $\mathbf{k}$. (Recall that all states in the S^5 manifold respect inversion symmetry, implying: $U_{\mathbf{k},i\mu} = U_{-\mathbf{k},-i\mu}, V_{\mathbf{k},i\mu} = V_{-\mathbf{k},-i\mu}, E_{\mathbf{k},\mu} = E_{-\mathbf{k},\mu}$)

At small temperature T this expression is controlled by the three gapless modes of the system where the thermal factor may be approximated as $n_{\mathbf{k}\mu} \approx T/E_{\mathbf{k},\mu}$. The numerical plots in Fig. 2.9 show that as k tends to zero, $G_{\mathbf{k},\mu=0} \sim 1, G_{\mathbf{k},\mu=1} \sim 1, G_{\mathbf{k},\mu=2} \sim k^{-1}, F_{\mathbf{k}} \sim k^{-1}$. After changing the sum to a 2D integral: $\sum_{\mathbf{k}} \to \left(\frac{L}{2\pi}\right)^2 \int k dk d\theta$ and considering $E_{\mathbf{k},\mu=0,1} \sim k^2, E_{\mathbf{k},\mu=2} \sim k$, we find that that the zero-temperature condensate depletion is finite, while the finite-temperature depletion is marginally divergent as a function of system size. The latter behavior is consistent with Mermin-Wagner theory in 2D which precludes the formation of a true symmetry-broken phase (i.e. a condensate) at any finite temperature.

2.6.2 Normal-fluid density

We now proceed to calculate the normal fluid density ρ_n. This density can be calculated via the transverse current-current response function: We imagine placing

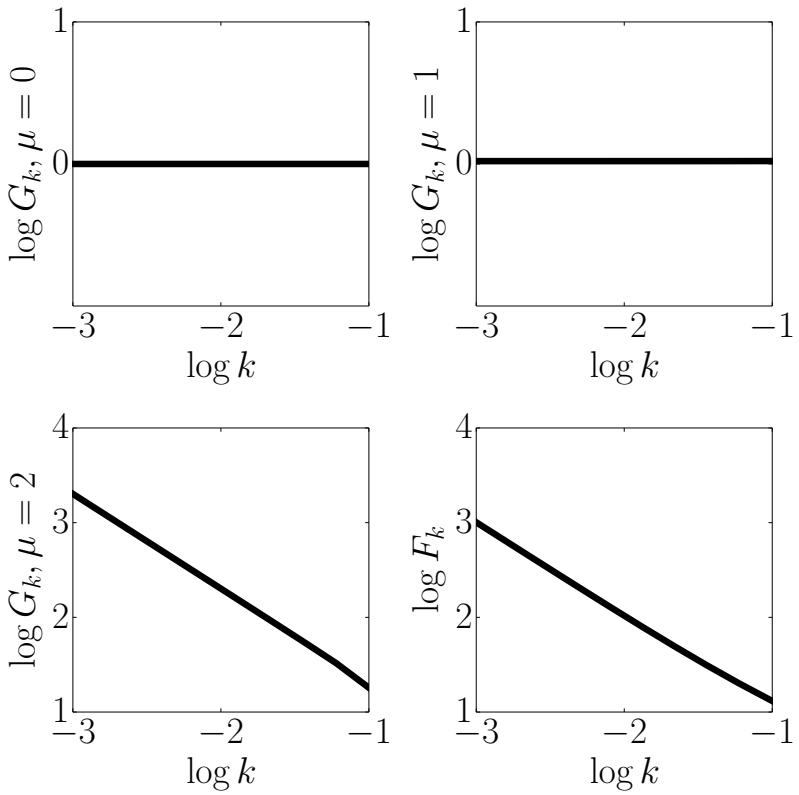

Figure 2.9 Scaling of $G_{\mathbf{k}}$ and $F_{\mathbf{k}}$ with respect to k on a log-log plot, where $\mu = 0, 1$ represent the gapless quadratic modes and $\mu = 2$ is the linear mode. The fitted slope for the bottom figures is -1, indicating the $G_{\mathbf{k},\mu=2} \sim k^{-1}, F_{\mathbf{k}} \sim k^{-1}$ at small k, while $G_{\mathbf{k},\mu=0} \sim 1, G_{\mathbf{k},\mu=1} \sim 1$. Parameter values: $V(k) = \exp(-k^2/\sigma^2), \sigma = 0.3Q/2$, $U = -6\epsilon_{Q/2}$.

a superfluid in a box, applying a small current in one direction, then measuring the current response of the system in an orthogonal direction (i.e. shearing the liquid). We expect the superfluid not to contribute to this transverse response, therefore the resulting shear must be due to the normal fluid fraction alone. The expression for the normal fluid density is

$$\rho_n = \frac{2}{L^d Z} \lim_{\mathbf{q}\to 0} \sum_{mm'} \frac{e^{-\beta \mathcal{E}_m} |\langle m'| J_{\perp \mathbf{q}} |m\rangle|^2}{\mathcal{E}_{m'} - \mathcal{E}_m}\,, \tag{2.23}$$

where m label many-body eigenstates with energies $\mathcal{E}_m$ of the interacting system described by a gas of Bogoliubov excitations with partition function Z [28].

We need the Fourier transform of the current operator $\mathbf{J}_\mathbf{q}$, in particular its component, $J_{\perp\mathbf{q}}$, transverse to the wavevector $\mathbf{q}$

$$J_{\perp\mathbf{q}} = \mathbf{J}_\mathbf{q} \cdot (\hat{\mathbf{z}} \times \hat{\mathbf{q}})\,, \qquad \mathbf{J}_\mathbf{q} = \sum_\mathbf{p} (\mathbf{p} - \tfrac{1}{2}\mathbf{q})\, b^\dagger_{\mathbf{p}-\mathbf{q}} b_\mathbf{p}\,. \tag{2.24}$$

We can write $b_\mathbf{p}$ in terms of the operators near the condensed momenta: $b_{\mathbf{k}i} = \sum_\mu (U_{\mathbf{k},i\mu}\beta_{\mathbf{k}\mu} + V_{\mathbf{k},i\mu}\beta^\dagger_{-\mathbf{k}\mu})$. So, $J_{\perp\mathbf{q}}$ consists of one-quasiparticle and two-quasiparticle contributions. The one-quasiparticle contribution is given by

$$J^{(1)}_{\perp\mathbf{q}} = \sum_\mu (\gamma_{-\mathbf{q}\mu}\beta^\dagger_{-\mathbf{q}\mu} + \gamma^*_{\mathbf{q}\mu}\beta_{\mathbf{q}\mu}) \tag{2.25}$$

$$\gamma_{\mathbf{q}\mu} = \sum_i (\mathbf{G}_i)_{\perp\mathbf{q}} (\alpha_i U^*_{\mathbf{q},i\mu} + \alpha^*_i V_{-\mathbf{q},i\mu}). \tag{2.26}$$

Note that this is zero for the single condensate. For the S^5 symmetric condensate, the matrix element becomes

$$\gamma_{\mathbf{q}\mu} = \sum_{i>0} \alpha_i (\mathbf{G}_i)_{\perp\mathbf{q}} (U^*_{\mathbf{q},i\mu} - U^*_{-\mathbf{q},i\mu} + V_{-\mathbf{q},i\mu} - V_{\mathbf{q},i\mu})\,. \tag{2.27}$$

Noting $(\cdots)_{\perp(-\mathbf{q})} = -(\cdots)_{\perp\mathbf{q}}$ from the definition in (2.24), we see that $\gamma_{-\mathbf{q}\mu} = \gamma_{\mathbf{q}\mu}$.

For the two-quasiparticle contribution

$$\begin{aligned} J^{(2)}_{\perp\mathbf{q}} &= \sum_{\mathbf{k},i\mu\nu} (\mathbf{G}_i + \mathbf{k})_{\perp\mathbf{q}} (U^*_{\mathbf{k}-\mathbf{q},i\mu}\beta^\dagger_{\mathbf{k}-\mathbf{q}\mu} + V^*_{\mathbf{k}-\mathbf{q},i\mu}\beta_{-\mathbf{k}+\mathbf{q}\mu})(U_{\mathbf{k},i\nu}\beta_{\mathbf{k}\nu} + V_{\mathbf{k},i\nu}\beta^\dagger_{-\mathbf{k}\nu}) \\ &= \sum_{\mathbf{k},i\mu\nu} (\mathbf{G}_i + \mathbf{k})_{\perp\mathbf{q}} \Big[U^*_{\mathbf{k}-\mathbf{q},i\mu}U_{\mathbf{k},i\nu}\beta^\dagger_{\mathbf{k}-\mathbf{q}\mu}\beta_{\mathbf{k}\nu} + V^*_{\mathbf{k}-\mathbf{q},i\mu}V_{\mathbf{k},i\nu}\beta_{-\mathbf{k}+\mathbf{q}\mu}\beta^\dagger_{-\mathbf{k}\nu} \\ &\qquad + U^*_{\mathbf{k}-\mathbf{q},i\mu}V_{\mathbf{k},i\nu}\beta^\dagger_{\mathbf{k}-\mathbf{q}\mu}\beta^\dagger_{-\mathbf{k}\nu} + V^*_{\mathbf{k}-\mathbf{q},i\mu}U_{\mathbf{k},i\nu}\beta_{-\mathbf{k}+\mathbf{q}\mu}\beta_{\mathbf{k}\nu} \Big] \\ &= \sum_{\mathbf{k}\mu\nu} \Big[\xi_{\mathbf{k},\mathbf{k}-\mathbf{q},\mu\nu}\beta^\dagger_{\mathbf{k}-\mathbf{q}\mu}\beta_{\mathbf{k}\nu} + \tfrac{1}{2}\eta_{\mathbf{k},\mathbf{k}-\mathbf{q},\mu\nu}\beta^\dagger_{\mathbf{k}-\mathbf{q}\mu}\beta^\dagger_{-\mathbf{k}\nu} + \tfrac{1}{2}\eta^*_{-\mathbf{k},-\mathbf{k}+\mathbf{q},\mu\nu}\beta_{-\mathbf{k}+\mathbf{q}\mu}\beta_{\mathbf{k}\nu} \Big], \end{aligned} \tag{2.28}$$

with the matrix elements

$$\xi_{\mathbf{k},\mathbf{k}-\mathbf{q},\mu\nu} = \sum_i (\mathbf{G}_i + \mathbf{k})_{\perp\mathbf{q}} (U^*_{\mathbf{k}-\mathbf{q},i\mu}U_{\mathbf{k},i\nu} - V_{-\mathbf{k}+\mathbf{q},-i\mu}V^*_{-\mathbf{k},-i\nu}), \tag{2.29}$$

$$\eta_{\mathbf{k},\mathbf{k}-\mathbf{q},\mu\nu} = \sum_i (\mathbf{G}_i + \mathbf{k})_{\perp\mathbf{q}} (U^*_{\mathbf{k}-\mathbf{q},i\mu}V_{\mathbf{k},i\nu} - V_{-\mathbf{k}+\mathbf{q},-i\mu}U^*_{-\mathbf{k},-i\nu}). \tag{2.30}$$

To obtain the last form, we have used the relabeling $\mathbf{k} \to -\mathbf{k}+\mathbf{q}$, $\mathbf{k}-\mathbf{q} \to -\mathbf{k}$, $i \leftrightarrow -i$ and $\mu \leftrightarrow \nu$ to combine the two normal terms and to symmetrize the anomalous terms. As a result, $\eta_{-\mathbf{k}+\mathbf{q},-\mathbf{k},\mu\nu} = \eta_{\mathbf{k},\mathbf{k}-\mathbf{q},\nu\mu}$, and $\xi_{-\mathbf{k}+\mathbf{q},-\mathbf{k},\mu\nu} = -\xi^*_{\mathbf{k},\mathbf{k}-\mathbf{q},\nu\mu}$.

In the limit $\mathbf{q} \to 0$, the matrix elements can be further simplified

$$\xi_{\mathbf{k},\mathbf{k},\mu\nu} = \mathbf{k}_{\perp\mathbf{q}} + \sum_i (\mathbf{G}_i)_{\perp\mathbf{q}} (U^*_{\mathbf{k},i\mu}U_{\mathbf{k},i\nu} - V_{-\mathbf{k},-i\mu}V^*_{-\mathbf{k},-i\nu}), \tag{2.31}$$

$$\eta_{\mathbf{k},\mathbf{k},\mu\nu} = \sum_i (\mathbf{G}_i)_{\perp\mathbf{q}} (U^*_{\mathbf{k},i\mu}V_{\mathbf{k},i\nu} - V_{-\mathbf{k},-i\mu}U^*_{-\mathbf{k},-i\nu}). \tag{2.32}$$

We see that $\xi_{\mathbf{k}\mathbf{k},\mu\nu} = \xi^*_{\mathbf{k}\mathbf{k},\nu\mu}$ in general, i.e. it is a Hermitian matrix in the $\mu\nu$-indices. Note also that $\eta_{\mathbf{k},\mathbf{k},\mu\nu} = \eta_{-\mathbf{k},-\mathbf{k},\nu\mu}$ does not vanish in general and is an antisymmetric matrix in the $\mu\nu$-indices.

Substituting the one-quasiparticle contribution (2.25) for $J_{\perp\mathbf{q}}$ into (2.23), we find

$$\rho^{(1)}_n = \frac{2}{L^d} \lim_{\mathbf{q}\to 0} \left[\frac{|\gamma_{-\mathbf{q}\mu}|^2}{E_{-\mathbf{q}\mu}} (n_{-\mathbf{q}\mu} + 1) - \frac{|\gamma_{\mathbf{q}\mu}|^2}{E_{\mathbf{q}\mu}} n_{-\mathbf{q}\mu} \right], \tag{2.33}$$

where $n_{\mathbf{q}\mu} = 1/(e^{\beta E_{\mathbf{q}\mu}} - 1)$ is the Bose factor for the quasiparticle μ at wavevector $\mathbf{q}$. This reduces to

$$\rho^{(1)}_n = \frac{2}{L^d} \lim_{\mathbf{q}\to 0} \frac{|\gamma_{\mathbf{q}\mu}|^2}{E_{\mathbf{q}\mu}} \tag{2.34}$$

which is a temperature-independent contribution to the normal density.

A similar expression may be derived for the two-quasiparticle terms. The zero-temperature contribution is

$$\rho_n(T=0) = \rho_n^{(1)} + \frac{1}{L^d}\sum_{\mathbf{k}\mu\nu}\frac{|\eta_{\mathbf{k},\mathbf{k},\mu\nu}|^2}{E_{\mathbf{k}\mu}+E_{\mathbf{k}\nu}}\,. \tag{2.35}$$

As we raise the temperature, the T-dependence of this quantity at low T is controlled by the gapless modes of the system. At any non-zero T, the integral is dominated by modes with energies below T where the Bose factor $n_{\mathbf{k}\mu} \simeq T/E_{\mathbf{k}\mu} \gg 1$, i.e. the equipartition limit, leading to the expression

$$\rho_n(T) - \rho_n(0) \simeq \frac{T}{L^d}\sum_{\mathbf{k}\mu\nu}^{E_{\mathbf{k}}<T}\frac{|\xi_{\mathbf{k},\mathbf{k},\mu\nu}|^2 + |\eta_{\mathbf{k},\mathbf{k},\mu\nu}|^2}{E_{\mathbf{k}\mu}E_{\mathbf{k}\nu}} \tag{2.36}$$

where we keep only the gapless modes in μ and ν.

The two-quasiparticle terms control the temperature-dependence of the normal fluid density. In Figs. 2.10 and 2.11, we plot how the ξ and η terms scale as a function of k for the various matrix elements. The relevant contribution comes from the term $\xi^2_{\mathbf{k},00} \sim k^2$, which suggests that

$$\rho_n(T) - \rho_n(0) \sim T\int_{L^{-1}}^{A(T)}\frac{k^2}{k^4}kdk \sim T\log(L\cdot A(T)), \tag{2.37}$$

where A is a wavevector which scales linearly with temperature T. Hence we find that the temperature dependence of the superfluid response is marginally divergent with respect to system size. This is different from a standard 2D superfluid, which has a normal fluid density vanishing as T^3 near $T=0$. The marginally divergent normal fluid density is a symptom of the topological instability of vortex configurations on the S^5 manifold, which preclude the formation of a superfluid in the thermodynamic limit, at any finite temperature.

2.7 Order-by-disorder

The S^5 degeneracy of the p-band ground state manifold only exists at the mean-field level, meaning that the SU(3) symmetry generators only commute with the

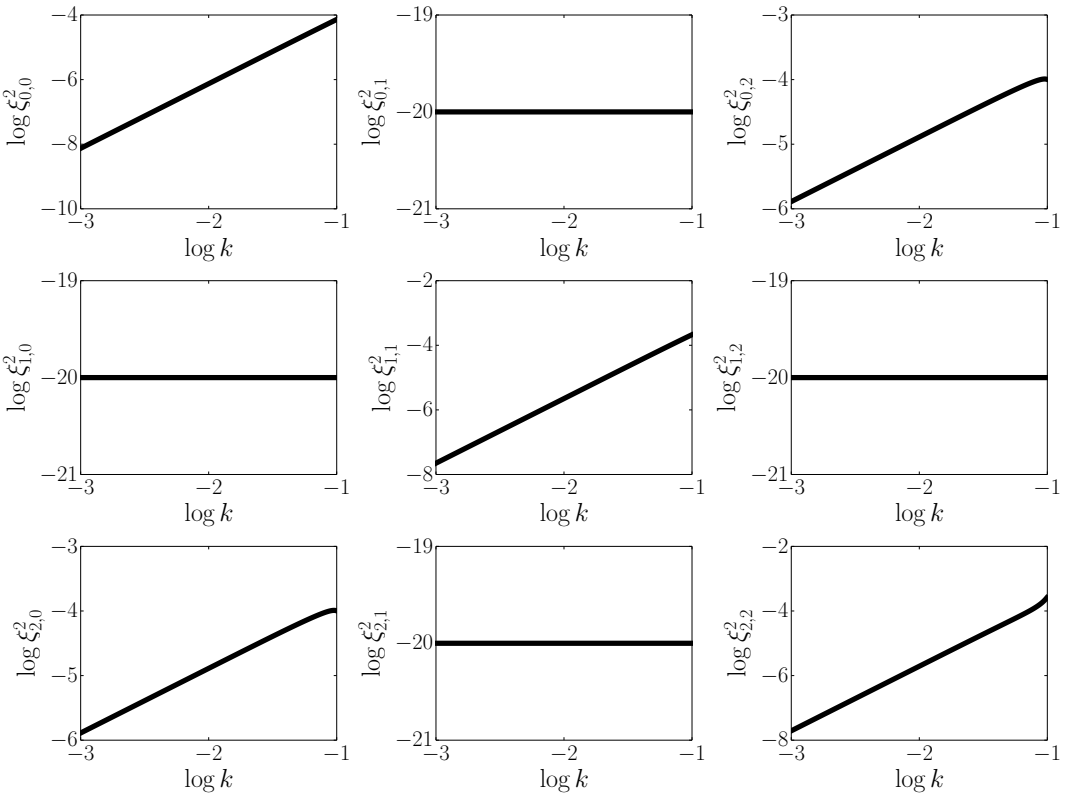

Figure 2.10 Scaling of $|\xi|^2$ as a function of k on a log-log plot near the Γ point, where $\mu = 0, 1$ label the two quadratic branches and $\mu = 2$ labels the linear mode. Note the scale, as some matrix elements are zero due to symmetry. Parameter values: $V(k) = \exp(-k^2/\sigma^2), \sigma = 0.3Q/2$, $U = -6\epsilon_{Q/2}$.

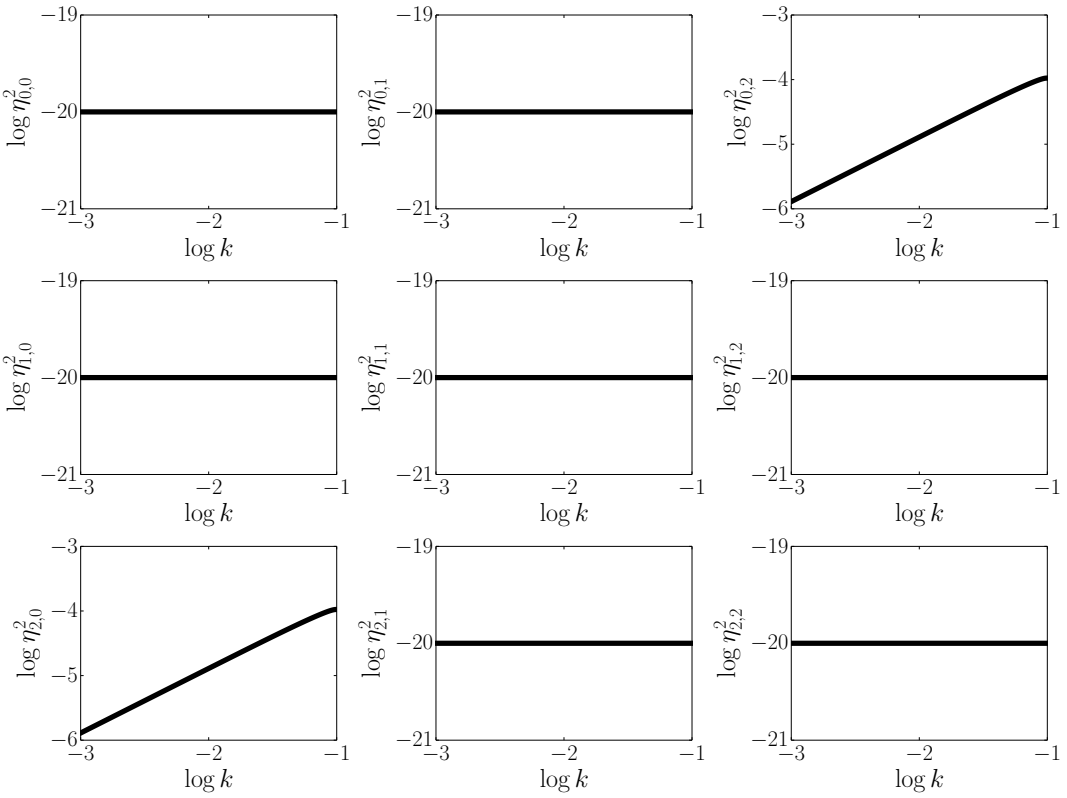

Figure 2.11 Scaling of $|\eta|^2$ as a function of k on a log-log plot near the Γ point, where $\mu = 0, 1$ label the two quadratic branches and $\mu = 2$ labels the linear mode. Note the scale, as some matrix elements are zero due to symmetry. Parameter values: $V(k) = \exp(-k^2/\sigma^2), \sigma = 0.3Q/2$, $U = -6\epsilon_{Q/2}$.

interacting Hamiltonian in the manifold of coherent states: $\langle\Psi|[H, Q^i]|\Psi\rangle = 0$. (See Sec. 2.3.1.) We expect that fluctuations beyond mean-field theory will break this degeneracy. One mechanism which will reduce the emergent symmetry is "order-by-disorder," which shrinks the manifold of degenerate ground states by picking the state which minimizes the zero-point energy associated with its spectrum. Here we show that the zero-point energy difference between different points on the S^5 manifold is very small with respect to other energy scales in the system. Hence we anticipate the effects due to the non-Abelian symmetry generators to be robust in certain parameter regimes.

The expression for the zero-point energy per particle reads

$$\frac{E_{zp}}{N} = \frac{1}{2N}\sum_{\mathbf{k}\in BZ} E(\mathbf{k}) = \frac{1}{2\bar{n}}\left(\frac{1}{2\pi}\right)^2 \int E(\mathbf{k}) d^2\mathbf{k}. \tag{2.38}$$

If we write the zero-point energy in units of the Brillouin zone area over the density of particles: $E_{zp}/N = \epsilon_{zp}(a_{BZ}/\bar{n})$, then we can compare the zero-point energy between different condensed states via numerical integration. This is given in Fig. 2.12. We find that as the range of the interaction in momentum space increases, the evenly condensed state begins to have a lower zero-point energy compared to a single-condensed state. In systems where order-by-disorder is typically important [48], the energy splitting per particle is of order the fundamental energy scale in the system (e.g. $\epsilon_{Q/2}$); however, we find that this contribution is roughly three orders of magnitude suppressed in the S^5 condensate. This suggests that signatures of the SU(3) symmetry generators ought to be observable at small (but finite) temperatures.

2.8 Dipolar-interacting condensates

The interaction condition $V(k > Q/2) = 0$ which is necessary to observe the S^5 manifold can be approximately achieved by using dipolar-interacting bosons. We review the work of Fischer [49] which demonstrates how a finite-range interaction can be realized for dipolar bosons confined to a cloud in the xy-plane. A tunable dipolar-interacting condensate has recently been achieved in Erbium condensates

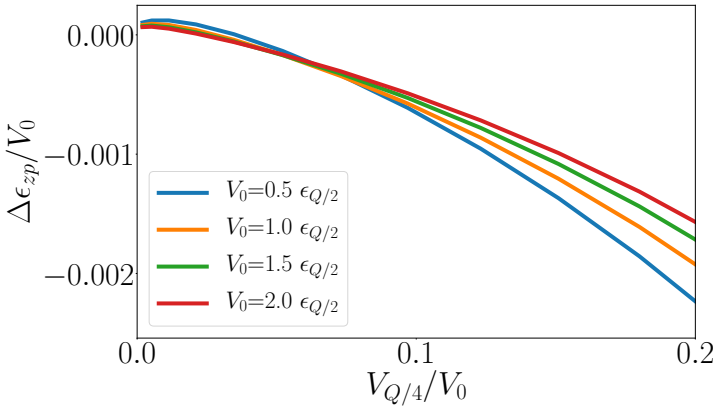

Figure 2.12 Zero-point energy difference between the evenly condensed state $c_1 = c_2 = c_3$ and the single condensed state $c_1 = 1$ as a function of the ratio $V_{Q/4}/V_0$, and for different V_0 values.

[50].

Consider dipolar bosons of mass m with dipole moment d_e, polarized by a strong electric field in the z-direction. The interaction between two bosons at a (three-dimensional) displacement of $\mathbf{r}$ consists of two components. Firstly, there is a contact interaction parametrized by an s-wave scattering length a_s or an interaction strength $g_{3D} = 4\pi\hbar^2 a_s/m$. There is also a dipole-dipole interaction of the form $V_{dd}(\mathbf{r}) = (3g_d/4\pi r^3)(1 - 3z^2/r^2)$ with $g_d = d_e^2/3\epsilon_0$. This is repulsive when $x^2 + y^2 \gg z^2$ and attractive when $x^2 + y^2 \ll z^2$ (when the dipoles are nearly collinear in the z-direction).

When these bosons are confined by harmonic trap to a Gaussian wavepacket of width d_z in the z-direction, the Fourier transform of the effective interaction in the 2D plane can be written as

$$V_{\mathbf{q}} = \frac{g_d}{d_z}\left[\frac{1 + g_{3D}/2g_d}{\sqrt{\pi/2}} - \frac{3}{2}qd_z w\left(\frac{qd_z}{\sqrt{2}}\right)\right] \quad \text{with} \quad w(x) = e^{x^2}\mathrm{erfc}(x)\,, \tag{2.39}$$

where $\mathbf{q}$ is the 2D wavevector of the Fourier transform. Fischer [49] proposed that the contact interaction strength g_{3D} can be tuned to be equal to g_d so that $V_{\mathbf{q}} \to 0$ as $q \to \infty$. Thus, the short-range contributions from the dipolar interaction and contact interaction cancel each other, producing an interaction with lengthscale d_z.

For this study, we want this lengthscale to be large compared to the wavelength $\sim 1/Q$ of the density modulations of our coherent state (2.3). This corresponds to the condition that confinement in the z-direction must be larger than $\sqrt{3}a$ where a is the length of the triangular lattice vector. This suppresses intervalley processes that break the S^5 symmetry.

In summary, we impose two conditions on the interaction to observe the S^5 symmetry

$$g_d = g_{3\mathrm{D}}\,, \qquad d_z > \sqrt{3}a\,, \tag{2.40}$$

which can be achieved by using a Feshbach resonance and by adjusting the out-of-plane confinement of the trap.

2.9 Summary and outlook

Motivated by recent solid-state experiments, we have studied a non-Abelian condensate with spatial density modulations in two dimensions. We have described a setup where such a coherent state is a local minimum of the energy at zero temperature, and argued that the enlarged degeneracy manifold leads to the loss of topological vortices which suggests that we do not expect superfluidity in the system at non-zero temperatures. This is verified by a calculation of how condensation and superfluidity is lost as the system size is increased at non-zero temperatures. We suggest that dipolar-interacting condensates can be used to unambigiously observe this exotic superfluidity. Our scenario is not confined to a triangular lattice and is anticipated to generalize to degenerate higher band condensates in e.g. square, hexagonal lattices and in three dimensions. Intriguingly, our non-Abelian superfluid shares similar low-temperature behavior and a lack of a BKT transition with the ^{4}He bilayer on graphite [36]. Nevertheless, a complete theory for this helium system that motivated our story remains elusive.

Chapter 3

Disordered topological superconductors

A common piece of wisdom for symmetry-protected topological insulators and superconductors is that gapless edge modes are robust with respect to disordered terms in the Hamiltonian which keep the model within the same Altland-Zirnbauer symmetry class. While this is true for "weak" disorder realizations which preserve the bandgap, this is no longer the case once the disorder profile is strong enough to close an energy gap in the spectrum. In this chapter, we study a concrete model where strong (symmetry-preserving) disorder is capable of both creating and destroying a topological degeneracy of the ground state. Specifically, we consider a long-range Kitaev chain and uncover a phase diagram as a function of disorder in the onsite potential. As the variance of the potential is increased, regions with 2 Majorana zero modes (MZMs) per edge will first lose one of the modes, then lose both, as a function of increasing disorder. Conversely, certain regions of the phase diagram with 1 MZM can gain a MZM as disorder is increased. Thus we demonstrate that strong disorder (which respects the underlying symmetries of the clean Hamiltonian) can both induce and destroy topological edge modes. Our work additionally provides a minimal starting point to consider the stability of local zero-modes in the presence of a disordered bulk—a setup which has recently received significant

theoretical attention due to the long coherence times of topological edge modes in a many-body localized phase.

3.1 Kitaev's spinless superconductor and the topological qubit

We begin by discussing the simplest example of a topological superconductor (the Kitaev chain), emphasizing its relevance to "topological quantum computation." A fundamental challenge in the pursuit of quantum computing is the design and control of quantum bits (qubits). Quantum systems are experimentally difficult to manipulate due to inevitable interactions with environmental processes which tend to "decohere" a state, i.e. the environment contributes noise to the systems causing a prepared eigenstate to mix with other eigenstates over time. The ground state degeneracy of a topological superconductor may provide a solution to this issue.

About two decades ago, Alexei Kitaev proposed and studied the simplest example of a 1D spinless fermionic superconductor which has a two-fold ground-state degeneracy guaranteed by topological arguments [19]. The ground state is characterized either by a complete lack of quasiparticles, or the presence of a single *non-local* zero-energy excitation composed of a pair of Majorana fermions, one localized on each side of the chain. The two quantum ground states can represent a robust qubit. Local noise cannot couple one ground state to its degenerate partner; these states also do not couple to bulk modes since they are gapped in energy. The exact degeneracy between the ground states also offers protection against "dephasing noise" which can arise if a perturbation induces an unwanted energy splitting between the two states. Thus the degenerate ground state subspace can represent a qubit immune to a number of decoherence processes: Flipping the qubit amounts to moving the state from one of the degenerate ground states to the other. This is the paradigm of topological quantum computing and much experimental effort has been dedicated towards its realization, both academically and commercially. On a more fundamental level,

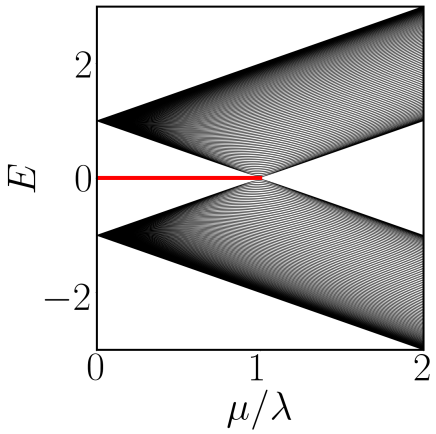

Figure 3.1 Spectrum of the Kitaev chain Hamiltonian (3.1) for $N = 100$ sites. The edge modes have zero energy and are given in red; bulk modes in black.

this system is a simple candidate to unambiguously observe Majorana quasiparticle excitations. In this section we briefly review the simplest model which realizes these ideas, known as the Kitaev chain. Our novel work comes later, in an extension of this paradigmatic model. (See Sec. 3.4.)

Consider the fermionic Bogoliubov-de Gennes (BdG) Hamiltonian:

$$\mathcal{H} = 2\mu \sum_{i=1}^{N} a_i^\dagger a_i - \sum_{i=1}^{N-1} \left(t a_i^\dagger a_{i+1} + \Delta a_i^\dagger a_{i+1}^\dagger + h.c. \right) \tag{3.1}$$

where a_i represents a spinless fermion annihilation operator on lattice site i of a chain with N sites. Fermions experience a chemical potential of strength μ, nearest-neighbor hopping t, and pairing Δ. Conceptually, this model is the simplest example of a topological superconductor. For the remainder of this chapter, we set $t = \Delta \equiv \lambda \in \mathbb{R}$ (although qualitative results remain unchanged away from this limit).

The spectrum of the (fermionic) BdG Hamiltonian is found by diagonalizing (3.1) via a unitary Bogoliubov transformation. In Fig. 3.1 we plot the spectrum of the Hamiltonian as a function of μ/λ. The spectrum is gapped away from the point $\lambda = \mu$. Notably, there exists a single zero-energy excitation whenever $\lambda > \mu$. If we observe the eigenvector associated with the zero-energy excitation, we find that it has support on both edges of the chain, but not within the bulk. This is another example of a topologically protected gapless edge mode (meaning that it cannot be removed without closing a bulk band energy gap), and is best understood by

transforming to a Majorana basis.

Consider the transformation:

$$\alpha_{2i-1} = a_i^\dagger + a_i, \qquad \alpha_{2i} = -i(a_i^\dagger - a_i) \tag{3.2}$$

which turns the "complex" fermions $a_i, a_i^\dagger$ into a pair of "Majorana" modes $\alpha_{2i-1}, \alpha_{2i}$. Majorana fermions are characterized by two properties: (1) they are self-adjoint, i.e. $\alpha^\dagger = \alpha$, and (2) they obey fermionic statistics: $\{\alpha_i, \alpha_j\} = 2\delta_{i,j}$. It is always possible to define a transformation from complex fermions to Majorana fermions. In the Majorana basis, the Hamiltonian (3.1) takes the simple form

$$\mathcal{H} = i\left[\frac{\mu}{2}\sum_{i=1}^{N}(\alpha_{2i}\alpha_{2i-1} + h.c.) - \frac{\lambda}{2}\sum_{i=1}^{N-1}(\alpha_{2i}\alpha_{2(i+1)-1} + h.c.)\right]. \tag{3.3}$$

This Hamiltonian is a nearest-neighbor tight-binding model on a bipartite lattice with intracell hopping magnitude $\mu/2$ and intercell hopping $-\lambda/2$. Notice that this Hamiltonian is exactly the Su-Schrieffer-Heeger model [29] (see Sec. 1.4.3) with distinct sublattice sites corresponding to even/odd labeled Majorana modes. Its topological properties are guaranteed by the chiral symmetry of the Majorana Hamiltonian matrix: $H_{\text{maj}} = -\tau_z H_{\text{maj}} \tau_z$ where $\tau_z = \mathbb{I}_N \otimes \sigma_z$ and the 2×2 subspace labels the two Majorana modes corresponding to each physical site. This symmetry pins Majorana modes at the edge of the sample to have exactly zero energy, and ensures that the winding number of the Bloch Hamiltonian is well defined. It is useful to think about the "fully-dimerized limit" at $\mu = 0$. In this limit, we find that two Majorana operators do not appear in the Hamiltonian: α_1 and α_{2N}, which implies that they are exact zero-energy eigenstates of $\mathcal{H}$.

Even though there are two localized Majorana eigenstates of $\mathcal{H}$ with zero energy in the topological phase, there is only one zero-energy excitation which is *nonlocal*. An implicit assumption of the Bogoliubov transformation is that quasiparticles must be represented as complex fermions, i.e. a Bogoliubov quasiparticle cannot be self-adjoint. Thus, while we have seen that the operators α_1 and α_{2N} are zero-energy eigenstates of the Hamiltonian in the fully dimerized limit, only their linear superposition $b^\dagger = \alpha_1 + i\alpha_{2N}$ forms a valid quasiparticle. This is the origin of the

non-locality of the edge mode: Majoranas on opposite ends of the chain must couple in order to form a proper zero-energy excitation. Note that this is always possible, since the number of particles in the Majorana basis is always even since a single complex fermion splits into two Majoranas. In other words, there is no possibility for a single Majorana zero-mode to exist on one edge without a partner on the other side of the chain.

In this section we have studied the basic model of a topological superconductor with boundary modes composed of Majorana fermions, and emphasized its importance in the context of quantum computing. In summary, the Kitaev chain hosts zero-energy excitations which are inherently non-local, and the existence of these modes are guaranteed via topological arguments as long as a bulk gap exists. As such, the ground state degeneracy of a topological superconductor is a good candidate for a qubit which is immune to a variety of perturbations. In the later sections of this chapter, we will develop this story by suggesting that *local* zero-modes in the presence of a disordered bulk may represent an equally promising paradigm in the quest for the topological qubit.

3.2 Adding disorder to a Kitaev chain

In the forthcoming analysis, we shall examine the robustness of edge modes in the presence of disorder for a variant of the Kitaev chain which hosts *local* edge excitations. As such, it is useful to begin by studying the disordered phase diagram of the Kitaev chain introduced in the previous section.

Consider promoting the chemical potential to a site-dependent quantity according to: $\mu_i = \bar{\mu} + X$ where X is a uniform random variable chosen between $-\sigma$ and $+\sigma$. A simple way to determine the presence of zero-energy edge modes is to guess an ansatz zero-energy mode wavefunction and check whether it is normalizable or not. In the trivial phase, it should be non-normalizable, whilst in the topological phase it should form a valid solution.

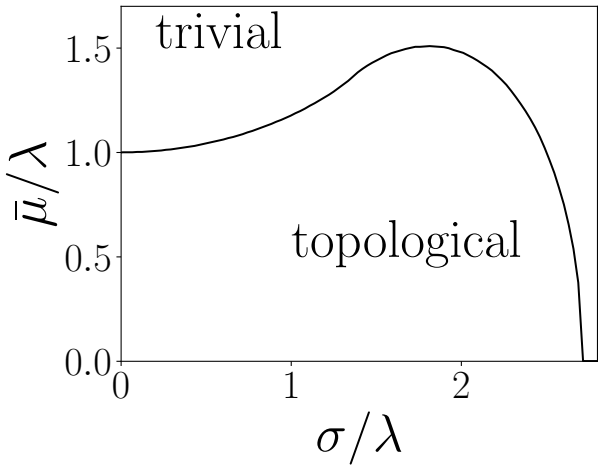

Figure 3.2 Topological phase diagram of a Kitaev chain in the presence of a disordered chemical potential $\mu_i = \bar{\mu} + X$ where X is a uniform random variable between $\pm\sigma$.

More quantitatively, consider the ansatz in a Majorana basis for a mode on the left edge: $e_0 = \sum_{i=1}^{N} A_i \alpha_{2i-1} \equiv \mathbf{A} \cdot \alpha^T$. Note that we only consider Majoranas on the odd sublattice sites in order for the mode to respect chiral symmetry, i.e. $\mathbf{A} = \mathbf{A}\tau_z$, such that its energy is precisely zero. Imposing $\mathcal{H}e_0 = 0$ in a semi-infinite geometry, we arrive at the recursion relation

$$\left|\frac{A_n}{A_1}\right| = \prod_{i=1}^{n} \left|\frac{\mu_i}{\lambda}\right| = \exp\left[\sum_{i=1}^{n} \log\left(\left|\frac{\mu_i}{\lambda}\right|\right)\right] \approx \exp\left[n\left\langle \log\left|\frac{\mu_i}{\lambda}\right|\right\rangle\right] \tag{3.4}$$

where we assume the law of large numbers in the final equality. Thus in order for the right-hand-side converge to zero as $n \to \infty$ we simply need to examine the sign of the expectation value $\langle \log|\mu_i/\lambda| \rangle$ for a single random variable μ_i. The sign of this quantity will inform us whether the system is in a topological or trivial phase.

The topological phase diagram is given in Fig. 3.2. At weak disorder values the phase diagram is generally unaltered from the clean limit. In the presence of moderate disorder, something interesting happens: The addition of disorder can induce a topological state from a trivial state. This is perhaps not too surprising, since disorder has the effect of localizing eigenmodes in 1D [51] which might benefit the formation of edge modes. This disorder-induced topological phase is known as the "topological Anderson insulator" and has been the subject of much interest [52–

55]. We shall discover a generalization of this behavior in the subsequent sections. Finally, we notice that there is a critical amount of disorder above which we no longer expect to observe any topological state. This is because the system can remove a zero-energy edge mode as a function of disorder strength when the "bulk gap" closes at strong disorder.

While including disordered terms is of central importance in modeling conventional solid-state systems [56–58], it is worth noting that recent experiments have devised "controllable disorder" in the realm of ultracold atoms which allows for precise trajectories in parameter space. Indeed, the topological Anderson insulator was recently discovered in a disordered ultracold atomic wire [55]. This opens up the possibility to probe the effects of disorder in a controlled experimental setting.

Having introduced some basic properties of disorder on a Kitaev chain, in the next section we will motivate the study of *local* zero-modes in the presence of a disordered bulk before turning to our novel study.

3.3 Coherent local qubits due to localization

While a number of experimental groups claim to have found the Majorana zero-mode in the form of a "zero-bias peak" in conductivity [56, 57], it remains hotly contested whether the origin is truly topological and hence the stability of these modes is in question. One of the difficulties in validating the presence of topological Majorana modes is precisely in the inherent nonlocality of the excitation. Nonlocal measurements/operations pose a difficult experimental challenge, hence the quest for a robust *local* qubit is equally desirable [59, 60].

Recent studies have found that the coherence times of topological qubits can benefit from an additional ingredient: many-body localization. Many-body localization is the interacting analog of Anderson localization [61], both of which are characterized by a lack of thermalization due to the presence of disorder. In other words, the system has memory of its original state up to arbitrarily long evolution times and the

principle of ergodicity is violated. Notably, Ref. [62] discovered that the interplay of topological order with many-body localization can be beneficial to the coherence times of *local* edge correlators. They study a "cluster-spin Ising model" which maps via Jordan-Wigner transformation to an interacting fermion problem in general, and is a topological spin chain with a $\mathbb{Z}_2 \otimes \mathbb{Z}_2$ degeneracy for certain parameter regimes which physically represents a local spin flip operation at each end of the chain that leaves the spectrum invariant. Interestingly, the $\mathbb{Z}_2 \otimes \mathbb{Z}_2$ degeneracy persists in the interacting, disordered limit (where the system is also in a many-body localized phase). This is evidenced by a robust 4-fold degeneracy in the interacting spectrum, calculated via exact diagonalization. This topological, many-body localized state hosts long coherence times for edge mode correlators which scale with system size [62, 63], and hence potentially provides a route to achieve both stable qubits with better experimental controllability.

In this chapter, we investigate the disordered phase diagram of the noninteracting limit of this model (after Jordan-Wigner transformation into fermionic degrees of freedom). We proceed to define the setup below.

3.4 Local zero-modes in the presence of disorder

We study the effects of disorder on the topological phase diagram for a minimal variant of the Kitaev chain which enables both local and nonlocal zero-energy excitations [64, 65], implying local ground state degeneracies which can represent a *local* qubit. This will also allow us to observe a generalized topological Anderson insulator transition for a $\mathbb{Z}$-classified model.

3.4.1 The model

Consider the Hamiltonian

$$\mathcal{H} = 2\sum_{i=1}^{N} \mu_i a_i^\dagger a_i - \lambda_1 \sum_{i=1}^{N-1} \left(a_i^\dagger a_{i+1} + a_i^\dagger a_{i+1}^\dagger + h.c. \right) - \lambda_2 \sum_{i=2}^{N-1} \left(a_{i-1}^\dagger a_{i+1} + a_{i-1}^\dagger a_{i+1}^\dagger + h.c. \right), \tag{3.5}$$

where λ_1, λ_2 represent nearest and next-nearest neighbor hopping and pairing. (Qualitative results remain unchanged away from the limit where hopping is equal to pairing strength, as long as time-reversal symmetry is respected, i.e. both quantities are real). $\lambda_1, \lambda_2, \mu_i \in \mathbb{R}$, and $\mu_i = \mu$ in the clean case. The disorder is later introduced in the on-site energy $\mu_i = \bar{\mu} + X$ where X is, once again, a uniform random variable chosen between $-\sigma$ and $+\sigma$.

Within the Tenfold way [17], this model (without disorder) can topologically protect any integer number of zero-energy edge modes due to the preserved chiral symmetry. As such, the model is said to have a $\mathbb{Z}$ topological classification. By adding next-nearest-neighbor terms to our model we will be able to achieve phases where two Majorana zero-modes exist on each side of the chain. If we label the ones on the left side of the chain as $\alpha_{l,1/2}$ then we will be able to make a zero-energy Bogoliubov quasiparticle which is fully localized on the left side of the chain via $b_l^\dagger = \alpha_{l,1} + i\alpha_{l,2}$. In this way, we will be able to probe the stability of *local* zero-energy excitations against the presence of disorder.

3.4.2 The clean case

We begin our discussion by reviewing the clean phase diagram of the model using transfer matrices. As before, we define Majorana modes: $\alpha_{2i} = a_i^\dagger + a_i, \alpha_{2i+1} = -i(a_i^\dagger - a_i)$. The Hamiltonian (3.5) transforms to a next-nearest-neighbor Su-Schrieffer-Heeger model [29] where the sublattice label corresponds to the two Majorana states in the original problem.

To check for the presence of Majorana zero-modes (MZMs) with support on "odd" sublattice sites on the left edge, we use the eigenvector ansatz $e_0 = \sum_{i=1}^{N} A_i \alpha_{2i-1}$. Imposing $\mathcal{H} e_0 = 0$ in a semi-infinite geometry, we arrive at the recursion relation

$$\begin{pmatrix} 0 & 1 \\ \frac{\mu}{\lambda_2} & -\frac{\lambda_1}{\lambda_2} \end{pmatrix} \begin{pmatrix} A_i \\ A_{i+1} \end{pmatrix} = \begin{pmatrix} A_{i+1} \\ A_{i+2} \end{pmatrix}. \tag{3.6}$$

Defining this equation as $S\boldsymbol{A}_i = \boldsymbol{A}_{i+1}$, we find $\boldsymbol{A}_{n+1} = S^n \boldsymbol{A}_1$. The eigenvalues of

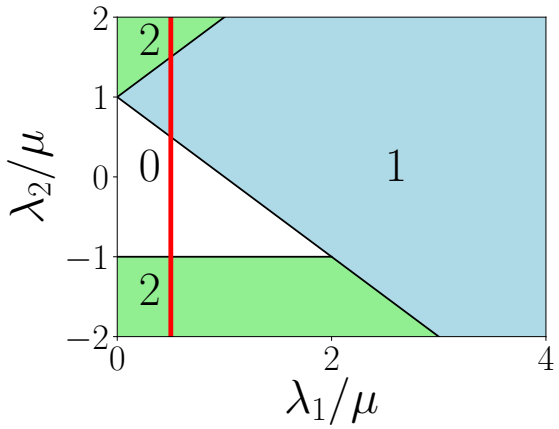

Figure 3.3 Clean phase diagram indicating number of MZMs per edge obtained by considering eigenvalues of the transfer matrix S. The same diagram can be obtained by finding the winding number of the Bloch Hamiltonian [65]. Red line: clean limit of Fig. 3.4.

the transfer matrix S are

$$S\boldsymbol{y}^{\pm} = z^{\pm}\boldsymbol{y}^{\pm}, \qquad z^{\pm} = \frac{-\lambda_1 \pm \sqrt{4\lambda_2\mu + \lambda_1^2}}{2\lambda_2}. \tag{3.7}$$

These candidate zero-energy edge modes must be normalizable which requires $|z| < 1$. Then, $-1/\ln|z|$ gives the localization length of the edge mode (in units of the lattice spacing of the Majorana chain). We confirm in Fig. 3.3 the phase diagram found in Ref. [65] by checking this condition for the two eigenvalues z as a function of λ_1, λ_2 and μ. We see that there are phases with 2 MZMs for $|\lambda_2/\mu| > 1$.

We note that, when $\lambda_2/\mu < -1$, the two MZMs can have the same localization length since $\sqrt{4\lambda_2\mu + \lambda_1^2}$ is purely imaginary up to $\lambda_1/\mu = 2$. This is why two MZMs appear together as we cross the phase boundary at $\lambda_2/\mu = -1$ giving a direct 2-0 MZM transition.

3.4.3 Disorder phase diagram

Having found the phase diagram for the clean case by considering the normalization of the edge modes via transfer matrices, a natural question is whether the same can be done for the disordered case. We will now disorder the chemical potential at each

site, as before, according to $\mu_i = \bar{\mu} + X$. In the disordered case, the transfer matrix S now acquires a site dependence S_i, leading to

$$\boldsymbol{A}_{n+1} = Q_n \boldsymbol{A}_1, \qquad Q_n \equiv \prod_{i=1}^{n} S_i. \tag{3.8}$$

We are ultimately interested in the large-n behavior of the eigenvalues $\zeta_n^{(1,2)}$ of Q_n, characterized by the two "Lyapunov exponents" (LEs) $\gamma_{1,2}$ [66]:

$$\left|\zeta_n^{(1,2)}\right| \propto e^{\gamma_{1,2} n}, \qquad n \gg 1. \tag{3.9}$$

The number of negative LEs will tell us how many normalizable MZMs are present at a given value of $\lambda_1, \lambda_2, \bar{\mu}, \sigma$ and we can construct phase diagrams accordingly, in direct analogy with the clean case. The construction of a phase diagram is thus equivalent to solving for the LEs, which we find using a combination of numerical and analytical techniques.

First, we demonstrate how to find the sum of the LEs analytically. The determinant is the product of eigenvalues:

$$\left|\det\left(Q_n\right)\right| \propto e^{(\gamma_1+\gamma_2)n}, \qquad n \gg 1. \tag{3.10}$$

The determinant product rule $\det\left(Q_n\right) = \prod_{i=1}^{n} \det\left(S_i\right)$, allows us to treat the right-hand-side as a product of random variables. Using the law of large numbers [67] leads to

$$\gamma_1 + \gamma_2 = \int p(\mu) \ln\left|\det S(\mu)\right| d\mu = \frac{1}{2\sigma} \int_{\bar{\mu}-\sigma}^{\bar{\mu}+\sigma} \ln\left|\frac{\mu}{\lambda_2}\right| d\mu, \tag{3.11}$$

for a uniform distribution for the random variable μ. If $\gamma_1 + \gamma_2 < 0$, there exists at least one MZM. On the other hand, $\gamma_1 + \gamma_2 > 0$ means that there can be at most one MZM. This separates parameter space into two regions which interestingly do not depend on λ_1.

Second, we still need one more constraint in order to determine both LEs for a point in parameter space. While analytical solutions for the exponents are rare, it is straightforward to calculate LEs numerically for each realization [66–68]. We use the algorithm outlined in Ref. [66] to determine the maximum LE, $\gamma_{\max}$:

1. Begin with an arbitrary vector $\boldsymbol{r}_0$ which is normalized to 1 and multiply it by m iterations of the random matrix S_i from the left.

2. Store the norm of the resulting vector as R_0 and renormalize the vector to 1. Generically, at step k we store $R_k = |\boldsymbol{r}'_k|, \boldsymbol{r}'_k \equiv \left(\prod_{j=km+1}^{(k+1)m} S_i\right) \boldsymbol{r}_k$ and renormalize the resulting vector $\boldsymbol{r}_{k+1} \to \boldsymbol{r}'_k / |\boldsymbol{r}'_k|$.

3. Repeat the procedure $k = N$ times.

4. The maximum Lyapunov exponent is given by $\gamma_{\max} = \lim_{N\to\infty} \frac{1}{(N+1)m} \sum_{k=0}^{N} \ln [R_k]$.

This procedure relies on the fact that the norm of an arbitrary vector will grow according to the largest eigenvalue of the random matrix product, in analogy with a deterministic product. We split up the product into bins of size $m = 20$ in order to avoid numerical error, since successive multiplication of the random matrix S_i will generically cause the norm of $\boldsymbol{r}$ to tend to either zero or infinity (away from a phase boundary).

Having found the maximum and sum of Lyapunov exponents, we can construct the phase diagram (Fig. 3.4 for $\lambda_1/\bar{\mu} = 0.5$). We notice that, for weak disorder, the diagram is generally unaltered from the clean case (with the notable exception near $\lambda_2/\bar{\mu} = -1$). Physically, this implies that a local qubit constructed out of two MZMs on one side of the chain is able to withstand moderate amounts of disorder. Nevertheless, sufficiently strong disorder induces 2-1 and 1-0 MZM transitions. This can occur because two MZMs do not necessarily possess the same localization length, hence disorder can push one mode into the bulk whilst the other remains. Remarkably, we also find the converse situation in other parts of the phase diagram. Some parts of the clean 0-MZM phase can support an edge mode when disorder is added. Similarly, a 1-MZM phase can support 2 MZMs upon addition of disorder (near $\lambda_2/\bar{\mu} = 1.5$). This is an analog of the disorder-induced topological Anderson insulator for $\mathbb{Z}$-classified models [52].

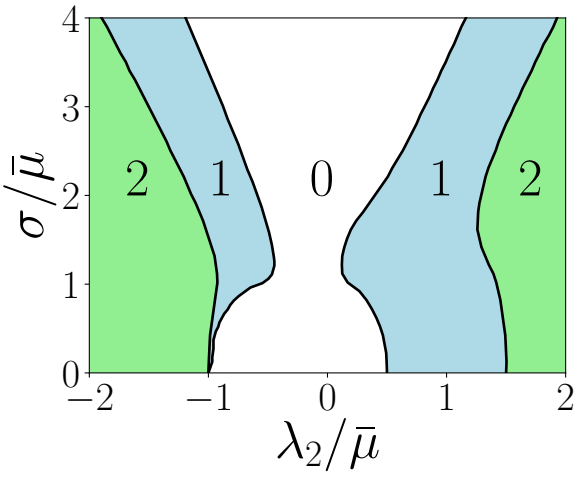

Figure 3.4 Phase diagram indicating the number of MZMs per edge as a function of disorder strength σ for $\lambda_1/\bar{\mu} = 0.5$. The diagram appears qualitatively similar for any choice of $\lambda_1/\bar{\mu} \in [0, 2]$. Note the "tricritical" point $\lambda_2/\bar{\mu} = -1$ on the clean axis where all three phases meet. Lyapunov exponents are calculated for chains of 10^6 sites.

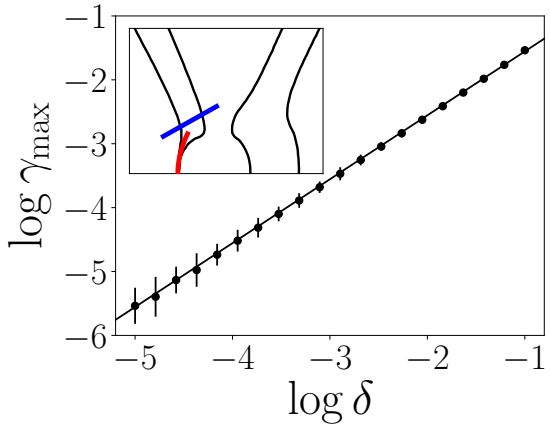

Figure 3.5 The maximum Lyapunov exponent as a function of δ (which parameterizes the $\gamma_1 + \gamma_2 = 0$ path, depicted in red in the inset) on a log-log plot over four decades. ($\lambda_1/\bar{\mu} = 0.5$.) The fitted slope of 1 implies $\gamma_{\max} \propto \delta \propto \sigma^2$ along this path. We use a chain with 2×10^7 sites and average over 10 configurations to estimate errors which increase when the localization length becomes comparable to the length of the chain.

Let us now look more closely at the system near $\lambda_2/\bar{\mu} = -1$. Recall that the clean localization length near the 2-0 boundary is the same for both modes. Disorder is responsible for a splitting of the Lyapunov exponents $\gamma_{1,2}$ of the transfer matrix Q_n in this region. This leads to an anomalous "tricritical point" at $\lambda_2/\bar{\mu} = -1, \sigma = 0$ which separates 2, 1, and 0 MZM regions. We can understand this behavior if we focus on the line in parameter space where $\gamma_1 = -\gamma_2$, which we can determine analytically according to Eq. (3.11). The line is either an exact phase boundary (if $\gamma_1 = \gamma_2 = 0$), or it must lie in the 1-MZM region due to the splitting. At weak disorder, this line is given by $\sigma/\bar{\mu} = \sqrt{6\delta}$ where $\delta = \lambda_2/\bar{\mu} + 1$ (red line in Fig. 3.5 inset). In Fig. 3.5, we present numerical evidence that $\gamma_{\max} \propto \delta \propto \sigma^2$. This suggests that a 1-MZM phase arises between the 2- and 0-MZM phases for an arbitrary amount of disorder. Indeed, this behavior is generic for all $\lambda_1/\bar{\mu}$.

3.4.4 Verification using the entanglement spectrum

We use the "entanglement degeneracy criterion" as an independent method to validate our phase diagram [69–72]. More specifically, we consider the chain in a Majorana basis, impose periodic boundary conditions, and partition the system into two halves. The entanglement spectrum is defined as the set of eigenvalues of the operator $\bar{H} = -\log \mathrm{tr}_N \rho_{gs}$ where ρ_{gs} is the ground state density matrix and we trace over the Majorana modes α_i on half the chain ($1 \leq i \leq N$). The degeneracy of the entanglement spectrum can be used to distinguish distinct topological phases, since the number of entanglement zero-modes coincides with the number of topologically-protected MZMs in the finite system.

Peschel [73] demonstrated that for a quadratic Majorana Hamiltonian, the entanglement spectrum is related to the eigenvalues of the ground state subsystem correlation matrix. The full correlation matrix (in the Majorana basis) is defined as $\kappa_{ij} = \langle \mathrm{vac} | \alpha_i \alpha_j | \mathrm{vac} \rangle$, from which one can read off the subsystem correlation matrix by considering all degrees of freedom which have not been traced away. We then

find that the entanglement spectrum is

$$\tanh\left(\frac{e_{\text{ent}}}{2}\right) = e_{\text{corr}} - 1, \tag{3.12}$$

where e_{ent} are the eigenvalues of the "entanglement Hamiltonian" $\bar{H} = -\log \text{tr}_N \rho_{\text{gs}}$, and e_{corr} are the eigenvalues of the ground state subsystem correlation matrix κ_{sub}. We will calculate the entanglement spectrum by tracing over half the degrees of freedom in the Majorana basis α.

Our original Hamiltonian (3.5) reads

$$\mathcal{H} = \boldsymbol{a}^\dagger \tilde{H} \boldsymbol{a}, \qquad \boldsymbol{a} = \left(a_1, \ldots, a_N, a_1^\dagger, \ldots, a_N^\dagger\right)^T, \tag{3.13}$$

where $a_i^\dagger$ is the fermion creation operator at lattice site i. The Hamiltonian is diagonalized via a unitary Bogoliubov transformation according to

$$\mathcal{H} = \boldsymbol{b}^\dagger \Lambda \boldsymbol{b}, \qquad \boldsymbol{a} = U\boldsymbol{b}, \qquad U^\dagger \tilde{H} U = \Lambda, \qquad \Lambda = \text{Diag}\left[+\epsilon_1, \ldots, +\epsilon_N, -\epsilon_1, \ldots, -\epsilon_N\right]. \tag{3.14}$$

We can define a Majorana basis for both b and a fermion operators according to the following transformation $\boldsymbol{b} = P\boldsymbol{\beta}$, $\boldsymbol{a} = P\boldsymbol{\alpha}$. Using these transformations, we can relate the Majorana modes according to

$$\boldsymbol{\beta} = P^{-1}\boldsymbol{b} = P^{-1}U^{-1}\boldsymbol{a} = P^{-1}U^{-1}P\boldsymbol{\alpha} \equiv W\boldsymbol{\alpha}. \tag{3.15}$$

The correlation matrix of the vacuum is easily determined in the $\boldsymbol{\beta}$ basis. All Bogoliubov annihilation operators b_i will destroy the vacuum state. In other words

$$\left\langle \text{vac} \left| b_p b_q^\dagger \right| \text{vac} \right\rangle = \delta_{p,q} \tag{3.16}$$

$$\left\langle \text{vac} \left| b_p^\dagger b_q \right| \text{vac} \right\rangle = 0 \tag{3.17}$$

$$\left\langle \text{vac} \left| b_p b_q \right| \text{vac} \right\rangle = 0. \tag{3.18}$$

By translating the b operators into Majorana β operators, it follows that

$$T_{pq} \equiv \left\langle \text{vac} \left| \beta_p \beta_q \right| \text{vac} \right\rangle = \delta_{pq} + i\Gamma_{pq}, \qquad \Gamma_{pq} = \mathbb{I}_N \otimes \begin{pmatrix} 0 & 1 \\ -1 & 0 \end{pmatrix}. \tag{3.19}$$

So we have determined the correlation matrix in the β Majorana basis.

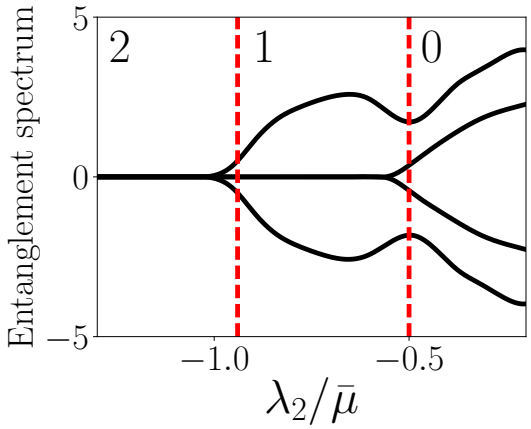

Figure 3.6 Four modes closest to zero energy of the entanglement spectrum (defined in the text) along the line $\sigma = 0.75\lambda_2 + 2\bar{\mu}$, $\lambda_1/\bar{\mu} = 0.5$ (blue line in Fig. 3.5 inset). The red dashed lines indicate the phase transitions based on Lyapunov exponents. The spectrum has 4, 2, or 0 modes with zero energy depending on the topological phase of the system. For the simulation we use $N = 1000$ particles, disorder averaged across 1000 configurations.

Finally, we would like to determine the correlation matrix in the α basis. This can be done with the following transformations

$$\kappa_{ij} = \langle \text{vac} | \alpha_i \alpha_j | \text{vac} \rangle \tag{3.20}$$

$$= \left\langle \text{vac} \left| \left(W^{-1}\boldsymbol{\beta}\right)_i \left(W^{-1}\boldsymbol{\beta}\right)_j \right| \text{vac} \right\rangle \tag{3.21}$$

$$= \sum_{pq} W^{-1}_{ip} W^{-1}_{jq} \langle \text{vac} | \beta_p \beta_q | \text{vac} \rangle \tag{3.22}$$

$$\Rightarrow \kappa = W^{-1} T \left(W^{-1}\right)^T . \tag{3.23}$$

In Fig. 3.6, we plot the four modes closest to zero "energy" in the entanglement spectrum. Indeed we find that gaps in the spectrum align with the phase boundaries derived via Lyapunov exponents. These numerical results agree very well with the semi-analytical Lyapunov method discussed in the previous section.

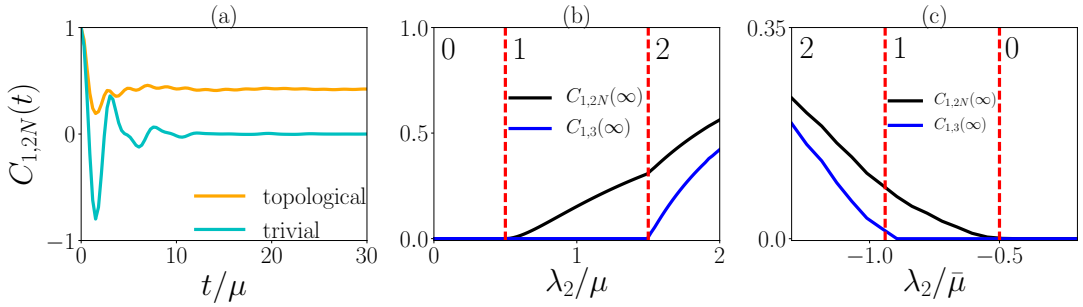

Figure 3.7 (a) Time-dependent, non-local correlator for clean systems at $\lambda_1/\mu = 0.5$, $\lambda_2/\mu = 0.45$ (trivial) and 2.0 (topological). If there are no MZMs (trivial), the long-time value is zero, otherwise it saturates at a non-zero value. (b) Clean long-time saturation value when $\lambda_1/\mu = 0.5$. The non-local (local) correlator signals the onset of the 1 (2)-MZM phase. (c) Disorder-averaged long-time saturation value along the line $\sigma = 0.75\lambda_2 + 2\bar{\mu}$ when $\lambda_1/\bar{\mu} = 0.5$ over 10^4 samples. The behavior is analogous to the clean case. The red dashed lines indicate the phase transitions based on Lyapunov exponents.

3.4.5 Signatures of dynamical correlators

Experimentally diagnosing different regions in our phase diagram is an important issue. In this section we demonstrate that certain time-dependent, *local* correlation functions can identify the onset of a 2-MZM phase, while *non-local* correlators identify the 1 MZM phase. Recent studies [74, 75] have found that the long-time values of certain "qubit" correlators will saturate in a topological phase, while they tend to zero in the trivial phase, reminiscent of order parameter behavior. Consider the correlator

$$C_{i,j}(t) = \frac{1}{2}\left\langle \mathrm{vac}\left|\left\{e^{iHt}q_{i,j}e^{-iHt}, q_{i,j}\right\}\right|\mathrm{vac}\right\rangle, \tag{3.24}$$

where $q_{i,j} = i\alpha_i\alpha_j$ and $|\mathrm{vac}\rangle$ is the vacuum of Bogoliubov quasiparticles. Note that $q_{i,j}$ is both Hermitian and unitary which restricts its eigenvalues to ± 1.

We are interested in the time-dependent correlator

$$C_{i,j}(t) = \frac{1}{2}\left\langle \mathrm{vac}\left|\left\{e^{iHt}q_{i,j}e^{-iHt}, q_{i,j}\right\}\right|\mathrm{vac}\right\rangle, \tag{3.25}$$

where $q_{i,j} = i\alpha_i\alpha_j$ and $|\mathrm{vac}\rangle$ is the vacuum of Bogoliubov quasiparticles. We can

relate the Bogoliubov quasiparticles to Majorana modes according to

$$\boldsymbol{b} = U^{-1}\boldsymbol{a} = U^{-1}P\boldsymbol{\alpha} \Rightarrow \boldsymbol{\alpha} = P^{-1}U\boldsymbol{b}. \tag{3.26}$$

If we define $M \equiv P^{-1}U$ then $\boldsymbol{\alpha} = M\boldsymbol{b}$. We will now use these expressions to solve for $C_{i,j}(t)$. Explicitly

$$\begin{aligned} C_{i,j}(t) &= \frac{1}{2}\left(\left\langle \text{vac}\left|e^{iHt}q_{i,j}e^{-iHt}q_{i,j}\right|\text{vac}\right\rangle + \left\langle \text{vac}\left|q_{i,j}e^{iHt}q_{i,j}e^{-iHt}\right|\text{vac}\right\rangle\right) && (3.27)\\ &= \frac{1}{2}\left(\left\langle \text{vac}\left|q_{i,j}e^{-iHt}q_{i,j}\right|\text{vac}\right\rangle + \left\langle \text{vac}\left|q_{i,j}e^{iHt}q_{i,j}\right|\text{vac}\right\rangle\right) && (3.28)\\ &= \frac{1}{2}\left(\left\langle \psi_{i,j}\left|e^{-iHt}\right|\psi_{i,j}\right\rangle + h.c.\right), \qquad |\psi_{i,j}\rangle \equiv q_{i,j}\left|\text{vac}\right\rangle. && (3.29) \end{aligned}$$

We see that $C_{i,j}(t)$ must be real since it is the sum of a complex conjugate pair. Once we note that

$$|\psi_{i,j}\rangle = i\left[\sum_{m=1}^{N}\sum_{n>m}^{N}\left(M_{i,N+m}M_{j,N+n} - M_{j,N+m}M_{i,N+n}\right)b_m^\dagger b_n^\dagger + \sum_{m=1}^{N}M_{i,m}M_{j,N+m}\right]|\text{vac}\rangle, \tag{3.30}$$

we find

$$\begin{aligned} C_{i,j}(t) = &\sum_{m=1}^{N}\sum_{n>m}^{N}\cos\left[\left(\epsilon_m+\epsilon_n\right)t\right]\left|M_{i,N+m}M_{j,N+n} - M_{j,N+m}M_{i,N+n}\right|^2 \\ &+\left|\sum_{m=1}^{N}M_{i,m}M_{j,N+m}\right|^2 \end{aligned} \tag{3.31}$$

In the long-time limit $t \to \infty$ we notice that the terms which dominate $C_{i,j}$ are: 1) the first term in the right-hand-side of (3.31) which is independent of time, and 2) pairs of zero-energy modes m', n' such that $\cos\left[\left(\epsilon_{m'}+\epsilon_{n'}\right)t\right] = 1, \forall t$. In the case when there is no more than 1 zero-mode, then there are no pairs of zero-modes and the first term is the long-time saturation value. Incidentally, the saturation is equivalent to a *static* correlation function

$$\text{if no pairs of zero-modes: } \lim_{t\to\infty} C_{i,j}(t) = K_{i,j} \qquad K_{i,j} = \left|\langle\text{vac}|\, q_{i,j}\,|\text{vac}\rangle\right|^2. \tag{3.32}$$

Only in the presence of 2 or more zero-modes does the long-time saturation value differ from this static correlator $K_{i,j}$.

In Fig. 3.7(a), we show that the long-time behavior of the non-local correlator between the end sites will saturate to a non-zero value in a topological phase (>0

MZMs), whilst the correlator tends to zero in a 0-MZM phase. In Fig. 3.7(b) we plot the long-time saturation of the non-local correlator $C_{1,2N}$ as well as the local correlator $C_{1,3}$ for the clean system. We find that the former serves as an indicator of the 0-1 MZM transition, while the latter signals the 1-2 MZM transition. This is in agreement with our understanding that we require two MZMs with support on odd "sublattice" sites in order to create a local qubit state.

In Fig. 3.7(c), we plot the disorder-averaged correlators across a 2-1-0 path (the same one taken in Fig. 3.6) and find analogous behavior to the clean case. We point out that the standard deviation is quite high at non-zero saturation (~ 0.1) indicating a strong configurational dependence. Nevertheless, one would anticipate a disordered experiment to exhibit non-zero long-time saturation which ought to be observable. We have thus found another useful metric to describe and experimentally diagnose topological phase transitions in the presence of disorder.

3.5 Summary and outlook

We began this chapter by describing the simplest example of a topological superconductor, known as the Kitaev chain. This model has attracted much attention since its ground state possesses a topological degeneracy due to nonlocal Majorana zero modes which can represent a qubit which is immune to several noise channels. We then suggested that *local* zero modes in the presence of disorder may represent a new paradigm in the quest for a stable qubit, and subsequently studied a minimal model which realizes such a setup. Specifically, we investigated the disorder phase diagram of a longer-range Kitaev chain which supports two MZMs on each edge of the chain, thus capable of forming a *local* zero energy excitation representing a qubit. We discover regions of moderate disorder where 2 MZMs are stable, while strong disorder generally drives a $2\to1\to0$ MZM transition. Physically this can occur because two MZMs with the same clean localization length can split in the presence of disorder, with one of them vanishing into the bulk before the other.

In addition, we have uncovered regions where the addition of disorder can induce local zero-modes and found a special tricritical point where the 2, 1, and 0-MZM regions meet as corroborated by a combination of analytical and numerical tools. Our work thus lays the foundation for future studies to further investigate the stability of local zero-modes with respect to other perturbations, including the addition of interactions or environmental dissipation.

Chapter 4

Non-Hermitian symmetry-protected topological phases

Topological band theory was developed to predict and explain robust features in the ground state electronic structure of insulators and superconductors. While these ideas have already found fundamental applications in quantum metrology [21] and quantum computation [20], there has been a recent effort to generalize these concepts to constrain the behavior of many-body atomic, molecular, and optical systems in a non-equilibrium environment. In the rest of this thesis, we will discuss how topological ideas can be leveraged to describe robust dynamical features of these complex systems. This chapter will serve as an introduction to the rapidly-growing field of "non-Hermitian symmetry-protected topological phases," which will be further explored in the following two chapters. We introduce the Bernard-LeClair (BL) classes which generalize the ten Altland-Zirnbauer (AZ) classes in the absence of Hermiticity. Further, we discuss where these BL symmetries arise naturally in a variety of non-equilibrium setups, specifically in quenched bosons, dissipative atoms, and classical photonics.

4.1 Background

Recent efforts in the condensed matter community have aimed to understand the topological properties of electronic ground states in material insulators and superconductors [15, 16]. While the topological band theory of electrons is rapidly becoming a mature field, there has been much recent interest in borrowing topological ideas to describe universal behavior in the non-equilibrium dynamics of atomic, molecular, and optical (AMO) systems. Specifically, we wish to generalize the formalism of symmetry-protected topological order to encompass: (1) classical modes of light in photonic crystals, (2) the Bogoliubov spectra of interacting atomic bosons and non-linear photons, (3) quantum dissipative dynamics of many-particle ensembles. What do these systems have in common? Temporal (or spatial) evolution can be non-unitary due to absorption from a medium, instabilities from a quench or resonant drive, or decoherence processes from an external environment. The non-unitary evolution is generated from a non-Hermitian operator. The study of topological phases in non-Hermitian systems ultimately aims to make robust statements concerning edge modes, degeneracies, and quantized observables in a highly out-of-equilibrium setup.

In this chapter, we outline how the formalism of symmetry-protected topological phases can be applied to systems which do *not* evolve unitarily in time or space. Mathematically, this translates to studying the topological properties of non-Hermitian effective Hamiltonians which generically possess complex "energies," where the real and imaginary parts are related to the frequency and growth/decay rate of modes. The structure of this chapter is as follows: We will first review the Hermitian tenfold way, and motivate why non-Hermitian Hamiltonians can possess a richer set of symmetry classes. Next, we present the non-Hermitian generalization of the Altland-Zirnbauer (AZ) classes via the Bernard-LeClair (BL) symmetry classes. We conclude by demonstrating that BL symmetries arise generically for a wide class of quantum and classical models, specifically in bosonic Bogoliubov-de Gennes (BdG) Hamiltonians and fermionic Lindbladians. The following two chap-

ters study a variety of concrete models which benefit from the general formalism outlined below.

4.2 Beyond the Tenfold way

In Sec. 1.4.5, we discussed the Tenfold way: A bridge which connects ten AZ symmetry classes to the number of topologically distinct ground states for equilibrium fermions. We briefly review these AZ classes, before extending the analysis to non-Hermitian models.

Consider a matrix H which represents a first-quantized Hamiltonian on a lattice, e.g. $\mathcal{H} = \sum_{i,j} H_{i,j} c_i^\dagger c_j$. For any H we can check for the presence of the following symmetries

$$\text{TRS:} \qquad H = xH^*x^\dagger, \qquad xx^* = \pm\mathbb{I} \tag{4.1}$$

$$\text{PHS:} \qquad H = -yH^*y^\dagger, \qquad yy^* = \pm\mathbb{I} \tag{4.2}$$

$$\text{chiral:} \qquad H = -zHz^\dagger, \qquad z^2 = \mathbb{I} \tag{4.3}$$

called time-reversal (TRS), particle-hole (PHS), and chiral symmetry respectively, where x, y, z, are unitary matrices. There are $3 \times 3 + 1 = 10$ distinct classes, since we have 3 options for TRS (no TRS, or $xx^* = +\mathbb{I}$, or $xx^* = -\mathbb{I}$), 3 options for PHS, and chiral symmetry can exist alone in the absence of either. As we demonstrated in Chapter 1, imposing these various symmetries will have a direct consequence on the values that a bulk topological index can assume (e.g. the sum of Chern numbers of occupied bands with $xx^* = -\mathbb{I}$ TRS must be zero in quantum spin Hall systems). One can also use these symmetries to construct adiabatic arguments for the stability of edge modes in real-space (e.g. spin edge modes in the gap are protected via Kramers degeneracy in the quantum spin Hall effect).

A central assumption of the Tenfold way analysis is Hermiticity of the Hamiltonian $H = H^\dagger$. For systems which evolve non-unitarily in time/space, this Hermiticity condition will be violated. Can these systems possess unique symmetries which protect topological signatures?

Hermitian TRS and PHS are "anti-linear," meaning that they involve complex conjugation of the Hamiltonian matrix H. Non-unitary time evolution is generated by an effective non-Hermitian Hamiltonian $H \neq H^\dagger \implies H^* \neq H^T$. The TRS can then be mathematically represented in two distinct ways: $H = xH^*x^\dagger$ or $H = xH^Tx^\dagger$, which are redundant expressions in the Hermitian limit, but impose independent constraints for non-Hermitian models. The same is true for PHS. This suggests that non-Hermitian Hamiltonians can display a richer set of topologically-important symmetries, since taking the transpose is an inequivalent operation from complex conjugation.

4.3 Bernard-LeClair symmetries

A few years after the analysis of Altland and Zirnbauer [32] (but before the rise of topology in condensed matter), Bernard and LeClair (BL) generalized random matrix ensembles to incorporate classes which violate Hermiticity [76]. The resulting classification is based on the presence or absence of the following relationships, which are called K, C, P, Q symmetries respectively

$$K: \qquad H = \epsilon_k k H^* k^\dagger, \qquad kk^* = \pm\mathbb{I} \tag{4.4}$$

$$C: \qquad H = \epsilon_c c H^T c^\dagger, \qquad cc^* = \pm\mathbb{I} \tag{4.5}$$

$$P: \qquad H = -pHp^\dagger, \qquad p^2 = \mathbb{I} \tag{4.6}$$

$$Q: \qquad H = \epsilon_q q H^\dagger q^\dagger, \qquad q^2 = \mathbb{I} \tag{4.7}$$

where $\epsilon_{c,q,k} = \pm 1$, $\mathbb{I}$ is the identity, and p, c, k, q are unitary matrices. The K and C symmetries are non-Hermitian generalizations of TRS (if $\epsilon_c = \epsilon_k = +1$) and PHS (if $\epsilon_c = \epsilon_k = -1$). If a Hamiltonian has two types of K symmetries ($\epsilon_k = \pm 1$) then it is guaranteed a P symmetry, which is just chiral symmetry from the AZ classification. This is also true for a Hamiltonian with two types of C symmetries. If a Hamiltonian has both C and K symmetry, then it is guaranteed a Q symmetry (called pseudo-(anti)-Hermiticity), by putting these together.

BL originally uncovered 43 equivalence classes based on the presence or absence of these four relations (in analogy with the ten AZ classes). Two very recent studies [77, 78] have constructed a topological classification table using the BL classes as a basis (in analogy with Tenfold way), which suggest that only 38 of them are topologically distinct. We briefly outline how different symmetry classes are defined, pointing to Refs. [76, 77, 79] for a more detailed treatment.

The Q and K symmetries involve complex conjugation of the Hamiltonian matrix H. This implies that an $\epsilon_{k,q} = +1$ symmetry can transform into a $\epsilon_{k,q} = -1$ symmetry by scaling H by an imaginary unit: $H \to iH$. While this transformation will affect the spectrum, the topological properties of a Hamiltonian will be preserved under multiplication by a constant hence we identify classes which are related in this way as equivalent. This redundancy can be exploited such that only the sign of ϵ_c is meaningful to distinguish between unique classes.

Let us consider what happens when a Hamiltonian has more than one symmetry. As an example consider a Hamiltonian with both P and C symmetry

$$H = -pHp^\dagger \tag{4.8}$$

$$H = \epsilon_c c H^T c^\dagger. \tag{4.9}$$

Substituting one expression into the other leads to

$$H = -\epsilon_c c p^* H^T p^T c^\dagger \tag{4.10}$$

$$H = -\epsilon_c p c H^T c^\dagger p^\dagger. \tag{4.11}$$

If p, c are both unitary matrices, these expressions can be satisfied in two different ways: $c = \epsilon_{cp} p c p^T$ where $\epsilon_{cp} = \pm 1$. We find that classes with multiple symmetries are distinguished by how the unitary transformation matrices are related to each other.

4.4 Q symmetry protects edge modes in 1D

Having drawn parallels between the Bernard-LeClair and Altland-Zirnbauer symmetries, we now provide an explicit example where a BL symmetry protects edge modes in a non-Hermitian tight-binding model.

Esaki *et al.* [80] were the first to show that Q symmetry can be used to construct an adiabatic argument for the stability of edge modes in real space. Consider the 1D dissipative SSH model

$$\mathcal{H}_{\text{dSSH}} = v\sum_{i=1}^{m}\left(c_{A,i}^{\dagger}c_{B,i} + h.c.\right) + w\sum_{i=1}^{m-1}\left(c_{B,i}^{\dagger}c_{A,i+1} + h.c.\right) - iu\sum_{i=1}^{m} c_{B,i}^{\dagger}c_{B,i}, \quad (4.12)$$

where $u, v, w \in \mathbb{R}$ and $c_{A/B,i}$ represents an annihilation operator on lattice site i in sublattice site A/B [81]. This can be written as $\mathcal{H}_{\text{dSSH}} = \mathbf{c}^{\dagger}H_{\text{dSSH}}\mathbf{c}$. The Hamiltonian matrix H_{dSSH} does *not* have time-reversal, particle-hole, or chiral symmetry and therefore belongs to class A. The Hermitian Tenfold way analysis would suggest that this model ought to be trivial in 1D; however, this model still hosts strongly protected edge modes. While chiral symmetry is broken, edge modes are protected by a Q symmetry: $H_{\text{dSSH}} = -\tau_z H_{\text{dSSH}}^{\dagger}\tau_z$, $\tau_z = \mathbb{I}_N \otimes \sigma_z$, (the 2×2 space represents sublattice sites) which constrains edge mode energies via $E_{\text{edge}} = -E_{\text{edge}}^{*}$. (The right and left eigenvectors of the edge mode are related via: $\psi_{\text{right}} \propto \tau_z\psi_{\text{left}}^{*}$ which ensures edge mode energies are purely imaginary.) This is in direct analogy with how chiral symmetry pins SSH edge mode energies to obey $E_{\text{edge}} = -E_{\text{edge}} = 0$. For the non-Hermitian problem, any (complex gap preserving) disorder entering the Hamiltonian which respects Q symmetry will ensure that edge modes will have exactly zero real energy, $\text{Re}[E_{\text{edge}}] = 0$, but their imaginary energy can be arbitrary. This provides an explicit example where a BL symmetry can be used to construct an adiabatic argument for the stability of edge modes. We will discuss another example in Ch. 6, where C symmetry can protect zero-energy Majorana modes in 1D and 2D.

4.5 Where to find BL symmetries?

We have mathematically motivated why topological edge modes and invariants might be protected by BL symmetries which generalize the canonical AZ symmetries in the absence of Hermiticity. An important next step is to address where these symmetries arise physically. TRS and PHS are robust symmetries which arise in fermionic insulators and superconductors. Sublattice symmetry (lack of direct hopping between two different sublattices) manifests itself in chiral symmetry. Where do Q and C symmetries arise in nature? We address this fundamental question in the rest of this chapter.

4.5.1 Q symmetry in the bosonic BdG equation

We have encountered the bosonic BdG Hamiltonians in Chs. 1 and 2 in our discussion of superfluids. We repeat the steps of the Bogoliubov transformation in order to emphasize the BL symmetries which are inherent to the BdG equation. Specifically, we demonstrate that the spectrum of every Hermitian bosonic BdG Hamiltonian is found via the eigenvalues of a non-Hermitian matrix [82]. We then sort this matrix into one of the BL classes.

Let us consider a *Hermitian* $2N \times 2N$ bosonic BdG Hamiltonian

$$\mathcal{H} = \mathbf{b}^\dagger \tilde{H} \mathbf{b}, \qquad \mathbf{b} = \left(b_1, \ldots, b_N, b_1^\dagger, \ldots, b_N^\dagger\right)^T, \tag{4.13}$$

where we consider N types of bosons b and

$$\tilde{H} = \begin{pmatrix} B & A \\ A^* & B^T \end{pmatrix}, \tag{4.14}$$

represents the most general form where $B = B^\dagger, A = A^T, \tilde{H} = \tilde{H}^\dagger$. We define the transformation

$$\mathbf{b} = T\beta, \qquad \mathbf{b}^\dagger = \beta^\dagger T^\dagger, \qquad T = \begin{pmatrix} U & V \\ V^* & U^* \end{pmatrix}, \tag{4.15}$$

such that

$$\mathcal{H} = \beta^\dagger \Sigma_z \Lambda \beta, \tag{4.16}$$

where $\Sigma_z = \sigma_z \otimes \mathbb{I}_N$ and Λ is a diagonal matrix. If we impose bosonic commutation relations on the quasiparticles β then the transformation T must obey

$$T\Sigma_z T^\dagger = \Sigma_z \Rightarrow T^{-1} = \Sigma_z T^\dagger \Sigma_z, \tag{4.17}$$

which implies T is *paraunitary* (i.e. non-unitary). In addition, T needs to diagonalize the Hamiltonian

$$T^\dagger \tilde{H} T = \Sigma_z \Lambda \Rightarrow \tilde{H} T = \left(T^\dagger\right)^{-1} \Sigma_z \Lambda = \Sigma_z T \Lambda. \tag{4.18}$$

Multiplying by Σ_z on the left leads to

$$\Sigma_z \tilde{H} T = T \Lambda, \tag{4.19}$$

which implies that the eigenvalues of $H_{\text{BdG}} \equiv \Sigma_z \tilde{H}$ will determine the spectrum of the system, and the right eigenvectors will determine the transformation matrix T. We refer to (4.19) as the bosonic BdG equation, and point out two symmetries built into H_{BdG}

$$Q: \qquad H_{\text{BdG}} = \Sigma_z H_{\text{BdG}}^\dagger \Sigma_z \tag{4.20}$$

$$K: \qquad H_{\text{BdG}} = -\Sigma_x H_{\text{BdG}}^* \Sigma_x, \tag{4.21}$$

corresponding to a Q symmetry with $\epsilon_q = +1$ (pseudo-Hermiticity) and a K symmetry with $\epsilon_k = -1, kk^* = \mathbb{I}$ (particle-hole) [83]. This class is also defined by: $q = -kq^*k^\dagger$ from the commutation condition, where the minus sign distinguishes it from the Hermitian class D. Thus while the Hamiltonian (4.13) is Hermitian, the spectrum is equivalent to the eigenvalues of a non-Hermitian matrix.

Note that this analysis does not apply to fermionic BdG models (i.e. superconductors). These are diagonalized by a unitary transformation such that the fermionic BdG equation is particle-hole symmetric and Hermitian: $\epsilon_q = +1, q = \mathbb{I}, q = +kq^*k^\dagger$, representing class D [32].

The non-Hermiticity of H_{BdG} suggests that imaginary modes can appear which are populated exponentially fast in time (also known as dynamically-unstable modes). Physically, these modes can arise if bosons condense in a state which does not minimize the mean-field energy of the evolving Hamiltonian, such as after a quench protocol. The simplest example of this is called a roton instability. In the Bogoliubov approximation, the weakly-interacting spectrum of a $k = 0$ condensate reads

$$E_k = \sqrt{\epsilon_k(\epsilon_k + 2nV_k)} \tag{4.22}$$

where ϵ_k is the kinetic energy, n is the density of bosons, and V_k is the Fourier transform of the interaction profile. (See Sec. 1.3.2.) Notice that if $\epsilon_k + 2nV_k < 0$ then the argument under the square root is negative and the Bogoliubov spectrum becomes *complex*. This is called a roton instability, and has recently been observed by quenching the dipolar interaction profile in a condensate of Erbium atoms [50]. By quenching from a system with a stable spectrum to one with a roton instability, the condensate depletes from the $k = 0$ mode to some higher-wavevector mode $k = \pm Q$. This condensate depletion mechanism is absent from fermionic BdG models, and is the physical reason why bosonic and fermionic BdGs belong to separate symmetry classes.

4.5.2 C symmetry in fermionic Lindbladians

Consider a *non-Hermitian* fermionic BdG Hamiltonian

$$\mathcal{H} = u\sum_n c_n^\dagger c_n - J\sum_n \left(c_n^\dagger c_{n+1} + c_n^\dagger c_{n+1}^\dagger + h.c.\right), \tag{4.23}$$

where $u \in \mathbb{C}, J \in \mathbb{R}$ and c_n represents a complex spinless fermion on site n. The Hamiltonian is rewritten as

$$\mathcal{H} = \mathbf{c}^\dagger H \mathbf{c}, \qquad \mathbf{c} = \left(c_1, \ldots, c_N, c_1^\dagger, \ldots, c_N^\dagger\right)^T, \tag{4.24}$$

where H is a $2N \times 2N$ non-Hermitian matrix. In the language of the BL scheme, the particle-hole structure of the BdG formalism imposes a C symmetry on the

Hamiltonian, but explicitly breaks K symmetry

$$C: \qquad H = -\Sigma_x H^T \Sigma_x \tag{4.25}$$

$$K: \qquad H \neq -\Sigma_x H^* \Sigma_x, \tag{4.26}$$

where $\Sigma_x = \sigma_x \otimes \mathbb{I}_N$. We emphasize that in the Hermitian limit (when $u \in \mathbb{R}$), $H^* = H^T$ such that the C and K symmetries are redundant. The C symmetry is the non-Hermitian generalization of particle-hole symmetry, which comes from making the replacement: $c_i^\dagger c_j = 1/2(c_i^\dagger c_j - c_j c_i^\dagger)$, $c_i^\dagger c_j^\dagger = 1/2(c_i^\dagger c_j^\dagger - c_j^\dagger c_i^\dagger)$; in other words, it is generic as long as the Hamiltonian is quadratic in fermionic operators (regardless of its Hermiticity).

There are two ways that a non-Hermitian quadratic fermion operator will govern the dynamics of Lindbladian time evolution in dissipative fermionic systems: (1) in the "stochastic wavefunction" approach in the absence of a "quantum jump event," [84] and (2) using the method of "third quantization" of the density operator [85]. We will only discuss the first case in this thesis; the second is work in progress.

A quantum many-body system in contact with an external environment will generically undergo non-unitary time evolution due to the possibility of particles which can be injected into or removed from the system [84]. The most general (Markovian) description involves evolution of the system's density matrix according to a Lindblad master equation [86]

$$\frac{d\rho}{dt} = -i[H, \rho] + \mathcal{L}(\rho), \tag{4.27}$$

where $\rho = \sum_\alpha p_\alpha |\psi_\alpha\rangle \langle\psi_\alpha|$ is the density matrix, H is the Hermitian time-evolution of the system in the absence of decoherence processes, and $\mathcal{L}(\rho)$ is a "superoperator" which takes one density matrix to another

$$\mathcal{L}(\rho) = -\sum_k \frac{\gamma_k}{2}\left(L_k^\dagger L_k \rho + \rho L_k^\dagger L_k - 2L_k \rho L_k^\dagger\right). \tag{4.28}$$

The L_k operators represent decoherence processes which serve to destroy the otherwise unitary time evolution of the system. By defining the quantity: $H_{\text{eff}} =$

$H - i\sum_k (\gamma_k/2) L_k^\dagger L_k$, we can rewrite the master equation in a simpler form

$$\frac{d\rho}{dt} = -i[H_{\text{eff}}, \rho] + \sum_k \gamma_k L_k \rho L_k^\dagger. \tag{4.29}$$

This has a convenient physical interpretation: In a time step dt, a system prepared in a pure state will either evolve coherently according to a non-Hermitian effective Hamiltonian H_{eff}, or a "quantum jump event" will occur which moves the pure state from $|\psi_\alpha\rangle$ to $L_k|\psi_\alpha\rangle$. Averaging over all such trajectories will produce the same expectation values as formally solving the Lindblad master equation for the evolution of the density matrix. This is called the "stochastic wavefunction approach" to incoherent systems.

If we prepare the system in a pure state, there are certain cases when experimentally we can constantly check for the presence or absence of a jump event [87] (e.g. if the jump event involves removing the particle from the system via emitting a photon into a cavity mode, then we can constantly monitor the cavity for the presence of a photon). In doing so, we perform a partial measurement of the system, inducing non-unitary time evolution. In the absence of a quantum jump event, the system undergoes *coherent* non-unitary time evolution according to H_{eff}. In Ch. 6, we will find that it is possible to use the framework of non-Hermitian topology to make robust statements about the degeneracy of the steady-state of a system which evolves according to H_{eff}.

4.5.3 Non-Hermitian classical optics

So far, we have discussed how non-unitary time evolution can occur in quantum systems out of equilibrium, either due to instabilities of a condensate or due to decoherence processes. In this subsection, we discuss how non-Hermitian single-particle Hamiltonians can be simulated in classical optics via the paraxial equation. Non-unitary spatial evolution of an electric field amplitude can occur due to dissipation of an electric field into a material. The setup described here is the starting point for the field of PT-symmetric photonics [88–90].

Consider a 2D electrical field $E(x,y) = e^{ik_0 y}\psi(x,y)$ propagating in a medium with a spatially varying refractive index $n(x)$. A given component of the field will satisfy the scalar Helmholtz equation

$$\left(\frac{\partial^2}{\partial y^2} + \frac{\partial^2}{\partial x^2} + k^2\right) E(x,y) = 0, \tag{4.30}$$

where $k = n(x)\omega/c$, ω is the temporal frequency of the wave, $n(x) = n_0(1 + v(x))$. We make the assumptions: (1) $v(x) \ll 1$, and (2) $\partial^2\psi/\partial y^2 \ll \partial^2\psi/\partial x^2$, which physically implies that the refractive index changes slowly around a mean value, and the beam has small deviations in the transverse direction x as a function of propagation in the y direction with wavevector k_0. The "paraxial" equation which governs the envelope function $\psi(x,y)$ reads

$$i\frac{\partial\psi}{\partial y} = -\left[\frac{1}{2k_0}\frac{\partial^2}{\partial x^2} + k_0 v(x)\right]\psi, \tag{4.31}$$

which is mathematically equivalent to a Schrödinger equation with two main differences: (1) instead of propagating a wavefunction in time, it propagates an envelope function in the y direction, and (2) the potential $v(x)$ is the deviation of the refractive index of the material which can be a complex function, representing material losses or optical gain depending on the sign of the imaginary part. In PT-symmetric systems, $v(x) = v(-x)^*$ which leads to a non-Hermitian time-independent Hamiltonian which can in some cases still possess purely real eigenvalues. This leads to interesting scenarios where certain electric fields maintain their amplitude in the presence of both loss and gain in the medium. If the refractive index is chosen to be translationally invariant $v(x + X) = v(x)$, eigenstates are labeled by a Bloch wavenumber in analogy to single-particle eigenstates in a crystal.

The field of "topological photonics" is actively being pursued by a number of groups, both experimentally and theoretically [91, 92]. Can modes of light propogating through a medium possess topological protection [93]? If material losses are accounted for, the problem is generically non-Hermitian and we can exploit BL symmetries to constrain the behavior of edge modes in dissipative environments.

4.6 Properties of non-Hermitian matrices

Before concluding this chapter, we briefly review some basic properties of non-Hermitian matrices which will be useful for the rest of this thesis. Consider a non-Hermitian matrix H. We say that the matrix is diagonalizable if we can perform the transformation

$$VHV^{-1} = \Lambda, \qquad V^\dagger \neq V^{-1}, \tag{4.32}$$

where Λ is a diagonal matrix, and V is a non-unitary transformation. (In the Hermitian limit, V must be unitary.) The non-unitarity of V implies that there are "right" and "left" eigenvectors associated with each eigenvalue, defined below

$$H\mathbf{x}_i = E_i\mathbf{x}_i, \qquad \mathbf{y}_i^\dagger H = E_i\mathbf{y}_i^\dagger, \qquad \mathbf{y}_i^\dagger \cdot \mathbf{x}_j = \delta_{ij}, \tag{4.33}$$

where for each eigenvalue E_i we have an associated right eigenvector $\mathbf{x}_i$ and a left eigenvector $\mathbf{y}_i^\dagger$, which satisfy "biorthonormality" conditions. It is sometimes convenient to rewrite the middle equation above as: $H^\dagger\mathbf{y}_i = E_i^*\mathbf{y}_i$, hence the left eigenvector of H is related to the right eigenvector of $H^\dagger$.

Unlike the Hermitian case, there are certain non-Hermitian matrices which we *cannot* diagonalize, and generically this gives rise to a degeneracy. These are called exceptional points. As a simple example, consider the matrix

$$H_{ep} = \begin{pmatrix} 0 & 1 \\ 0 & 0 \end{pmatrix}. \tag{4.34}$$

Solving the secular equation for the eigenvalues leads to the conclusion that both are zero. However we can only find one eigenvector: $(1,0)^T$ with zero eigenvalue. Two eigenvectors can "coalesce" into one at the degeneracy point, making it impossible to diagonalize the matrix. Interesting topological effects can occur if the Bloch Hamiltonian "encircles" an exceptional point in parameter space.

Finally, we will often be dealing with non-Hermitian matrices which possess an anti-linear symmetry of the form: $H = UH^*U^\dagger$, which can lead to interesting properties for the spectrum. (Celebrated examples of this include PT symmetry [89]

and pseudo-Hermiticity [94].) Imposing such an anti-linear symmetry means that each eigenvalue is either purely real (if the associated right eigenvector is symmetric: $\mathbf{x}_i \propto U\mathbf{x}_i^*$), or must come in a complex conjugate pair with another eigenvector (if $\mathbf{x}_i \not\propto U\mathbf{x}_i^*$). These two types of eigenvalues are called unbroken and broken respectively. (This is because the eigenvector either is symmetric with respect to U or it breaks the symmetry.) As we tune parameters of the matrix, a transition can occur between parameter regimes where all eigenvalues are purely real (unbroken), and regions where certain modes come in complex conjugate pairs (broken). Generically, one must pass the system through an exceptional point (spectral degeneracy) to move between phases since two real eigenvalues must become degenerate to adiabatically form a complex conjugate pair.

4.7 Summary and outlook

In this chapter, we have suggested that ideas from topological band theory can be applied to systems which evolve according to a non-Hermitian Hamiltonian. We introduced and motivated the importance of the Bernard-LeClair symmetries which generalize the canonical Altland-Zirnbauer ones in the absence of Hermiticity. Very recent studies [77, 78] have used the enlarged set of BL classes as a basis to construct a symmetry-based topological classification table in direct analogy with the Tenfold way. This provides a map in the hunt for topologically robust behavior in open, non-equilibrium systems.

The rest of the chapter was dedicated to physical motivations for the framework of non-Hermitian topology. Specifically, we addressed where BL symmetries arise naturally in various non-equilibrium quantum and classical setups.

We first suggested that *Hermitian* bosonic BdG models (which are the analog of fermionic topological superconductors), fall outside the Tenfold way but belong to one of the BL classes with a guaranteed Q (pseudo-Hermiticity) and K (particle-hole) symmetry. This is because the dynamical matrix that one needs to diagonalize

to find the spectrum is inherently non-Hermitian due to the paraunitary transformation which preserves bosonic commutation relations. Thus if we want to fully understand the topological band theory of quadratic bosons, we are naturally led to the topological classification of the BL classes. Bosonic BdG models are used to model a wide variety of physical systems, including: cold atomic gases in a mean-field approximation [95, 96], photons propagating in a nonlinear (potentially driven) medium [97–99], and spin-wave excitations in magnets after Holstein-Primakoff transformation [100]. In the next chapter we will introduce the concept of a "topological edge instability" which can occur in these systems.

Next, we demonstrated that *non-Hermitian* quadratic fermion operators (with anomalous terms $c_i^\dagger c_j^\dagger$) still possess a particle-hole symmetry reminiscent of their Hermitian counterparts (i.e. topological superconductors). However, this particle-hole symmetry manifests itself mathematically as a C symmetry rather than a K symmetry in the BL language. Furthermore, quadratic Fermi operators generate the dynamics of certain dissipative systems in the Lindblad formalism. In Ch. 6 we will show that this generalized particle-hole symmetry can be used to protect gapless Majorana modes in a dissipative system, leading to a topologically-degenerate steady-state.

We discussed how non-Hermitian single-particle Hamiltonians generate the spatial evolution of certain classical modes of light within the paraxial approximation, due to inherent losses/gain from the underlying medium. Modes of light can exhibit topological protection, and non-Hermitian symmetries can be responsible as we shall soon see.

Finally, we summarized a few facts about non-Hermitian matrices which will be useful in the following two chapters.

Chapter 5

Topological phases in the non-Hermitian Su-Schrieffer-Heeger model

In this chapter, we study three variants of the canonical Su-Schrieffer-Heeger (SSH) model which break Hermiticity: two tight-binding models which are relevant for classical light-matter systems, and one bosonic-BdG model which is relevant for quenched condensates. Emphasis is placed on the Bernard-LeClair symmetries identified in the previous chapter. Any chirally-symmetric SSH model will also possess a C symmetry which is directly responsible for a quantized "complex" Zak (cZak) phase which leads to a bulk-boundary correspondence if Hermiticity is broken in the phase of the hopping. If the magnitude of the hopping is asymmetric, there is a breakdown of the bulk-boundary correspondence. The presence of an imaginary staggered potential breaks chiral symmetry but preserves PT and Q symmetry. The latter is important to ensure that boundary modes have exactly zero real energy. Finally, we study a Hermitian SSH model with diagonal bosonic pairing terms, resulting in a "topological edge instability." We draw connections to the fermionic Kitaev chain.

5.1 Background

Recent studies suggest that non-Hermitian analogs of the Su-Schrieffer-Heeger (SSH) model are relevant for describing one-dimensional (1D) topological behavior in open systems with gain and/or loss. Specifically, a number of theoretical works have suggested methods to achieve PT-symmetric versions of the SSH model in an optical setting by adding imaginary onsite potentials to sublattice sites [80, 81, 101–103], with recent experimental successes demonstrating the existence of robust edge states [104–107] and quantized observables. Analogous behavior has been found in higher dimensional models [108]. Thus an active area of research aims to characterize topological phenomena in non-Hermitian models [80, 108–113].

In this chapter, we introduce a new variant of the SSH model which breaks Hermiticity but preserves chiral sublattice symmetry [114]. This is achieved via asymmetric forward/backward hopping terms which couple the nearest-neighbor sites. This simple model preserves the relevant symmetries which arise in a more realistic description of plasmonic dispersion on a 1D chain of nanoparticles via a classical Green's function approach [115]. We demonstrate that this model has a quantized "complex" Zak (cZak) phase due to a C symmetry, which leads to the presence of gapless edge modes. Since publication of this work, the chiral SSH model has been widely studied since it is the simplest example of a Hamiltonian which has "anomalous bulk-boundary correspondence," also known as the non-Hermitian skin effect: If the magnitude of the forward and backward hopping amplitudes are different, then the spectrum can change dramatically depending on the boundary conditions of the model [116, 117]. A number of theoretical works have studied this effect, and it is briefly discussed towards the end of the subsection 5.2.3. We also revisit the well-studied PT-symmetric SSH model [80, 101], emphasizing the importance of the Q symmetry which generalizes chiral symmetry in the non-Hermitian case.

Towards the end of this chapter, we study the simplest example of a bosonic BdG Hamiltonian which undergoes a topological phase transition [95]. A Hermitian SSH model in the presence of diagonal bosonic pairing terms will generate dynamical

instabilities which are localized at the edge of the sample, known as a topological edge instability. These modes appear as bosonic counterparts of Majorana modes in the Kitaev chain, and we discuss their robustness.

5.2 Non-Hermitian single-particle SSH models

As mentioned in the previous chapter, non-Hermitian single-particle Hamiltonians describe the spatial evolution of wavefronts in the paraxial limit if material losses are taken into account. We begin by studying the most general 1D nearest-neighbor tight binding model on a bipartite lattice without assuming Hermiticity. Consider N pairs of particles on a finite chain with Hamiltonian

$$\begin{aligned}\mathcal{H}^{\text{hop}} = &\sum_{n=1}^{N} \left(v_1 \left|n, B\right\rangle \left\langle n, A\right| + v_2 \left|n, A\right\rangle \left\langle n, B\right|\right) \\ &+ \sum_{n=1}^{N-1} \left(w_1 \left|n+1, A\right\rangle \left\langle n, B\right| + w_2 \left|n+1, B\right\rangle \left\langle n, A\right|\right),\end{aligned} \tag{5.1}$$

where we do *not* assume $v_1 = v_2^*, w_1 = w_2^*$ [114, 118, 119]. (See Fig. 5.1 top.) In addition to the hopping, we will consider an imaginary staggered potential when discussing the PT-symmetric case, given by the term

$$\mathcal{H}^{\text{pot}} = iu \sum_{n=1}^{N} \left(\left|n, A\right\rangle \left\langle n, A\right| - \left|n, B\right\rangle \left\langle n, B\right|\right). \tag{5.2}$$

The full Hamiltonian reads $\mathcal{H} = \mathcal{H}^{\text{hop}} + \mathcal{H}^{\text{pot}}$. If periodic boundary conditions are assumed, then the system possesses discrete translational invariance and hence may be diagonalized according to Bloch's theorem by considering eigenvectors of the form

$$\left|\psi_k\right\rangle = \frac{1}{\sqrt{N}} \sum_{n=1}^{N} e^{ikn} \left(a_k, b_k\right) \begin{pmatrix} \left|n, A\right\rangle \\ \left|n, B\right\rangle \end{pmatrix}. \tag{5.3}$$

Substituting this ansatz into (5.1) leads to the equation

$$\begin{pmatrix} iu & w_1 e^{-ik} + v_2 \\ w_2 e^{ik} + v_1 & -iu \end{pmatrix} \begin{pmatrix} a_k \\ b_k \end{pmatrix} = E(k) \begin{pmatrix} a_k \\ b_k \end{pmatrix} \tag{5.4}$$

where the 2×2 matrix above is defined as the bulk Hamiltonian $H(k)$. Solving for the bulk dispersion $E(k)$ and corresponding eigenvectors provides us with all the modes

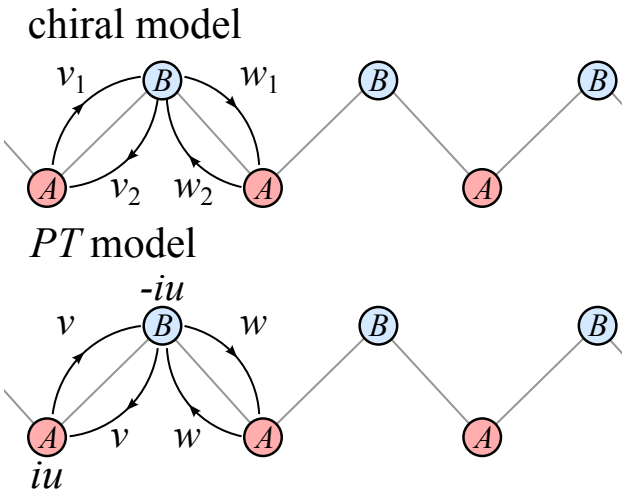

Figure 5.1 *Top*: Chiral SSH with non-Hermitian hopping parameters, no potential. *Bottom*: Chirally-broken, PT-symmetric SSH with non-Hermitian staggered potential.

in the model except edge modes, which only appear in the finite chain Hamiltonian without periodic boundary conditions (5.1). The bulk-boundary correspondence states that an invariant calculated from the bulk Hamiltonian can predict how many gapless, topologically-protected edge modes to expect in the finite system [120].

In what follows, we will be concerned with two distinct scenarios: (1) completely general hopping in the absence of a staggered potential $u = 0$, which is referred to as the chirally-symmetric case; (2) real, symmetric hopping (up to a gauge) in the presence of an imaginary potential $v_1 = v_2 = v \in \mathbb{R}, w_1 = w_2 = w \in \mathbb{R}, u \neq 0, u \in \mathbb{R}$, which is referred to as the PT-symmetric case. Figure 5.1 gives an illustration of the two setups.

5.2.1 Symmetries

We discuss the symmetries in the absence of a staggered potential $u = 0$. Restricting hopping to nearest-neighbors implies that the Hamiltonian possesses chiral symmetry, defined by $\sigma_z H(k)\sigma_z = -H(k)$, where σ_i refers to Pauli matrices. This results in eigenvalues $E(k)$ which come in $\pm$ pairs at a given k. Chiral symmetry implies a C symmetry: $H(k) = \sigma_x H(k)^T \sigma_x$ since both conditions are satisfied only if the bulk

SSH parameters	symmetries
$u = 0$	chiral sublattice, C
$v_1 = v_2^*, w_1 = w_2^*$	PT, Q

Table 5.1: Chart summarizing the symmetries for the two types of SSH tight-binding models.

Hamiltonian lacks a term proportional to σ_z. We will show that this is the necessary ingredient for a quantized cZak phase. If $w_1 = w_2, v_1 = v_2$ then H possesses inversion symmetry defined as $\sigma_x H(k)\sigma_x = H(-k)$, which implies $E(k) = E(-k)$.

In the presence of an imaginary staggered potential $u \neq 0$ and real hopping $v_1 = v_2 = v, w_1 = w_2 = w$, chiral symmetry is broken but the system possesses PT-symmetry defined by $H(k) = \sigma_x H(k)^* \sigma_x$. Generally, PT-symmetric models have two parameter regimes called the "broken" and "unbroken" phases [89, 90]. The unbroken phase has attracted much attention, since it is defined by a fully real spectrum and eigenvectors which are PT-symmetric $|\psi_k\rangle = \sigma_x |\psi_k\rangle^*$. The unbroken phase for our model occurs when $u < |v - w|$. The PT-symmetric model possesses a Q symmetry: $H(k) = -\sigma_z H(k)^\dagger \sigma_z$, which is responsible for a topological transition (discussed below). Note that the Q symmetry reduces to chiral symmetry in the case of a Hermitian Hamiltonian. Table 5.1 summarizes the symmetries for the two models.

Chiral symmetry ensures that $N_A - N_B$ is a topological invariant, where $N_{A/B}$ is the number of zero-energy edge modes with support on sublattice A/B on the left side of the chain [35, 119]. This is because topologically-protected edge modes are their own chirally-symmetric partners, which pins their energy to zero. By considering the two completely dimerized regimes $|v_{1,2}| = 0, |w_{1,2}| \neq 0; |v_{1,2}| \neq 0, |w_{1,2}| = 0$, we find that this invariant changes from one to zero and hence infer that a topological transition must occur somewhere in between these two limits. Similarly, Esaki *et al.* argue that Q symmetry acts analogously to chiral symmetry with the caveat

that edge modes must appear gapless in the real plane only, $E_{\text{edge}} = -E^*_{\text{edge}}$ [80]. What bulk invariant is responsible for these edge states?

5.2.2 Non-Hermitian Zak phase

Before specializing to the model (5.4), we introduce the Zak phase for non-Hermitian Hamiltonians. The "complex" Zak phase for band n is defined by

$$Q_n^c = i \int_{-\pi}^{\pi} \left\langle \lambda_k^n \left| \frac{\partial}{\partial k} \right| \psi_k^n \right\rangle dk \tag{5.5}$$

where n labels the band index, $|\psi\rangle, |\lambda\rangle$ are eigenvectors of $\mathcal{H}, \mathcal{H}^\dagger$ respectively (namely the right and left eigenvectors of the Hamiltonian), and the integral is taken over the 1D Brillouin zone [94, 121, 122]. A generalization of Berry's original argument [30] suggests that Q_n^c is the geometrical phase picked up by an adiabatic deformation across the Brillouin zone, which arises fundamentally because the states $|\psi^n\rangle$ no longer form an orthogonal basis while bi-orthonormality constraints are satisfied $\langle \lambda^n | \psi^m \rangle = \delta_{nm}$.

We briefly mention that in the literature, some studies have suggested that the quantization of the "real" Zak phase, defined by

$$Q_n^r = i \int_{-\pi}^{\pi} \left\langle \psi_k^n \left| \frac{\partial}{\partial k} \right| \psi_k^n \right\rangle dk \tag{5.6}$$

where $\langle \psi^n | \psi^n \rangle = 1$, implies a topological classification in non-Hermitian systems [101, 106]. We will find instances where Q_n^r does *not* predict the existence of gapless edge modes, while its complex counterpart does in all situations encountered.

5.2.3 The chiral-SSH model

We now study the chirally-symmetric model, i.e. $u = 0$. The right/left eigenvectors are related via C symmetry by $|\lambda_k^\pm\rangle = \sigma_x |\psi_k^\pm\rangle^*$. Additionally the chiral symmetry relates the positive/negative bands by $|\psi_k^\pm\rangle = \sigma_z |\psi_k^\mp\rangle$. Combining these together

leads to a useful parametrization (fixing the overall gauge)

$$\begin{aligned} \left|\psi_k^{\pm}\right\rangle &= \frac{1}{\sqrt{2\sin\theta_k\cos\theta_k}} \begin{pmatrix} e^{-i\phi_k}\cos\theta_k \\ \pm\sin\theta_k \end{pmatrix} \\ \left|\lambda_k^{\pm}\right\rangle &= \frac{1}{\sqrt{2\sin\theta_k\cos\theta_k}} \begin{pmatrix} e^{-i\phi_k}\sin\theta_k \\ \pm\cos\theta_k \end{pmatrix} \end{aligned} \tag{5.7}$$

where the eigenvectors are normalized to obey the conditions $\left\langle\lambda_k^{\pm}\right|\left.\psi_k^{\pm}\right\rangle = \delta_{++;--}$, $\left\langle\psi_k^{\pm}\right|\left.\psi_k^{\pm}\right\rangle \neq 1, 0$. Substituting (5.7) into the expression for Q^c in (5.5), after some algebra, we find

$$Q_{\pm}^c = \frac{1}{2}\int_{BZ}\dot{\phi}_k dk = \frac{1}{2}\left(\phi_k|_{k=-\pi}^{k=\pi}\right) \tag{5.8}$$

which is clearly quantized to be an integer multiple of π. Note that our parametrization (5.7) is ill-defined in the case when $\theta_k = n\pi/2, n \in \mathbb{Z}$ due to the diverging normalization constant. However θ_k attains such values only when a band gap closes for the chiral system. This is because chiral symmetry precludes a σ_z term in $H(k)$, hence the eigenvectors $|\psi_k\rangle = (1,0)^T, (0,1)^T$ can only occur if one of the off-diagonal elements in the bulk Hamiltonian is zero, and hence at a band crossing. (This point is also known as an exceptional point [123].) Thus the cZak phase is a topological invariant: As long as adiabatic deformations to the Hamiltonian preserve the band gap, the cZak phase will be integer quantized in units of π.

It can be shown [114] that the real Zak phase in a chiral model is not quantized if inversion symmetry is broken. Note that in the cZak phase analysis above there is no reference to inversion symmetry and relationships between right/left eigenvectors arise due to C symmetry alone. Later we will confirm numerically that there are chiral models where inversion symmetry is broken which possess gapless edge modes. Interestingly, recent studies have found that the non-Hermitian 2D Chern number is not sensitive to the combination of right/left eigenvectors used in the expression for the Berry connnection, in contrast to the 1D Zak phase [108].

We now provide a geometrical picture which further justifies our results for the chiral model by projecting eigenvectors onto the Bloch sphere. The most general

2D right eigenvector can be parametrized as

$$|\psi'(\alpha_k, \beta_k)\rangle = \begin{pmatrix} \cos(\beta_k/2) \\ e^{i\alpha_k} \sin(\beta_k/2) \end{pmatrix}. \tag{5.9}$$

For each eigenvector we may calculate the Bloch vector, defined as

$$\mathbf{b}_k = \langle \psi'_k | \boldsymbol{\sigma} | \psi'_k \rangle \tag{5.10}$$

at each k point, where $\boldsymbol{\sigma}$ is the vector of Pauli matrices. α_k, β_k correspond to the azimuthal and polar angles of $\mathbf{b}_k$ respectively.

In Fig. 5.2 we plot the eigenvector evolution on the Bloch sphere across the Brillouin zone for two chiral systems with distinct cZak phases. The north/south poles of the Bloch sphere are attained if $|\psi'(k)\rangle = (1,0)^T, (0,1)^T$ respectively, which (as explained previously) can only occur at a band crossing. If we restrict adiabatic deformations to those which preserve band openings then the poles are not accessible, hence distinct winding numbers are topologically preserved. The topological classification arises due to the result from homotopy theory $\pi_1(S^2/\{n,s\}) = \mathbb{Z}; n = (0,0,1)^T, s = (0,0,-1)^T$, where we map the one-dimensional path across the Brillouin zone onto the surface of the Bloch sphere and observe that distinct winding numbers around the z-axis cannot be smoothly deformed into each other without passing the loop through the north/south pole. The source of the $\mathbb{Z}$ classification in the non-Hermitian model is to be contrasted with the Hermitian SSH model, where Bloch vectors are constrained to lie on the equator, hence $\pi_1(\mathrm{U}(1)) = \mathbb{Z}$. Note that in the presence of a real, staggered potential in the Hermitian SSH, topological classification is lost due to the result $\pi_1(S^2) = 0$, since eigenvectors can reach the poles without closing a band gap.

Bulk-boundary correspondence with Hermiticity-breaking phase: We have found a bulk invariant for the chiral SSH model in the cZak phase. Does a non-trivial invariant correspond to gapless boundary modes for systems with open boundary conditions? In Fig. 5.3 we plot the open spectrum for a system with Hermiticity-breaking phases in the hopping. Crucially, while bulk band gaps may close in the

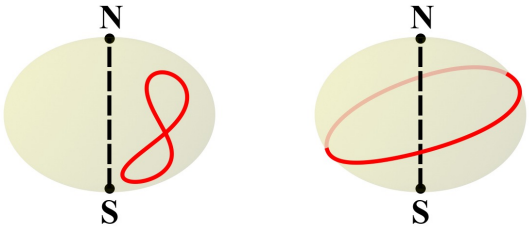

Figure 5.2 The lower-band vectors $\mathbf{b}_k$ (red) on the Bloch sphere in the range $k \in [-\pi, \pi)$ for a chiral model when: $Q^c_\pm = 0$ (left); $Q^c_\pm = \pi$ (right). The north/south axis is dashed in black. Systems with distinct winding number cannot be deformed into each other without passing through the north/south pole (black dots), which can only occur at a band crossing in the chiral model. $\mathbf{b}_k$ are *not* constrained to the equator (in contrast to the Hermitian limit).

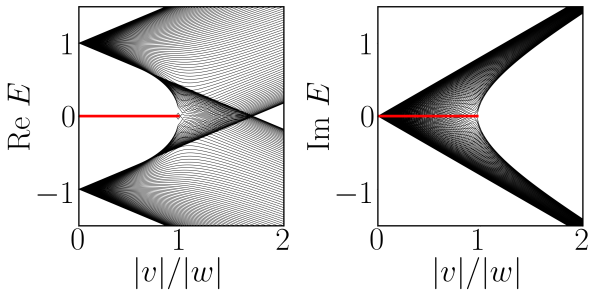

Figure 5.3 Chiral SSH spectrum with parameters: $u = 0, v_1 = \exp(i3\pi/5)\,|v|, v_2 = |v|, w_1 = w_2 = |w|, N = 100$ with open boundary conditions. Edge modes are in red; bulk modes are in black.

real or imaginary plane away from the topological transition point, the only time they close simultaneously is at the transition. The edge mode is protected at zero energy as long as a complex band gap exists in the bulk spectrum. Even though inversion symmetry is broken, we find that a topological transition still persists in agreement with the bulk analysis.

Breakdown of bulk-boundary correspondence: We have observed a "standard" bulk-boundary correspondence in the chiral SSH model if we break the Hermiticity by a phase in the hopping amplitudes, i.e. $|v_1| = |v_2|$, since a non-zero cZak phase corresponds to the presence of edge modes with exactly zero energy. What happens if we break the Hermiticity by an asymmetric hopping amplitude, i.e. $|v_1| \neq |v_2|$?

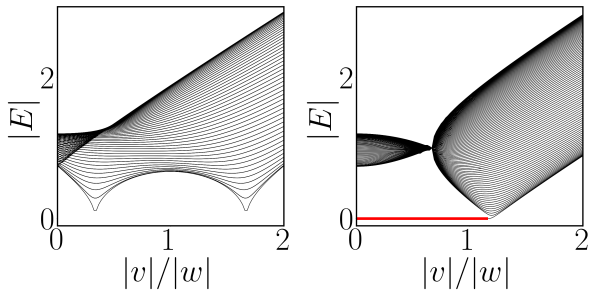

Figure 5.4 Chiral SSH spectrum with parameters: $u = 0, v_1 = |v| - \gamma, v_2 = |v| + \gamma, \gamma = 2/3|w|, w_1 = w_2 = |w|, N = 100$, with periodic boundary conditions (left), and open boundary conditions (right). The spectrum is highly sensitive to edge termination. Edge modes are in red; bulk modes are in black.

It turns out that the spectrum (and eigenvectors) are highly sensitive to boundary conditions: The spectrum looks very different depending on whether we impose periodic vs. open boundary conditions [116, 117], as depicted in Fig. 5.4. This can be intuitively understood because the asymmetric hopping term favors eigenstate localization on one of the two edges of the system. In the case of periodic boundary conditions, there are no edges and hence the spectrum can look very different from the open case.

A new topological invariant called the eigenvalue vorticity characterizes this model [108]. The vorticity between two bands m and n is defined via

$$\nu_{mn} = -\frac{1}{2\pi}\int_0^{2\pi} \frac{\partial}{\partial k}\arg[E_m(k) - E_n(k)]dk. \tag{5.11}$$

A non-zero vorticity of the spectrum implies that two bands swap across the Brillouin zone without becoming degenerate. A non-trivial vorticity for the chiral SSH is given in Fig. 5.5. The only way this vorticity can be smoothly undone is by closing the complex bandgap in the spectrum.

The chiral SSH with asymmetric hopping magnitudes is said to break bulk-boundary correspondence. This is because the vorticity of the bands does *not* predict the presence of gapless boundary modes. Intuitively, this is because the spectrum exhibits high sensitivity to boundary conditions, so a bulk index does not accurately predict behavior at the boundary. A rapidly-growing body of literature

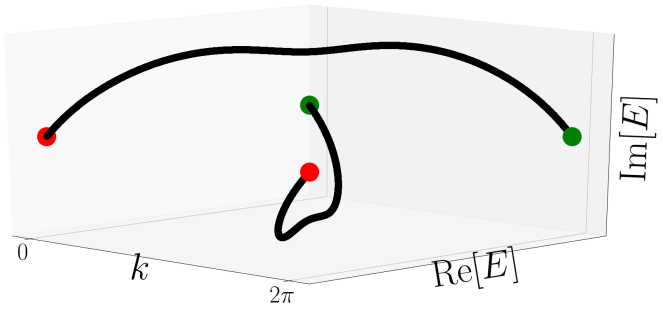

Figure 5.5 Bulk spectrum in the complex plane across the Brillouin zone $k \in [0, 2\pi)$ for parameters $u = 0, v_1 = |v| - \gamma, v_2 = |v| + \gamma, \gamma = 2|w|/3, |v| = 4|w|/5, w_1 = w_2 = |w|$. The red dots represent the same complex energy separated by 2π along the k axis (the green dots do the same). Note that eigenvalues "swap" without a band crossing as k goes from 0 to 2π. This is a non-trivial vorticity. The Bloch eigenvectors are 4π periodic.

[116, 117, 124–127] has been dedicated to address this problem recently, however we will not elaborate further on this.

5.2.4 The PT-SSH model

In the previous section we have argued that if the system has chiral symmetry, then generically the cZak phase will be quantized to an integer value away from a band crossing. It is well-known that a real, staggered potential will destroy quantization in the Hermitian SSH (called the Rice-Mele model) since such a term breaks both chirality and inversion [128, 129]. Physically this is because edge states acquire an energy splitting and hence can be adiabatically removed without closing a band gap. In the PT-symmetric model, edge states are gapless in the real plane but acquire an imaginary energy gap according to $E_{\text{edge}} = \pm iu$. Their real energy is protected to be exactly zero, while their imaginary energy is unconstrained [80]. Liang and Huang [111] derived the expression for the complex Berry connection

$$\left\langle \lambda_k^{\pm} \left| \frac{\partial}{\partial k} \right| \psi_k^{\pm} \right\rangle^{PT} = \frac{1}{2} \left(1 \pm \cos \xi_k\right) \dot{\eta}_k, \tag{5.12}$$

Figure 5.6 One-dimensional phase diagram in v for the PT-symmetric case $v_1 = v_2 = v \in \mathbb{R}, w_1 = w_2 = w \in \mathbb{R}$ at a fixed value of $u, w > 0$. The bulk spectrum is *gapless* (i.e. degenerate) whenever $|v - w| < u$ which implies that the system is critical. The real part of the negative energy band's Zak phase is a gauge-invariant quantity (up to 2π) which is strictly quantized in units of π away from the gapless region and predicts the existence of edge modes with zero real energy.

where $\cos\xi_k = \frac{iu}{\sqrt{\left|v+we^{-ik}\right|^2-u^2}}$, $e^{-i\eta_k} = \frac{v+we^{-ik}}{\left|v+we^{-ik}\right|}$. Upon integration across the Brillouin zone, we find that the real part of the Zak phase is quantized in units of π in the unbroken region ($u < |v - w|$), where the bulk modes are fully real and gapped in the real plane.

The topological phase in the PT-symmetric model is only well defined if the bulk spectrum is gapped in the real plane. In this case edge modes are guaranteed to be protected at zero real energy and the real part of the cZak phase is a quantized invariant which cannot change adiabatically. Once the bulk gap closes in the real plane, the edge modes can be adiabatically removed, and the Hamiltonian is at a critical phase boundary. For the PT model, the bulk spectrum is gapless for a line in parameter space (rather than a critical point), depicted in Fig. 5.6.

Again, we can confirm the bulk-boundary correspondence in this model by plotting the finite chain spectrum. In agreement with the analysis from the previous paragraphs, $\mathrm{Re}[Q_n] = \pi$ corresponds to edge modes with zero real energy but non-zero imaginary energy. These get removed once the bulk spectrum closes and enters a critical region.

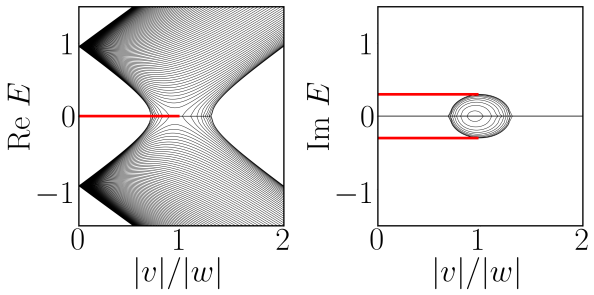

Figure 5.7 PT-symmetric case: $u = 0.3, v_1 = v_2 = |v|, w_1 = w_2 = |w|, N = 100$. Edge modes are in red; bulk modes are in black.

5.3 The bosonic-SSH model

In the previous section we studied non-Hermitian single-particle tight-binding models which are relevant for classical photonics. We now describe the simplest topological transition in a *Hermitian* bosonic Hamiltonian with anomalous terms (i.e. $b^\dagger b^\dagger$), which produces a dynamical instability localized at the edge of the system. This instability arises from the non-Hermiticity of the bosonic BdG equation, which was emphasized in the previous chapter.

Consider the bosonic-SSH Hamiltonian

$$\begin{aligned}\mathcal{H}_b =& v\sum_{i=1}^{N}\left(b_{A,i}^\dagger b_{B,i} + h.c.\right) + w\sum_{i=1}^{N-1}\left(b_{B,i}^\dagger b_{A,i+1} + h.c.\right) \\ &+ \sum_{i=1}^{N}\left[u\left(b_{A,i}b_{A,i} + b_{B,i}b_{B,i}\right) + h.c.\right],\end{aligned} \tag{5.13}$$

where $v, w \in \mathbb{R}$, $u \in \mathbb{C}$, and $b_{A/B,i}$ represents a bosonic operator on lattice site i in sublattice site A/B. This Hamiltonian was proposed by Barnett to describe 1D bosons initially prepared in a higher-energy band then allowed to evolve [95]. Note that the Hamiltonian $\mathcal{H}_b$ is Hermitian, however (due to the arguments in the previous chapter) the matrix which we need to diagonalize in order to obtain the spectrum (H_{BdG}) is non-Hermitian. Within the BL framework, the two relevant symmetries of the model are

$$Q: \qquad H_{\mathrm{BdG}} = \Sigma_z H_{\mathrm{BdG}}^\dagger \Sigma_z \tag{5.14}$$

$$K: \qquad H_{\mathrm{BdG}} = -\Sigma_x H_{\mathrm{BdG}}^* \Sigma_x \tag{5.15}$$

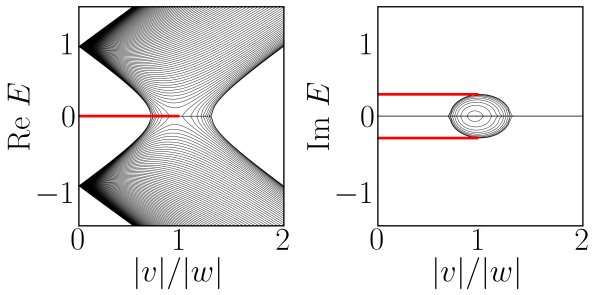

Figure 5.8 Bosonic-SSH post-quench spectrum with $u/w = 0.3, N = 100$. Edge modes are in red; bulk modes are in black.

namely a Q (pseudo-Hermiticity) and a K (particle-hole) symmetry.

The spectrum with open boundary conditions is given in Fig. 5.8 as a function of v/w at a constant value of u. The bulk spectrum is purely real and gapped for parameters $|w - v| > |u|$, however away from this regime some bulk modes start to become unstable and come in complex conjugate pairs. The spectrum appears identical to the PT-SSH model, however it is important to note that each eigenvalue is doubly-degenerate since we plot both quasiparticle and quasihole dispersion. This leads to a subtle difference at the boundary, where each side of the chain hosts two edge modes which can gap each other out by passing through an exceptional point. (See the discussion below.)

Of particular interest are the edge modes (given in red), which have a purely imaginary energy. Each edge hosts two modes: one with energy $+i|u|$ and one with $-i|u|$. Edge modes are particle-hole symmetric: $t_{\text{edge},\pm} \propto \Sigma_x t^*_{\text{edge},\pm}$ which suggests that $E_{\text{edge},\pm} = -E^*_{\text{edge},\pm}$ where $t_{\text{edge},\pm}$ represents an eigenstate of H_{BdG} on an edge with energy $E_{\text{edge},\pm} = \pm i|u|$. Thus because the mode on the edge is its own particle-hole symmetric partner, its energy must be purely imaginary. The stability of these edge modes will be discussed in the next section.

Since we have found that edge modes are particle-hole symmetric, one may wonder whether edge excitations are inherently *nonlocal*, in analogy with Majorana excitations in a Kitaev chain [19]. This interpretation is blurred when discussing the aforementioned model, since the Hamiltonian (5.13) cannot be brought to fully

diagonal form in terms of bosonic quasiparticles when the associated energies are imaginary. This is because complex modes are generically non-normalizable, i.e. $t^{\dagger}_{\text{edge},+}\Sigma_z t_{\text{edge},+} = 0$ [83, 130] which implies that the Bogoliubov transformation cannot be satisfied. There is no constraint for edge excitations to be represented as non-self-adjoint bosonic quasiparticles. While the Hamiltonian is not diagonalizable via bosons, the imaginary eigenvalues of H_{BdG} still have physical meaning: The Heisenberg equations of motion reveal exponential increase in edge site population as a function of time [95].

5.3.1 Robustness of bosonic-SSH edge modes

We return to the question of the robustness of edge modes in the bosonic-SSH model via an adiabatic argument. A few subtleties arise due to the non-Hermiticity of H_{BdG}. We begin by considering a parameter regime where all the bulk modes are fully real and gapped, and we restrict our attention to the left edge for concreteness. First, recall that this edge hosts two right eigenvectors of H_{BdG}: $t_{\pm}$ with associated energies $E_{\pm} = \pm i|u|$ respectively. These modes are particle-hole symmetric, satisfying $t_{\pm} \propto \Sigma_x t^*_{\pm}$ which constrains energies via $E_{\pm} = -E^*_{\pm}$. For Hermitian models, this condition results in the modes having exactly zero energy e.g. Majorana modes in the Kitaev chain [19]; however, in non-Hermitian models this constrains energies according to $\text{Re}[E_{\pm}] = 0$ which implies that the imaginary energy can be non-zero. Crucially, these modes cannot couple to bulk modes as long as there is a gap in real energy and hence edge energies are pinned to be purely imaginary.

Can edge modes with $\text{Re}[E_{\pm}] = 0$ be adiabatically removed without closing the bulk band gap? The answer is no, as long as symmetries are respected *and* H_{BdG} remains diagonalizable during the deformation process. In principle, the two modes with energies $\pm iu$ can become deformed to degeneracy at zero energy by passing through an exceptional point, where the two eigenvectors $t_{\pm}$ coalesce into one[1].

[1]This can be achieved e.g. by adding a staggered real potential $s\sum_{i=1}^{n}\left(b^{\dagger}_{A,i}b_{A,i} - b^{\dagger}_{B,i}b_{B,i}\right)$ to the Hamiltonian (5.13) and tuning from $s = 0$ to $s = 2|u|$.

However H_{BdG} becomes nondiagonalizable at the exceptional point, where edge modes undergo a broken-to-unbroken transition from modes which come in complex conjugate pairs (representing instabilities) to modes with a fully real spectrum (representing stable excitations). This suggests that the diagonalizability of H_{BdG} is important in the definition of a topological phase transition–a restriction which does not arise for Hermitian models and makes the physical protection weaker.

5.4 Summary and outlook

In summary, we have made the analysis from the previous chapter more concrete by explicitly studying extensions of the SSH model which admit modes with complex energies which arise in an open setting. In particular, we have studied the chirally-symmetric, PT-symmetric, and bosonic-SSH models, emphasizing similarities and differences.

We have introduced a chirally-symmetric SSH model which possesses a quantized cZak phase for each band, corresponding to the winding number of the eigenvector across the Bloch sphere. If we break Hermiticity by a phase term in the hopping parameters, the bulk-boundary correspondence is maintained. However, if the eigenvectors swap across the Brillouin zone (by introducing an asymmetric hopping magnitude), then we have numerically found that the bulk-boundary correspondence is destroyed. The PT-symmetric model has edge modes which are gapped in the imaginary plane, but gapless in the real plane. We suggest that a topological phase is well defined whenever the bulk gap is preserved. The real part of the cZak phase is strictly quantized away from a bulk degeneracy point, and serves as a topological index for the transition.

Finally, we studied the simplest example of a quadratic Hamiltonian with bosonic pairing terms which undergoes a topological transition. The spectral properties are remarkably similar to the PT-SSH model: Edge modes are gapped in imaginary energy but have exactly zero real energy. This is because edge modes are protected

by particle-hole symmetry such that $E_{\text{edge}} = -E^*_{\text{edge}}$, and cannot be adiabatically removed as long as the bulk spectrum is gapped in real energy (and the spectral matrix H_{BdG} remains diagonalizable).

Chapter 6

Non-Hermitian Majorana modes protect dynamical degeneracies

Majorana zero modes (MZMs) ensure a robust spectral degeneracy in the topological phase of superconductors (see Sec. 3.1). We demonstrate that non-Hermitian generalizations of MZMs are responsible for a degeneracy in the complex spectrum which describes the dynamics of a continuously-observed many-body state. Specifically, we study measurement-induced non-Hermitian evolution of a two-level transverse field Ising model (TFIM) with the possibility of decaying to a third level by emitting a photon into a cavity. The effective Hamiltonian governing the two-level system in the absence of photonic emission can be mapped to a non-Hermitian topological superconductor (TSC) via a Jordan-Wigner transformation. Using a generalization of particle-hole symmetry, we argue for the stability of MZMs which results in a robust two-fold spectral degeneracy. Increasing the decay rate above a critical amount can close a complex bulk gap, and we uncover the resulting topological phase diagram. Qualitative features of our study generalize to two-dimensional (2D) chiral TSCs. Our work provides a concrete example of a dynamical state which possesses a symmetry-protected topological phase transition which lies beyond the Hermitian Tenfold way.

6.1 Background

In this chapter, we study a non-Hermitian fermionic BdG model which arises due to a Jordan-Wigner transformation from a one-dimensional (1D) spin system coupled to a photonic cavity [131]. We find that MZMs are robust with respect to Hermiticity-breaking terms due to an unconventional particle-hole symmetry (C symmetry, Eq. (4.5)). These modes lead to a robust two-fold degeneracy for all of the many-body eigenstates of the dynamical system.

Specifically, we study a non-Hermitian generalization of the transverse-field Ising model (TFIM) which arises due to continuous observation of its immediate environment. Measurements of a subspace can lead to coherent (pure) non-unitary time evolution in the unmeasured subspace in the absence of a "quantum jump event" due to a positive observation, e.g. detecting a photon [87, 132, 133]. (See Sec. 4.5.2.) We consider a scenario similar to Ref. [87], where a two-level spin system is allowed decay to a third level by emitting a photon into a cavity mode. By continuously checking the cavity mode for the absence of photons, the wavefunction of the three-level system collapses onto the two-level subspace which evolves according to a non-Hermitian effective Hamiltonian (see next section). Projected spin systems have been experimentally probed for a single atom [134, 135], and thermodynamic quantum phase transitions for specific models are predicted [87]. In this study, we focus on the non-Hermitian TFIM from the perspective of topological phases of the Kitaev chain [19], which shares the same spectrum due to a Jordan-Wigner transformation which connects the models. We uncover a topological phase diagram in the strength of the decay parameter, where different phases are distinguished by the presence or absence of two-fold degenerate many-body eigenstates.

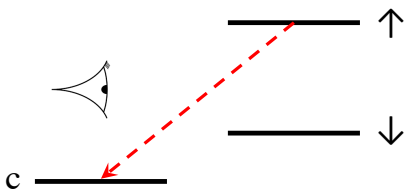

Figure 6.1 Schematic diagram of a dissipative three-level system. The spin up/down sector evolves under coherent, unitary time evolution. An atom can only reach the state $|c\rangle$ by starting in the $|\uparrow\rangle$ state and spontaneously emitting a photon into the cavity. By continuously monitoring the cavity for the absence of photons, part of the Hilbert space is projected and the two-level system undergoes coherent, *non-unitary* time evolution.

6.2 Coherent, non-unitary evolution in a three-level system

Before specializing to the many-body case, we first discuss a single atomic three-level system, with states: $|\uparrow\rangle, |\downarrow\rangle, |c\rangle$. We suppose that the only way for an atom to end up in the state $|c\rangle$ is by starting in the state $|\uparrow\rangle$ and spontaneously emitting a photon into a cavity mode. (See Fig. 6.1.) Otherwise, the two-level system $|\uparrow\rangle, |\downarrow\rangle$ undergoes unitary time evolution according to some Hermitian Hamiltonian H. In the Lindblad formalism outlined in Sec. 4.5.2, the quantum jump operator of this dissipative three-level system is: $L = |c\rangle\langle\uparrow|$. In the stochastic wavefunction approach, we can define an effective Hamiltonian for the dynamics of the two-level system in the absence of a quantum jump event: $H_{\text{eff}} = H - (i\gamma/2)|\uparrow\rangle\langle\uparrow|$, where γ is the spontaneous emission rate. This effective Hamiltonian implies exponential decay in the probability of finding the system in the $|\uparrow\rangle$ state as a function of time, which intuitively makes sense: Conditioning on the fact that no photons are emitted, the probability of finding the spin system in the up state decreases over time. In what follows, we will focus on an N particle generalization of this setup. The many-body steady-state can exhibit a robust degeneracy as a function of the decay rate. We uncover a dynamical

phase diagram for this strongly-interacting, dissipative spin system by mapping the problem to a non-Hermitian topological superconductor.

6.3 The model and symmetries

We now consider the many-body case, with unitary evolution governed by a two-level transverse-field Ising model. Consider the Hamiltonian

$$\mathcal{H} = -J\sum_n \sigma_n^x\sigma_{n+1}^x + u\sum_n \sigma_n^z - i\gamma\sum_n (\sigma_n^z + \mathbb{I})\,, \tag{6.1}$$

where σ_n^i represents the ith Pauli spin operator on the lattice site n of N. The first two terms represent the standard Hermitian TFIM, while the last term represents the non-Hermitian contribution responsible for non-unitary dynamics of the eigenstates: The spin-up state in z may decay to a third level by emitting a photon into the cavity mode. In the absence of photon emission, the two-level system undergoes non-unitary time evolution described above. (In the following analysis, we drop the term proportional to the identity since this does not affect dynamics.) The many-body spectrum can be found exactly by performing a Jordan-Wigner transformation to fermionic degrees of freedom [136]

$$\sigma_j^+ = \exp\left(-i\pi\sum_{k=1}^{j-1} n_k\right)c_j^\dagger \tag{6.2}$$

$$\sigma_j^- = \exp\left(+i\pi\sum_{k=1}^{j-1} n_k\right)c_j \tag{6.3}$$

$$\sigma_j^z = 2c_j^\dagger c_j - 1, \tag{6.4}$$

where $\sigma_j^\pm$ are raising/lowering operators at site j, c_j are complex fermions, and n_j is the fermion number operator. A local raising/lowering operator at site j is represented by the product of a "string operator" to the left of j, followed by creation/annihilation of a fermion at site j.

Upon performing this transformation, the Hamiltonian reads

$$\mathcal{H} = 2\tilde{u}\sum_n c_n^\dagger c_n - J\sum_n \left(c_n^\dagger c_{n+1} + c_n^\dagger c_{n+1}^\dagger + h.c.\right), \tag{6.5}$$

where $\tilde{u} = u - i\gamma$, and c_n represents a complex spinless fermion on site n. The Hamiltonian is rewritten as

$$\mathcal{H} = \frac{1}{2}\begin{pmatrix} \mathbf{c}^\dagger & \mathbf{c} \end{pmatrix} H \begin{pmatrix} \mathbf{c} \\ \mathbf{c}^\dagger \end{pmatrix}, \tag{6.6}$$

where $\mathbf{c} = (c_1, \ldots, c_N)$ and H is a $2N \times 2N$ non-Hermitian matrix.

We discuss the fundamental symmetries of the model. In the language of the Bernard-LeClair scheme, the particle-hole structure of the BdG formalism imposes a C symmetry on the Hamiltonian, but explicitly breaks K symmetry

$$C: \qquad H = -\Sigma_x H^T \Sigma_x \tag{6.7}$$

$$K: \qquad H \neq -\Sigma_x H^* \Sigma_x, \tag{6.8}$$

where $\Sigma_x = \sigma_x \otimes \mathbb{I}_N$. We emphasize that in the Hermitian limit, $H^* = H^T$ such that the C and K symmetries are redundant. Once non-Hermitian terms are added, K symmetry is violated while C remains. In contrast to previous studies [137–139], the model studied above does not possess PT symmetry and hence energies will generically be complex. It also does not possess time-reversal symmetry due to the decaying nature of the eigenstates. Nevertheless, we will demonstrate that only C symmetry is needed to protect Majorana zero modes in 1D and 2D.

To diagonalize the Hamiltonian, we make a transformation to fermionic quasiparticles

$$\begin{pmatrix} \mathbf{q} & \mathbf{p}^\dagger \end{pmatrix} = \begin{pmatrix} \mathbf{c}^\dagger & \mathbf{c} \end{pmatrix} V, \qquad \begin{pmatrix} \mathbf{p}^\dagger \\ \mathbf{q} \end{pmatrix} = V^{-1} \begin{pmatrix} \mathbf{c} \\ \mathbf{c}^\dagger \end{pmatrix}. \tag{6.9}$$

The two flavors of quasiparticles $q, p^\dagger$ arise due to the right and left eigenvectors of non-Hermitian matrices [137]. The C symmetry of the BdG Hamiltonian imposes a structure on the transformation matrix

$$V = \Sigma_x \left(V^{-1}\right)^T \Sigma_x. \tag{6.10}$$

Remarkably, this expression guarantees that quasiparticles obey generalized fermionic statistics

$$\{p_i^\dagger, q_j\} = \delta_{i,j}, \ \{p_i^\dagger, p_j^\dagger\} = \{q_i^\dagger, q_j^\dagger\} = 0. \tag{6.11}$$

The diagonalized second-quantized Hamiltonian reads

$$\mathcal{H} = \frac{1}{2}\begin{pmatrix} \mathbf{q} & \mathbf{p}^\dagger \end{pmatrix} \Lambda \begin{pmatrix} \mathbf{p}^\dagger \\ \mathbf{q} \end{pmatrix}, \tag{6.12}$$

where $\Lambda = \mathrm{Diag}[-E_1, \ldots, -E_N, E_1, \ldots, E_N]$ is a diagonal matrix whose entries correspond to the energies of the system, and $\mathrm{Re}[E_i] > 0$. The quasiparticle vacuum state is defined as: $q_i \left|\mathrm{vac}\right\rangle = 0$, and an excited state with energy E_i is $p_i^\dagger \left|\mathrm{vac}\right\rangle$.

6.4 Stability of Majorana modes

Before calculating the spectrum, we generalize the stability of Majorana zero modes to include robustness against non-Hermitian terms in the Hamiltonian. In a 1D Hermitian TSC (e.g. the Kitaev chain), the MZM is protected at zero energy due to its particle-hole symmetry

$$\psi_0 \propto \Sigma_x \psi_0^* \implies E_0 = 0, \tag{6.13}$$

where $H\psi_0 = 0$. Any term entering the Hamiltonian which preserves the bandgap cannot perturb the MZM away from zero energy.

In the non-Hermitian case, each eigenvalue E has an associated right and left eigenvector, defined as

$$H\psi = E\psi \tag{6.14}$$

$$H^\dagger \lambda = E^* \lambda. \tag{6.15}$$

The non-Hermitian MZM satisfies the condition

$$\psi_0 \propto \Sigma_x \lambda_0^* \implies E_0 = 0. \tag{6.16}$$

We find that the C symmetry protects the MZM at zero energy in direct analogy with the Hermitian case. This ensures a two-fold spectral degeneracy in the many-body spectrum of the dynamical system. This topological model clearly falls beyond the scope of the Tenfold way. Our analysis generalizes the protection of MZMs in a TSC with respect to Hermiticity-breaking terms in the Hamiltonian.

6.5 Many-body spectrum

The spectrum of the system for weak decay is given in Fig. 6.2. We find that the energy of the MZM remains unchanged upon inclusion of decay, in agreement with the analysis from the previous section. The same cannot be said about bulk modes, all of which acquire a non-zero imaginary component to their energy. Interestingly, we find that some quasiparticles get amplified while others decay. (In order to properly calculate observables we must renormalize the wavefunction after time evolving [87].) We can understand this behavior by examining the composition of the quasiparticles in terms of electrons and holes. Quasiparticles which are mostly composed of electrons ($c^\dagger$ terms) acquire a negative imaginary energy indicating decay, while modes composed of holes (c terms) acquire a positive imaginary energy indicating growth. Intuitively this agrees with the idea that electronic dissipation leads to the proliferation of holes. MZMs are equally composed of electrons and holes, hence their imaginary component is zero.

What does a complex energy spectrum imply for the dynamics of the system? An arbitrary initial state can be rewritten as a superposition of quasiparticles $p_i^\dagger$ acting on the vacuum. Upon evolving the state in time by $\exp(-i\mathcal{H}t)$, the terms with the most hole-like quasiparticles will start to dominate the wavefunction, since these are the modes which get amplified in time. The eigenstate with the largest imaginary energy will dominate the steady-state behavior. Each many-body eigenstate has a two-fold degeneracy due to the MZMs which couple to form a non-local zero mode.

6.6 Dissipative phase diagram

We have seen that the presence of weak decay (small γ) leaves the Majorana mode pinned at zero energy while bulk modes generically pick up a complex dispersion. As the decay rate is further increased, it is possible to induce a topological phase transition via closing a band gap. In Fig. 6.3 we show a particular trajectory in parameter space. The lack of MZMs at large decay rates indicates that the many-

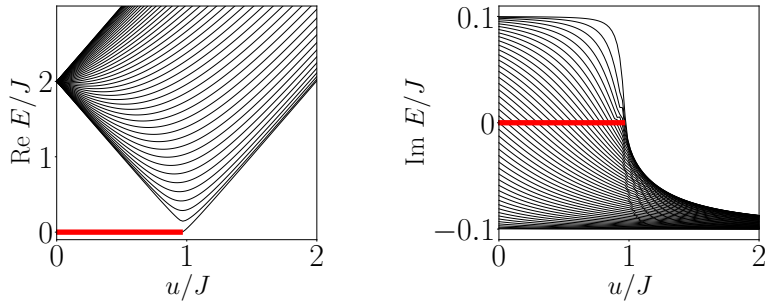

Figure 6.2 Spectrum of the 1D non-Hermitian Kitaev chain, $\gamma/J = 0.1$. The TFIM (6.1) shares the same spectrum. MZMs (red) exist on opposite ends of the spectrum and couple to form a quasiparticle zero-mode. Bulk modes (black) are generically complex. Positive imaginary modes represent amplifying hole bands, while negative modes represent decaying electronic bands.

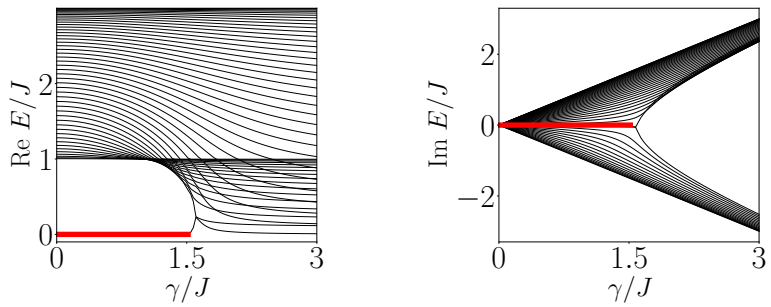

Figure 6.3 Increasing the decay rate (γ) induces a topological phase transition in the 1D non-Hermitian Kitaev chain, $u/J = 0.5$. MZMs (red) exist in the limit of weak decay but can be removed by closing a band gap in both the real and imaginary plane. MZMs do not exist at high decay rates, signaling a lack of eigenstate degeneracy.

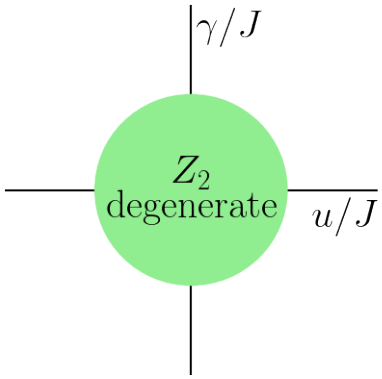

Figure 6.4 Phase diagram of the Ising model with coupling J, real transverse field u, and imaginary transverse field γ. Within the green unit circle, the many-body spectrum is two-fold degenerate (due to MZMs in the fermionic model, and symmetry-broken phases in the spin model).

body eigenspectrum is no longer two-fold degenerate.

In order to uncover the topological phase boundary, it is easiest to examine the Bloch Hamiltonian by transforming to momentum coordinates k. The bulk dispersion is found to be

$$E_k = \pm 2\sqrt{((u - i\gamma) - J\cos k)^2 + J^2 \sin^2 k}. \tag{6.17}$$

We easily identify the band closing points which occur at the critical values: $u_c^2 + \gamma_c^2 = J_c^2$. This expression agrees with our intuition: If we consider the non-Hermitian TFIM in Eq. (6.1), this phase boundary corresponds to the statement that spontaneous symmetry breaking will occur whenever the magnitude of the strength of the transverse field is less than that of the nearest-neighbor interaction. The phase diagram is given in Fig. 6.4. Indeed our analysis suggests that the $\mathbb{Z}_2$ eigenstate degeneracy of the symmetry-broken TFIM persists in the presence of complex transverse fields.

6.7 2D topological superconductor

We demonstrate that the qualitative results from our study generalize to two-dimensional models. Consider the "chiral" TSC in 2D in the presence of uniform electronic loss

$$\begin{aligned}\mathcal{H}_{\text{2D}} = &\sum_{m,n} -t\left(c^\dagger_{m+1,n}c_{m,n} + c^\dagger_{m,n+1}c_{m,n} + h.c.\right)\\ &+ \left(\Delta c^\dagger_{m+1,n}c^\dagger_{m,n} + h.c.\right) + \left(i\Delta c^\dagger_{m,n+1}c^\dagger_{m,n} + h.c.\right)\\ &- (\mu + i\gamma - 4t)\, c^\dagger_{m,n}c_{m,n}\end{aligned} \tag{6.18}$$

where we assume a square lattice geometry and $c_{m,n}$ annihilates a spinless fermion on lattice site (m, n) of an $N \times N$ lattice [140, 141]. The terms represent hopping t, pairing Δ, and the chemical potential μ. To observe edge modes we impose periodic boundary conditions in the y direction while maintaining a finite slab in x. We rewrite operators in terms of their Fourier transform:

$$c_{m,n} = \frac{1}{\sqrt{N}}\sum_{k_y} e^{ik_y n}c_{m,k_y}. \tag{6.19}$$

The Hamiltonian takes the form:

$$\mathcal{H}_{\text{2D}} = \sum_{k_y\in(0,\pi)} \mathbf{c}^\dagger_{k_y} H(k_y)\mathbf{c}_{k_y} \tag{6.20}$$

where $\mathbf{c}_k = (c_{m=1,k_y}\ldots, c^\dagger_{m=1,-k_y},\ldots)^T$. The spectrum is found by diagonalizing H_{k_y} and is given in Fig. 6.5 for a weakly decaying model (henceforth, we use the scalar k to represent k_y). Notice that a single edge mode is localized on each side of the chain with opposite group velocity which results in a net chirality.

The MZM is protected at the high-symmetry point in the Brillouin zone due to particle-hole symmetry. The Bloch Hamiltonian satisfies

$$H(k) = -\Sigma_x H^T(-k)\Sigma_x. \tag{6.21}$$

Non-Hermitian Majorana modes at a high-symmetry point in the Brillouin zone (e.g. $k = 0$), are related via

$$\psi_{\text{edge}}(k = 0) \propto \Sigma_x \lambda^*_{\text{edge}}(k = 0). \tag{6.22}$$

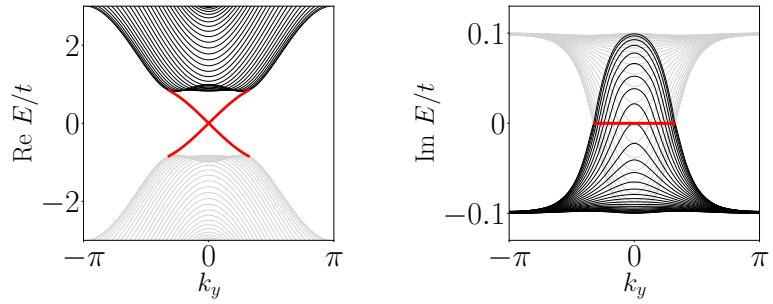

Figure 6.5 Semi-periodic spectrum in k_y for the weakly-dissipative Hamiltonian given in Eq. (6.18) with parameters: $\Delta/t = 0.5, \mu/t = 1.0, \gamma/t = 0.1$. Edge modes (red) retain their fully real dispersion, while bulk modes (black) are complex. The band crossing occurs at zero energy when $k = 0$ due to MZMs which arise on opposite edges of the system. This is in agreement with symmetry considerations. (Hole bands are shaded in grey.)

This again suggests that $E(k = 0) = 0$ due to C symmetry, in agreement with the numerics given in Fig. 6.5.

6.8 Summary and outlook

In this chapter, we have studied the coherent, non-unitary dynamics of a three-level system coupled to a photonic cavity mode. In the absence of photonic emission into the cavity, the two-level subspace evolves according to an Ising model with *complex* transverse field. We solved for the spectrum exactly by mapping the system to a dissipative topological superconductor via a Jordan-Wigner transformation. The model possesses no symmetries other than its inherent particle-hole structure—a C symmetry in the Bernard-LeClair classification. Nevertheless, Majorana zero modes exist at the edge of the sample, and we argued for their stability in the presence of non-Hermitian terms (in both 1D and 2D). We uncovered a topological phase diagram in the decay rate. In the language of the spin model, we demonstrated that symmetry-breaking phases are expected to occur in complex extensions of the transverse field, so long as the magnitude of the field is less than that of the interac-

tion. Our work extends the formalism of ground state phases of electrons to apply to dynamical phases of continuously-monitored many-body systems in a dissipative environment. A clear next step is to ask whether a topologically degenerate many-body steady-state can exist in the *presence* of decoherent quantum jump events. This will be the direction of future studies.

Chapter 7

Conclusions and outlook

In the remaining few pages of this thesis, we summarize the main achievements of each chapter and emphasize exciting new research directions. We separate our discussion into three parts, corresponding to the three main research themes.

7.1 Intertwined superfluidity and density wave order

In Ch. 2 we studied a 2D Bose Hamiltonian whose condensate degeneracy manifold was parameterized by non-Abelian symmetry generators due to spatial degrees of freedom. We considered a setup where an external field is applied to a weakly-interacting Bose gas; the particles condense in the second-lowest energy band and the finite-range interaction profile is restricted to satisfy a smoothness criterion. This led to a coherent state degeneracy manifold which is isomorphic to S^5. The non-Abelian manifold immediately led us to conclude that real-space vortices in the phase are unstable, and that anomalous Goldstone modes are expected. Both of these predictions were confirmed numerically. The lack of topological vortices led to the absence of superfluidity at non-zero temperature, which was corroborated by a microscopic calculation within the Bogoliubov approximation.

Can this non-Abelian condensate be a candidate for a "supersolid" phase that

spontaneously breaks both translational and global gauge symmetries? The condensation at non-zero momenta may be induced by certain two-body interaction potentials with negative Fourier components at the ordering wavevector. Such condensation may occur even in the absence of an applied field by creating a roton instability [142, 143]. Such a system is generically an Abelian condensate with decoupled Bogoliubov and phonon modes. (In the context of our S^5 manifold, the interactions creating the roton instability will generically determine all the relative weights and phases of the amplitudes c_i, other than the ones responsible for these U(1) modes.) Therefore, one expects to see a BKT transition in contrast to [36]. Nevertheless, we can show that non-Abelian condensates can be local minima in mean-field theory for special fine-tuned Hamiltonians. These states, however, appear to be dynamically unstable in general, as evidenced by imaginary eigenvalues in their Bogoliubov spectra. A notable exception arises if the single-particle spectrum deviates from the typical quadratic kinetic energy dispersion (e.g. due to band structure, or internal degrees of freedom) where we have found a condensate with SU(2) symmetry in addition to the U(1) translational symmetries. Future work should aim to uncover the properties of such a "non-Abelian supersolid."

7.2 Disordered topological superconductors

The Kitaev chain superconductor has attracted much attention since it possesses topological zero-modes which are responsible for nonlocally degenerate ground states which can represent a qubit immune to several noise channels. In Ch. 3 we uncovered phase diagrams for topological superconductors in the presence of strong disorder. We motivated the idea that local zero-modes in the presence of disorder may represent a new paradigm in the quest for a stable qubit, and subsequently studied a minimal model which realizes such a setup. For certain parameter regimes, our model hosts two Majorana zero modes per side of the chain which can pair up to form a *local* zero energy excitation. The corresponding disordered phase diagram

was found by two independent methods: (1) by considering the normalization of the disordered edge modes, and (2) by examining the degeneracy of the entanglement spectrum [64]. Both independent methods led to the same phase boundaries. We found that disorder can both promote and demote a topological index. Strong disorder generally drives a 2→1→0 MZM transition. In addition, we have uncovered regions where the addition of disorder can induce local zero-modes. This is a generalization of the "topological Anderson insulator" to models with a $\mathbb{Z}$ classification [69]. From the perspective of quantum information, our model can be mapped to a cluster-spin Ising model (via a Jordan-Wigner transformation) and consequently the phase diagram in Fig. 3.4 provides a starting point to investigate the coherence properties of topological edge spin qubits in the presence of disorder [62].

Does the global topology of a ground state wavefunction manifest itself in local properties within the bulk of a sample? Topological phases do not possess a *local* order parameter (almost by definition), hence naively one would expect that local observables do not carry information about global topology. However, recasting the expression for the Chern number in a real space basis leads to a quantity known as the Chern marker, which has been shown to be a locally-quantized object in the bulk of a finite sample [144, 145]. In light of recent progress in this field, it is natural to ask whether a disorder-averaged real-space marker can accurately predict the phase boundaries derived in this work. If so, this would add to the toolkit of methods which are useful for describing topological phases in a strongly disordered system.

7.3 Topology in non-Hermitian systems

In Chs. 4, 5, and 6 we generalized ideas from topological band theory to include complex band structures which belong to open systems out of equilibrium. Chapter 4 introduced the fundamental framework of "non-Hermitian symmetry-protected topological phases" by highlighting important symmetries and describing physical motivations. We suggested that time-reversal and particle-hole symmetry (both of

which involve complex conjugation of a Hamiltonian matrix) can come in two flavors in non-Hermitian models since $H^* \neq H^T$ if $H \neq H^\dagger$. This naturally leads to an enlarged set of non-Hermitian symmetry classes. These were dubbed the Bernard-LeClair classes which generalize the canonical Altland-Zirnbauer ones in the absence of Hermiticity. Very recent studies [77, 78] have used the BL classes as a basis to generalize symmetry-protected topological phases to non-Hermitian models, called the 38-fold way. The rest of Ch. 4 was dedicated to describing where to find these symmetries in nature, and explicit models were studied in Chs. 5 and 6.

To date, most of the experimental motivations in the field of "non-Hermitian topology" arise from describing topological modes of light propagating through a dissipative medium. The active field of topological photonics originally began with speculations by Haldane and Raghu [93]: Is topological band theory an inherently quantum mechanical property, or is it a general phenomenon which applies to classical waves? The answer appears to be the latter. If dissipation due to an underlying medium is taken into account, we have argued that the evolution of a wavefront can be mapped to a non-Hermitian Schrödinger equation (in the paraxial limit). Modes of light can be topologically protected to lie in the *complex* gap of a bulk band structure. In Ch. 5 we have given two examples of 1D tight-binding models which host symmetry-protected modes at the boundary. Depending on the symmetries of the model, edge modes can either be fully stable (if $E = 0$) or only gapless in the frequency domain (if $\mathrm{Re}[E] = 0$).

The experimental realization of a 2D topological photonic model is well known to be challenging. This is because it is generically difficult to break time-reversal symmetry (required for the $\mathbb{Z}$-classified Haldane state) or engineer fermionic time-reversal symmetry (required for the $\mathbb{Z}_2$-classified quantum spin Hall state). The 38-fold way tells us that by taking into account non-Hermitian symmetries, it is possible to engineer dissipation-induced topological phases which have no equilibrium counterpart. The enlarged space of non-Hermitian topological models provides more opportunity to hunt for topological behavior in open systems vs. their closed

counterparts. Constructing such models from first principles is an exciting new research avenue.

The dynamical matrix which time-evolves bosonic excitations around a condensate is a non-Hermitian one, which is naturally sorted into one of the Bernard-LeClair classes. More specifically, we showed that the bosonic Bogoliubov-de Gennes equation (the eigenvalue problem for the bosonic spectrum) naturally possesses a particle-hole symmetry (K) and "pseudo-Hermiticity" (Q) in the BL classification. Thus we have suggested that bosonic band structures fall outside of the Tenfold way, and instead are topologically classified via the non-Hermitian 38-fold way [82]. While this symmetry analysis was generic, in Ch. 5 we provided a concrete example where the non-Hermiticity plays an important role: Adding Hermitian bosonic pairing terms to a standard SSH model leads to instabilities which are localized at the edges of the sample [95]. This is called a "topological edge instability" which cannot occur in fermionic systems and has direct analogs in higher dimensional models [96, 97].

Bosonic BdG models are used to describe a wide variety of physical systems, including: (1) the excitation spectrum of atomic condensates, (2) quantum photonic band structures in the presence of nonlinear effects, (3) spin-wave excitations in magnets after Holstein-Primakoff transformation. The concept of a topological edge instability has already led to several proposals which may be useful for quantum device design and experimental diagnostics. Driving a medium with a pump source can cause unbounded growth of certain photonic modes due to nonlinear effects, e.g. "parametric down conversion." It has been suggested that topological instabilities can be exploited to construct unidirectional amplifiers which are resistant to backscattering—an important resource for quantum signal processing [97]. Additionally, recent work has proposed that the bosonic instability can be used as a tool to observe the topological edge modes in the spin-excitation spectrum of magnets: Driving a magnonic insulator with an electromagnetic field can lead to a spin current amplification which is confined to the boundary of the sample [146]. This would provide a simple smoking-gun signature of magnetic systems which are suspected to

possess topological edge modes above the low-energy sector.

An important direction for future work involves going beyond Bogoliubov mean-field theory. While non-unitary, exponential growth of fluctuations is a good approximation of dynamics at short time scales, the depletion of the condensate cannot continue indefinitely and hence the bosonic particles must reach a new equilibrium. Does this steady state carry information about the topological instability via a large population at the boundary? Or is this a transient effect which disappears in the long-time limit? The fate of this boundary population needs to be addressed in future work.

Separate from these bosonic instabilities, we also raised the tantalizing possibility of a symmetry-protected "topological steady state" which generalizes the notion of a topological ground state to non-equilibrium systems in an open environment. Systems interacting with a larger environment can exhibit non-unitary time evolution due to particles which can spontaneously appear from or disappear into a larger bath. Generic driven-dissipative systems are described by a many-body density matrix which tends to a unique non-thermal steady state in the long-time limit. Formally this is found by solving for the spectrum of a Lindblad master equation, which is generically complex, representing modes which decay as a function of time; the steady state is the one which maintains its amplitude. This complex spectrum is found from the eigenvalues of a non-Hermitian matrix, and it is therefore natural to ask whether the formalism of non-Hermitian topology can be useful in constructing steady states which are topologically degenerate.

In Ch. 6 we presented a simple setup which realizes two robustly-degenerate steady states: A two-level transverse-field Ising model which could decay to a third level was studied from the perspective of a Kitaev chain with a complex onsite potential. The latter shares the same spectrum due to a Jordan-Wigner transformation which connects the two models. We found that non-Hermitian generalizations of Majorana zero modes are responsible for a two-fold degeneracy of the steady state in the absence of photonic emission for certain parameter regimes. Using the fermionic

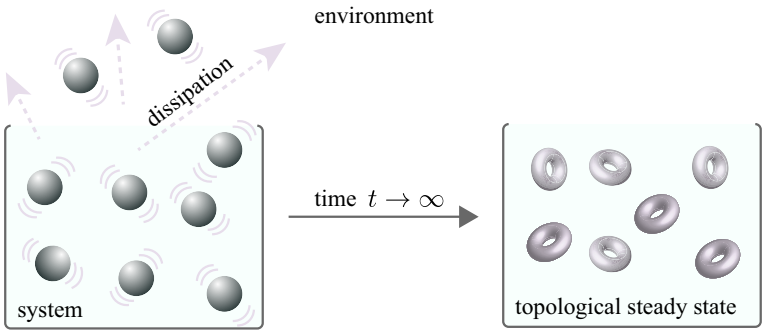

Figure 7.1 An arbitrary initial state interacting with an environment will tend to a topologically-degenerate steady state in the long-time limit.

mapping, we were able to draw an exact phase boundary between regions where the steady state is unique vs. $\mathbb{Z}_2$ degenerate. This provides a simple example of a symmetry-protected topological degeneracy in the steady state of a dissipative, dynamical model.

A natural extension of Ch. 6 is to ask whether a steady state can be topologically degenerate in the *presence* of quantum jump events which decohere the system. (See Fig. 7.1.) We briefly outline an approach which appears promising. An $N \times N$ density matrix can be viewed as a N^2 vector by simply rewriting the matrix elements. If the unitary time evolution of the Lindbladian is quadratic in Fermi operators, and the jump operators are linear, then the Lindblad superoperator can always be expressed as a non-Hermitian, quadratic Fermi operator acting on the space of vectorized density matrices [85]. The complex spectrum of the Lindbladian is then found via the eigenvalues of a non-Hermitian BdG superconductor. In light of this, we can once again ask whether it is possible to engineer Majorana zero modes which connect degenerate steady states: $\gamma_{\text{maj.}} |\text{SS}_1\rangle = |\text{SS}_2\rangle$, where $|\text{SS}_{1/2}\rangle$ represent vectorized steady state density matrices which are connected by a gapless Majorana mode $\gamma_{\text{maj.}}$. This can be viewed as a dissipative analog of a Kitaev chain, which could serve as a new platform for quantum computation: Qubits can be represented as one of two topologically-degenerate steady states, where decoherence channels are already taken into account.

The field of non-Hermitian topological band theory has received much theoretical

and experimental attention in recent years. While much of this formalism has been successfully used to predict the existence of robust photonic edge modes in classical light-matter systems, this thesis suggests that non-Hermitian topology is very much relevant for open, many-body *quantum* models. Future research efforts should work towards the observation of topologically universal behavior in non-equilibrium quantum systems with many degrees of freedom.

Bibliography

[1] P. W. Anderson, *Basic notions of condensed matter physics* (Addison-Wesley, 1997).

[2] L. D. Landau and E. M. Lifshitz, *Statistical physics* (London Pergamon Press, 1958).

[3] K. G. Wilson, Rev. Mod. Phys. **47**, 773 (1975).

[4] M. Chester, L. C. Yang, and J. B. Stephens, Phys. Rev. Lett. **29**, 211 (1972).

[5] N. D. Mermin and H. Wagner, Phys. Rev. Lett. **17**, 1133 (1966).

[6] P. C. Hohenberg, Phys. Rev. **158**, 383 (1967).

[7] J. M. Kosterlitz and D. J. Thouless, J. Phys. C: Solid State Physics **6**, 1181 (1973).

[8] V. L. Berezinskii, Sov. Phys. JETP **32**, 493 (1971).

[9] K. v. Klitzing, G. Dorda, and M. Pepper, Phys. Rev. Lett. **45**, 494 (1980).

[10] D. J. Thouless, M. Kohmoto, M. P. Nightingale, and M. den Nijs, Phys. Rev. Lett. **49**, 405 (1982).

[11] F. D. M. Haldane, Phys. Rev. Lett. **61**, 2015 (1988).

[12] C. L. Kane and E. J. Mele, Phys. Rev. Lett. **95**, 226801 (2005).

[13] B. A. Bernevig, T. L. Hughes, and S.-C. Zhang, Science **314**, 1757 (2006).

[14] M. König, S. Wiedmann, C. Brüne, A. Roth, H. Buhmann, L. W. Molenkamp, X.-L. Qi, and S.-C. Zhang, Science **318**, 766 (2007).

[15] X.-L. Qi and S.-C. Zhang, Rev. Mod. Phys. **83**, 1057 (2011).

[16] M. Z. Hasan and C. L. Kane, Rev. Mod. Phys. **82**, 3045 (2010).

[17] S. Ryu, A. P. Schnyder, A. Furusaki, and A. W. W. Ludwig, New J. Phys. **12**, 065010 (2010).

[18] J. Goldstone, Il Nuovo Cimento **19**, 154 (1961).

[19] A. Y. Kitaev, Phys.-Usp. **44**, 131 (2001).

[20] J. Alicea, Rep. Prog. Phys. **75**, 076501 (2012).

[21] K. von Klitzing, Rev. Mod. Phys. **58**, 519 (1986).

[22] X.-G. Wen, *Quantum field theory of many-body systems: from the origin of sound to an origin of light and electrons* (Oxford University Press, 2004).

[23] M. Kardar, *Statistical Physics of Fields* (Cambridge University Press, 2007).

[24] O. Penrose and L. Onsager, Phys. Rev. **104**, 576 (1956).

[25] J. M. Kosterlitz and D. J. Thouless, J. Phys. C: Solid State Physics **5**, L124 (1972).

[26] J. F. Annett, *Superconductivity, superfluids and condensates*, Vol. 5 (Oxford University Press, 2004).

[27] L. Pitaevskii and S. Stringari, *Bose-Einstein condensation and superfluidity*, Vol. 164 (Oxford University Press, 2016).

[28] P. Nozieres and D. Pines, *Theory of Quantum Liquids Volume II: Superfluid Bose Liquids.*, Advanced Book Classics (Westview Press, 1994).

[29] W. P. Su, J. R. Schrieffer, and A. J. Heeger, Phys. Rev. Lett. **42**, 1698 (1979).

[30] M. V. Berry, J. Phys. A: Math. Gen. **18**, 15 (1985).

[31] J. Zak, Phys. Rev. Lett. **62**, 2747 (1989).

[32] A. Altland and M. R. Zirnbauer, Phys. Rev. B **55**, 1142 (1997).

[33] F. J. Dyson, J. Math. Phys. **3**, 1199 (1962).

[34] A. Kitaev, AIP Conf. Proc. **1134**, 22 (2009).

[35] S. Ryu and Y. Hatsugai, Phys. Rev. Lett. **89**, 077002 (2002).

[36] J. Nyéki, A. Phillis, A. Ho, D. Lee, P. Coleman, J. Parpia, B. Cowan, and J. Saunders, Nat. Phys. **13**, 455 (2017).

[37] P. Corboz, M. Boninsegni, L. Pollet, and M. Troyer, Phys. Rev. B **78**, 245414 (2008).

[38] W. V. Liu and C. Wu, Phys. Rev. A **74**, 013607 (2006).

[39] C. Wu, Mod. Phys. Lett. B **23**, 1 (2009).

[40] H. Watanabe and T. Brauner, Phys. Rev. D **84**, 125013 (2011).

[41] H. Watanabe and T. Brauner, Phys. Rev. D **85**, 085010 (2012).

[42] H. Watanabe and H. Murayama, Phys. Rev. Lett. **108**, 251602 (2012).

[43] H. Watanabe and H. Murayama, Phys. Rev. Lett. **110**, 181601 (2013).

[44] D. A. Takahashi and M. Nitta, Ann. Phys. **354**, 101 (2015).

[45] M. Nitta and D. A. Takahashi, Phys. Rev. D **91**, 025018 (2015).

[46] S. Lieu, A. F. Ho, D. K. K. Lee, and P. Coleman, Phys. Rev. B **99**, 014504 (2019).

[47] S. Gopalakrishnan, I. Martin, and E. A. Demler, Phys. Rev. Lett. **111**, 185304 (2013).

[48] R. Barnett, S. Powell, T. Graß, M. Lewenstein, and S. Das Sarma, Phys. Rev. A **85**, 023615 (2012).

[49] U. R. Fischer, Phys. Rev. A **73**, 031602 (2006).

[50] L. Chomaz, R. M. W. van Bijnen, D. Petter, G. Faraoni, S. Baier, J. H. Becher, M. J. Mark, F. Wächtler, L. Santos, and F. Ferlaino, Nat. Phys. **14**, 442 (2018).

[51] P. W. Anderson, Phys. Rev. **109**, 1492 (1958).

[52] J. Li, R.-L. Chu, J. K. Jain, and S.-Q. Shen, Phys. Rev. Lett. **102**, 136806 (2009).

[53] X. Cai, L.-J. Lang, S. Chen, and Y. Wang, Phys. Rev. Lett. **110**, 176403 (2013).

[54] A. Altland, D. Bagrets, L. Fritz, A. Kamenev, and H. Schmiedt, Phys. Rev. Lett. **112**, 206602 (2014).

[55] E. J. Meier, F. A. An, A. Dauphin, M. Maffei, P. Massignan, T. L. Hughes, and B. Gadway, Science **362**, 929 (2018).

[56] V. Mourik, K. Zuo, S. M. Frolov, S. R. Plissard, E. P. A. M. Bakkers, and L. P. Kouwenhoven, Science **336**, 1003 (2012).

[57] A. Das, Y. Ronen, Y. Most, Y. Oreg, M. Heiblum, and H. Shtrikman, Nat. Phys. **8**, 887 (2012).

[58] M. T. Deng, S. Vaitiekenas, E. B. Hansen, J. Danon, M. Leijnse, K. Flensberg, J. Nygård, P. Krogstrup, and C. M. Marcus, Science **354**, 1557 (2016).

[59] E. Prada, R. Aguado, and P. San-Jose, Phys. Rev. B **96**, 085418 (2017).

[60] S. Jeon, Y. Xie, J. Li, Z. Wang, B. A. Bernevig, and A. Yazdani, Science **358**, 772 (2017).

[61] R. Nandkishore and D. A. Huse, Annu. Rev. Condens. Matter Phys. **6**, 15 (2015).

[62] Y. Bahri, R. Vosk, E. Altman, and A. Vishwanath, Nat. Commun. **6**, 7341 (2015).

[63] D. V. Else, P. Fendley, J. Kemp, and C. Nayak, Phys. Rev. X **7**, 041062 (2017).

[64] S. Lieu, D. K. K. Lee, and J. Knolle, Phys. Rev. B **98**, 134507 (2018).

[65] Y. Niu, S. B. Chung, C.-H. Hsu, I. Mandal, S. Raghu, and S. Chakravarty, Phys. Rev. B **85**, 035110 (2012).

[66] B. Kramer and A. MacKinnon, Rep. Prog. Phys. **56**, 1469 (1993).

[67] A. Crisanti, G. Paladin, and A. Vulpiani, *Products of random matrices in statistical physics* (Springer-Vlg, 1993).

[68] M. Castanier and C. Pierre, J. Sound Vib. **183**, 493 (1995).

[69] H. Li and F. D. M. Haldane, Phys. Rev. Lett. **101**, 010504 (2008).

[70] A. M. Turner, F. Pollmann, and E. Berg, Phys. Rev. B **83**, 075102 (2011).

[71] D. J. Yates and A. Mitra, Phys. Rev. B **96**, 115108 (2017).

[72] N. M. Gergs, L. Fritz, and D. Schuricht, Phys. Rev. B **93**, 075129 (2016).

[73] I. Peschel and V. Eisler, J. Phys. A: Math. Theor. **42**, 504003 (2009).

[74] F. J. Gómez-Ruiz, J. J. Mendoza-Arenas, F. J. Rodríguez, C. Tejedor, and L. Quiroga, Phys. Rev. B **97**, 235134 (2018).

[75] M. Heyl, F. Pollmann, and B. Dóra, Phys. Rev. Lett. **121**, 016801 (2018).

[76] D. Bernard and A. LeClair, "A classification of non-hermitian random matrices," in *Statistical Field Theories*, edited by A. Cappelli and G. Mussardo (Springer Netherlands, Dordrecht, 2002) pp. 207–214.

[77] H. Zhou and J. Y. Lee, arXiv:1812.10490 (2018).

[78] K. Kawabata, K. Shiozaki, M. Ueda, and M. Sato, arXiv:1812.09133 (2018).

[79] U. Magnea, J. Phys. A: Math. Theor. **41**, 045203 (2008).

[80] K. Esaki, M. Sato, K. Hasebe, and M. Kohmoto, Phys. Rev. B **84**, 205128 (2011).

[81] M. S. Rudner and L. S. Levitov, Phys. Rev. Lett. **102**, 065703 (2009).

[82] S. Lieu, Phys. Rev. B **98**, 115135 (2018).

[83] Y. Nakamura, M. Mine, M. Okumura, and Y. Yamanaka, Phys. Rev. A **77**, 043601 (2008).

[84] M. B. Plenio and P. L. Knight, Rev. Mod. Phys. **70**, 101 (1998).

[85] T. Prosen, New J. Phys. **10**, 043026 (2008).

[86] G. Lindblad, Comm. Math. Phys. **48**, 119 (1976).

[87] T. E. Lee and C.-K. Chan, Phys. Rev. X **4**, 041001 (2014).

[88] C. E. Rüter, K. G. Makris, R. El-Ganainy, D. N. Christodoulides, M. Segev, and D. Kip, Nat. Phys. **6**, 192 (2010).

[89] C. M. Bender and S. Boettcher, Phys. Rev. Lett. **80**, 5243 (1998).

[90] C. M. Bender, D. C. Brody, and H. F. Jones, Phys. Rev. Lett. **89**, 270401 (2002).

[91] L. Lu, J. D. Joannopoulos, and M. Soljačić, Nat. Photon. **8**, 821 (2014).

[92] T. Ozawa, H. M. Price, A. Amo, N. Goldman, M. Hafezi, L. Lu, M. Rechtsman, D. Schuster, J. Simon, O. Zilberberg, *et al.*, arXiv:1802.04173 (2018).

[93] S. Raghu and F. D. M. Haldane, Phys. Rev. A **78**, 033834 (2008).

[94] A. Mostafazadeh, J. Math. Phys. **43**, 205 (2002).

[95] R. Barnett, Phys. Rev. A **88**, 063631 (2013).

[96] B. Galilo, D. K. K. Lee, and R. Barnett, Phys. Rev. Lett. **115**, 245302 (2015).

[97] V. Peano, M. Houde, F. Marquardt, and A. A. Clerk, Phys. Rev. X **6**, 041026 (2016).

[98] V. Peano, M. Houde, C. Brendel, F. Marquardt, and A. A. Clerk, Nat. Commun. **7**, 10779 (2016).

[99] A. McDonald, T. Pereg-Barnea, and A. A. Clerk, Phys. Rev. X **8**, 041031 (2018).

[100] R. Shindou, R. Matsumoto, S. Murakami, and J.-i. Ohe, Phys. Rev. B **87**, 174427 (2013).

[101] H. Schomerus, Opt. Lett. **38**, 1912 (2013).

[102] C. Yuce, Phys. Lett. A **379**, 1213 (2015).

[103] B. Zhu, R. Lü, and S. Chen, Phys. Rev. A **89**, 062102 (2014).

[104] C. Poli, M. Bellec, U. Kuhl, F. Mortessagne, and H. Schomerus, Nat. Commun. **6**, 6710 (2015).

[105] J. M. Zeuner, M. C. Rechtsman, Y. Plotnik, Y. Lumer, S. Nolte, M. S. Rudner, M. Segev, and A. Szameit, Phys. Rev. Lett. **115**, 040402 (2015).

[106] A. Weimann, M. Kremer, Y. Plotnik, Y. Lumer, S. Nolte, K. Makris, M. Segev, M. Rechtsman, and A. Szameit, Nat. Mater. **16**, 433 (2017).

[107] L. Xiao, X. Zhan, Z. H. Bian, K. K. Wang, X. Zhang, X. P. Wang, J. Li, K. Mochizuki, D. Kim, N. Kawakami, W. Yi, H. Obuse, B. C. Sanders, and P. Xue, Nat. Phys. **13**, 1117 EP (2017).

[108] H. Shen, B. Zhen, and L. Fu, Phys. Rev. Lett. **120**, 146402 (2018).

[109] Y. C. Hu and T. L. Hughes, Phys. Rev. B **84**, 153101 (2011).

[110] P. K. Ghosh, J. Phys.: Condens. Matter **24**, 145302 (2012).

[111] S.-D. Liang and G.-Y. Huang, Phys. Rev. A **87**, 012118 (2013).

[112] D. Leykam, K. Y. Bliokh, C. Huang, Y. D. Chong, and F. Nori, Phys. Rev. Lett. **118**, 040401 (2017).

[113] M. Klett, H. Cartarius, D. Dast, J. Main, and G. Wunner, Phys. Rev. A **95**, 053626 (2017).

[114] S. Lieu, Phys. Rev. B **97**, 045106 (2018).

[115] S. R. Pocock, X. Xiao, P. A. Huidobro, and V. Giannini, ACS Photon. **5**, 2271 (2018).

[116] S. Yao and Z. Wang, Phys. Rev. Lett. **121**, 086803 (2018).

[117] F. K. Kunst, E. Edvardsson, J. C. Budich, and E. J. Bergholtz, Phys. Rev. Lett. **121**, 026808 (2018).

[118] W. P. Su, J. R. Schrieffer, and A. J. Heeger, Phys. Rev. Lett. **42**, 1698 (1979).

[119] J. K. Asbóth, L. Oroszlány, and A. Pályi, *A short course on topological insulators: Band structure and edge states in one and two dimensions*, Vol. 919 (Springer, 2016).

[120] M. Franz and L. Molenkamp, *Topological Insulators*, Vol. 6 (Elsevier, 2013).

[121] J. Garrison and E. Wright, Phys. Lett. A **128**, 177 (1988).

[122] G. Dattoli, R. Mignani, and A. Torre, J. Phys. A: Math. Gen. **23**, 5795 (1990).

[123] W. D. Heiss, J. Phys. A: Math. Theor. **45**, 444016 (2012).

[124] S. Yao, F. Song, and Z. Wang, Phys. Rev. Lett. **121**, 136802 (2018).

[125] C. Yin, H. Jiang, L. Li, R. Lü, and S. Chen, Phys. Rev. A **97**, 052115 (2018).

[126] C. H. Lee and R. Thomale, Phys. Rev. B **99**, 201103 (2019).

[127] L. Herviou, J. H. Bardarson, and N. Regnault, Phys. Rev. A **99**, 052118 (2019).

[128] Y.-M. Lu and D.-H. Lee, arXiv:1403.5558 (2014).

[129] S. Ryu, A. P. Schnyder, A. Furusaki, and A. W. W. Ludwig, New J. Phys. **12**, 065010 (2010).

[130] D. A. Takahashi and M. Nitta, Ann. Phys. **354**, 101 (2015).

[131] S. Lieu, arXiv:1904.07481 (2019).

[132] Y. Ashida, S. Furukawa, and M. Ueda, Phys. Rev. A **94**, 053615 (2016).

[133] W. Kozlowski, S. F. Caballero-Benitez, and I. B. Mekhov, Phys. Rev. A **94**, 012123 (2016).

[134] N. Katz, M. Ansmann, R. C. Bialczak, E. Lucero, R. McDermott, M. Neeley, M. Steffen, E. M. Weig, A. N. Cleland, J. M. Martinis, and A. N. Korotkov, Science **312**, 1498 (2006).

[135] J. A. Sherman, M. J. Curtis, D. J. Szwer, D. T. C. Allcock, G. Imreh, D. M. Lucas, and A. M. Steane, Phys. Rev. Lett. **111**, 180501 (2013).

[136] P. Coleman, *Introduction to Many-Body Physics* (Cambridge University Press, 2015).

[137] K. Kawabata, Y. Ashida, H. Katsura, and M. Ueda, Phys. Rev. B **98**, 085116 (2018).

[138] M. Klett, H. Cartarius, D. Dast, J. Main, and G. Wunner, Phys. Rev. A **95**, 053626 (2017).

[139] H. Menke and M. M. Hirschmann, Phys. Rev. B **95**, 174506 (2017).

[140] B. A. Bernevig and T. L. Hughes, *Topological insulators and topological superconductors* (Princeton University Press, 2013).

[141] N. Read and D. Green, Phys. Rev. B **61**, 10267 (2000).

[142] N. Henkel, R. Nath, and T. Pohl, Phys. Rev. Lett. **104**, 195302 (2010).

[143] T. Macrì, F. Maucher, F. Cinti, and T. Pohl, Phys. Rev. A **87**, 061602(R) (2013).

[144] R. Bianco and R. Resta, Phys. Rev. B **84**, 241106 (2011).

[145] M. D. Caio, G. Möller, N. R. Cooper, and M. J. Bhaseen, Nat. Phys. **15**, 257 (2019).

[146] D. Malz, J. Knolle, and A. Nunnenkamp, arXiv:1901.02282 (2019).

Appendix A

Analytical Bogoliubov spectrum for S^5 condensates

In Sec. 2.5, we discussed how to numerically calculate the Bogoliubov spectrum of the S^5 degenerate condensate. Here, we demonstrate how to obtain analytical solutions for the spectrum via a perturbative expansion in the small k limit. This will help explain why broken symmetry generators correspond to gapless excitations. To find the Bogoliubov spectrum, our ultimate task is to find the eigenvalues and right-eigenvectors of $\Sigma_z H_k$. (See Eq. (2.12).) We thus define this quantity as: $H_k^\sigma = \Sigma_z H_k$ and expand it in a perturbation series in small k

$$H_k^\sigma = H_0^\sigma + kH_1^\sigma + k^2 H_2^\sigma, \tag{A.1}$$

where we drop the superscript σ in the forthcoming analysis. We do the same for the eigenvalues E and eigenvectors ξ

$$E_k = E_0 + kE_1 + k^2 E_2, \qquad \xi_k = \xi_0 + k\xi_1 + k^2\xi_2. \tag{A.2}$$

Matching each expression in orders of k leads to

$$H_0\xi_0 = E_0\xi_0, \tag{A.3}$$

$$H_0\xi_1 + H_1\xi_0 = E_0\xi_1 + E_1\xi_0, \tag{A.4}$$

$$H_0\xi_2 + H_1\xi_1 + H_2\xi_0 = E_0\xi_2 + E_1\xi_1 + E_2\xi_0. \tag{A.5}$$

Since we only care about the gapless modes of the system, we look for zero-modes of H_0, namely eigenvectors which satisfy: $H_0\xi_0 = 0$. As mentioned in Sec. 2.3.2, orthogonal zero-modes of the Bogoliubov Hamiltonian are found by acting the symmetry generators on the order-parameter according to: $\mathbf{e}_{0,i} = (\Delta_i \mathbf{c}, -\Delta_i^* \mathbf{c}^*)^T$.

Here we briefly summarize the steps to perform perturbation theory in the Bogoliubov framework, which are explained in detail in Ref. [45]. Generically, any Bogoliubov Hamiltonian at $k = 0$ may be written in the following form:

$$X^{-1}H_0X = \begin{pmatrix} 0 & 0 & 0 & 0 & 0 & 0 & 0 \\ 0 & \ddots & 0 & 0 & 0 & 0 & 0 \\ 0 & 0 & A & A & 0 & 0 & 0 \\ 0 & 0 & -A & -A & 0 & 0 & 0 \\ 0 & 0 & 0 & 0 & \ddots & 0 & 0 \\ 0 & 0 & 0 & 0 & 0 & \lambda & 0 \\ 0 & 0 & 0 & 0 & 0 & 0 & \ddots \end{pmatrix}, \tag{A.6}$$

where $X = \left[\mathbf{x}_i, \mathbf{x}_j, \ldots \frac{\mathbf{y}_k+\mathbf{z}_k}{2}, \frac{-\mathbf{y}_k+\mathbf{z}_k}{2}, \ldots, \mathbf{w}_l, \mathbf{w}_m, \ldots\right]$, $H_0\mathbf{x} = 0$, $H_0\mathbf{y} = 0$, $H_0\mathbf{z} = \kappa\mathbf{y}$, $H_0\mathbf{w} = \lambda\mathbf{w}$. That is, the vectors $\mathbf{x}, \mathbf{y}$ are linear combinations of the zero-modes $\mathbf{e}_0$, and the $\mathbf{w}$ eigenvectors have non-zero eigenvalues. These together "diagonalize" H_0. Note that since H_0 is not Hermitian (due to the multiplication of Σ_z on the left) it cannot in general be fully diagonalized and hence we need the "Jodan-associated vector" $\mathbf{z}$ which satisfies the condition $H_0\mathbf{z} = \kappa\mathbf{y}$ in order to bring the subspace spanned by combinations of $\mathbf{x}, \mathbf{y}$ into block diagonal form. (We will perform perturbation theory around a non-diagonalizable matrix H_0, called singular perturbation theory around an exceptional point.)

It is useful to find the vectors $\mathbf{x}, \mathbf{y}, \mathbf{z}$ since they satisfy σ-orthogonality conditions which constrain our perturbation theory. Define the inner-product: $(\mathbf{a}, \mathbf{b})_\sigma = \mathbf{a}^\dagger\Sigma_z\mathbf{b}$. The vectors satisfy the following properties: $(\mathbf{y}_i, \mathbf{y}_j)_\sigma = 0$, $(\mathbf{y}_i, \mathbf{w}_j)_\sigma = 0$, $(\mathbf{y}_i, \mathbf{z}_j)_\sigma = 2\delta_{ij}$, $(\mathbf{y}_i, \mathbf{x}_j)_\sigma = 0$, $(\mathbf{x}_i, \mathbf{x}_j)_\sigma = 2\delta_{ij}$. As we will soon see, the vectors $\mathbf{y}$ serve as the "seeds" of linear gapless modes, while the vectors $\mathbf{x}$ serve as the seeds of quadratic gapless modes. This is in agreement with standard Bogoliubov theory, where the

linear mode has zero-norm (with respect to the newly defined inner-product) at $k = 0$.

A.1 Linear modes

The most general linear gapless mode is $\xi_0^{\text{lin}} = \sum_i c_i \mathbf{y}_i$. For higher orders $\xi_{j\neq 0}$, we find

$$\xi_{j\neq 0} = d_{z_m}^{(j)} \mathbf{z}_m + d_{w_n}^{(j)} \mathbf{w}_n, \tag{A.7}$$

where repeated indices are summed. Note that this eigenvector has no $\mathbf{y}$ component because we can always redefine ξ_0 such that it absorbs any $\mathbf{y}$ from the higher-order eigenvectors while still satisfying $H_0\xi_0 = 0$. Now consider the quantity

$$H_0\xi_{j\neq 0} = \kappa_m d_{z_m}^{(j)} \mathbf{y}_m + \lambda_n d_{w_n}^{(j)} \mathbf{w}_n, \tag{A.8}$$

where we have used the fact: $H_0\mathbf{z} = \kappa\mathbf{y}$. Substituting this expression into (A.4) leads to

$$\kappa_m d_{z_m}^{(1)} \mathbf{y}_m + \lambda_n d_{w_n}^{(1)} \mathbf{w}_n = c_i \left(E_1 - H_1\right) \mathbf{y}_i, \tag{A.9}$$

from this equation we may solve for the coefficients $d^{(1)}$. This tells us the lowest-order correction to the eigenvector ξ_1 in terms of the quantities c_i, E_1, and importantly, ensures that the finite k eigenvector has non-zero norm. In order to solve for the remaining quantities, we turn to the second-order equation. Consider taking the inner-product of (A.5) with respect to $\mathbf{y}_i$ on both LHS and RHS:

$$\left(\mathbf{y}_i, H_1\xi_1 + H_2\xi_0\right)_\sigma = E_1 \left(\mathbf{y}_i, \xi_1\right)_\sigma \tag{A.10}$$

$$\implies E_1 = \frac{\left(\mathbf{y}_i, H_1\xi_1 + H_2\xi_0\right)_\sigma}{\left(\mathbf{y}_i, \xi_1\right)_\sigma} \tag{A.11}$$

There are as many equations as there are numbers of vectors $\mathbf{y}_i$ (which we call n) and hence one may write an $n \times n$ matrix in terms of the coefficients c_i. In order to solve for E_1, c_i we simply set the determinant of the matrix to zero and solve for the eigenvalues E_1 and corresponding eigenvectors c_i. These provide us with explicit expressions for all linear gapless modes of the system.

A.2 Quadratic modes

Similarly the quadratic modes are determined by setting: $\xi_0^{\text{quad}} = \sum_i c_i \mathbf{x}_i, \xi_{j\neq 0} = d_{z_m}^{(j)} \mathbf{z}_m + d_{w_n}^{(j)} \mathbf{w}_n$. Substituting these expressions into the first-order equation (where now $E_1 = 0$ since there is no linear contribution to the low-energy dispersion) results in

$$\kappa_m d_{z_m}^{(1)} \mathbf{y}_m + \lambda_n d_{w_n}^{(1)} \mathbf{w}_n = -c_i H_1 \mathbf{x}_i, \tag{A.12}$$

which allows to solve for d parameters in terms of cs. Again, in order to solve for the remaining variables (including E_2) we must turn to the second-order equation and take the inner products with respect to the $\mathbf{x}_i$, resulting in n equations for n unknowns (where there are n distinct $\mathbf{x}_i$ vectors)

$$E_2 = \frac{(\mathbf{x}_i, H_1\xi_1 + H_2\xi_0)_\sigma}{(\mathbf{x}_i, \xi_1)_\sigma}. \tag{A.13}$$

Setting the determinant to zero allows us to solve for the remaining eigenvalues E_2 and eigenvectors c_i.

A.3 Expressions for gapless modes

We will apply the formalism described above to find an explicit expressions for the Bogoliubov dispersion, we use the analytical expression for H_k described in the previous section. Although the form of the Hamiltonian is quite simple, the expressions for the single-particle eigenstates in terms of a large number of Fouerier coefficients can only be done numerically. As a first approximation, we may approximate the single-particle eigenstates as only involving the "first layer" of Fourier coefficients, i.e. the 7 spots closest to the origin, oriented in a hexagon around the $k = 0$ site (the black dots in Fig. 2.5). This approximation is valid in the limit of small potential, i.e. a nearly-free particle. In this approximation, we only consider 7 Fourier modes, and therefore we must specify only 7 condensation amplitudes: $\alpha = (0, \alpha_1, \alpha_2, \alpha_3, -\alpha_1, -\alpha_2, -\alpha_3)$ where the indices $i \in 0:6$ correspond to the vectors $\mathbf{G}_0 = [0,0], \mathbf{G}_i = Q/2\left[\cos\left(\frac{i\pi}{6}\right), \sin\left(\frac{i\pi}{6}\right)\right]$ with the condition

$|\alpha_1|^2 + |\alpha_2|^2 + |\alpha_3|^2 = 1$.

Carrying out the perturbation series, we find the following expressions for the case of an evenly spaced condensate $\alpha_1 = \alpha_2 = \alpha_3 = 1/\sqrt{6}$

$$E_{\text{lin.}}(k) = \sqrt{\frac{2\epsilon_k V_0 \left(2\epsilon_{Q/2} + |U|\right)}{|U|}}, \tag{A.14}$$

$$E_{\text{quad.1}}(k) = \epsilon_k \left(\frac{(2\epsilon_{Q/2} + |U|) - \epsilon_{Q/2}}{|U|}\right), \tag{A.15}$$

$$E_{\text{quad.2}}(k) = \epsilon_k \left(\frac{(2\epsilon_{Q/2} + |U|) + \epsilon_{Q/2}}{|U|}\right), \tag{A.16}$$

which agrees exactly at small k for a single-layer problem (i.e. small applied field U) and agrees approximately well once a larger number of condensation spots is considered. Interestingly, only the linear mode has a dispersion which depends on the interaction parameter strength V_0, and moreover the dispersion does not depend on direction in the Brillouin zone (i.e. it depends on the magnitude of $\mathbf{k}$ but not its direction).

We may solve for the linear and quadratic modes for the ground-state which picks out a specific M spot condensate, i.e. $\alpha_1 = 1/\sqrt{2}, \alpha_2 = \alpha_3 = 0$

$$E_{\text{lin.}}(k) = \sqrt{\frac{2\epsilon_k V_0 \left(4\epsilon_{Q/2}\cos^2(\theta) + |U|\right)}{|U|}}, \tag{A.17}$$

where θ is the direction in the Brillouin zone taken with respect to the x-axis. We are not able to find analytical expressions for the quadratic modes for general direction θ, however we can do so for the specific direction, e.g. along the x, y axis.

$$E^x_{\text{quad.1}}(k) = \epsilon_k \left(\frac{\epsilon_{Q/2} + |U|}{|U|}\right), \tag{A.18}$$

$$E^x_{\text{quad.2}}(k) = \epsilon_k \left(\frac{\epsilon_{Q/2} + |U|}{|U|}\right), \tag{A.19}$$

$$E^y_{\text{quad.1}}(k) = \epsilon_k \left(\frac{3\epsilon_{Q/2} + |U|}{|U|}\right), \tag{A.20}$$

$$E^y_{\text{quad.2}}(k) = \epsilon_k \left(\frac{3\epsilon_{Q/2} + |U|}{|U|}\right). \tag{A.21}$$

Away from these high-symmetry directions the two quadratic modes are non-degenerate in general.